

Complex flows of complex fluids - Linear instability of dilute polymer solutions and stochastic dynamics of run-and-tumble particles and bacterial suspensions



J N C A S R

Piyush Garg

Engineering Mechanics Unit

Jawaharlal Nehru Centre for Advanced Scientific Research, Bangalore

This dissertation is submitted for the degree of
Doctor of Philosophy

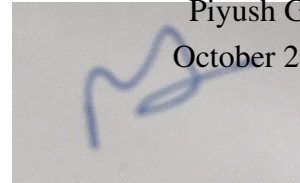
October 2023

Declaration

I hereby declare that the matter embodied in the thesis titled “**Complex flows of complex fluids - Linear instability of dilute polymer solutions and stochastic dynamics of run-and-tumble particles and bacterial suspensions**”, is the result of research work carried out by me at the Engineering Mechanics Unit, Jawaharlal Nehru Centre for Advanced Scientific Research, Bengaluru, India, under the supervision of Prof. Ganesh Subramanian, and that it has not been submitted elsewhere for the award of any degree or diploma.

In accordance with the general practice in reporting scientific observations, due acknowledgement has been rendered appropriately, wherever the work described is based on the findings of other investigators.

Piyush Garg
October 2023



Certificate

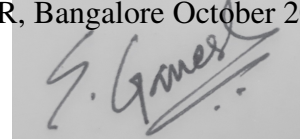
I hereby certify that the matter embodied in this thesis entitled “**Complex flows of complex fluids - Linear instability of dilute polymer solutions and stochastic dynamics of run-and-tumble particles and bacterial suspensions**”, has been carried out by Mr. Piyush Garg at the Engineering Mechanics Unit, Jawaharlal Nehru Centre for Advanced Scientific Research, Bengaluru, India, under my supervision, and that it has not been submitted elsewhere for the award of any degree or diploma.

Dr. Ganesh Subramanian

Professor

Engineering Mechanics Unit

JNCASR, Bangalore October 2023

A rectangular box containing a handwritten signature in black ink, which appears to be "G. Ganesh".

Acknowledgements

First, I would like to thank my research supervisor Prof. Ganesh Subramanian, for guiding me through the PhD process and most importantly giving me the freedom to work on a range of problems - sometimes even widely varying in their detailed focus. The course on fluid mechanics offered by him along with the discussions over the years have been very instrumental and critical in developing my approach and thinking. A part of my thesis work was done in collaboration with Prof. V Shankar from IIT Kanpur, which was immensely helpful.

Apart from my research, I would like to thank Prof. K. R. Sreenivas, Prof. Meheboob Alam and Prof. Santosh Ansumali for the courses they offered during my stay in EMU. From JNC, I would specifically like to thank my (former) labmates Sankalp and Laxman, with whom I have worked on a few problems over the years, under the guidance of Prof. Subramanian, and have had numerical fruitful discussions. Other lab members Navaneeth, Ponnulakshmi, Prateek and Arun have over the years provided a much needed ear as well as any help that I needed. Outside JNC, before ever joining for my PhD, Jason, Dipin and Danny had given me lots to think about during my intermittent visitations.

Finally, I want to acknowledge the support and patience of my parents, and especially my sister.

Abstract

This thesis is concerned with the theoretical study of the dynamics of two classes of complex fluids - dilute polymer solutions (chapter 1) and active suspensions (chapter 2 and 3). In chapter 1, we study the linear stability of pressure-driven pipe and channel flow of dilute polymer solutions. We demonstrate a novel linear instability that describes a hitherto unknown route to turbulence in dilute polymer solutions and explains recent experimental observations of the same. In chapters 2 and 3, we discuss the dynamics of an important class of active fluids viz. suspensions of run-and-tumble particles. In chapter 2, we obtain a closed form solution for the time dependent probability density of run-and-tumble particles in orientation-position space. We use this solution to study the radial and angular variation of the probability density, with time, for an infinitely localized population at the initial instant. In chapter 3, we formulate a fluctuating kinetic theory for bacterial suspensions, where the bacteria are modeled as run-and-tumble particles, with long-range hydrodynamic interactions now being included. We use this theoretical framework to study the variation of the fluid velocity variance and the tracer diffusivity as the threshold for collective motion of the suspension is approached.

Linear instability of Pipe and Channel flow of Dilute Polymer Solutions

Turbulent flow of dilute polymer solutions is of fundamental importance since it exhibits novel dynamics such as turbulent drag reduction [Toms, 1977]. Transition to turbulence in polymer solutions has thus been extensively investigated in recent years [Graham, 2014]. In Newtonian fluids, the transition is initiated by the lift-up effect leading to a non-linear, self sustaining process underlying the ensuing turbulent state, and with associated exact non-linear solutions, that arise beyond a finite Reynolds number (Re), and that make up the turbulent attractor [Kerswell, 2005]. Recent studies of dilute polymer solutions focus on the modification of the Newtonian transition scenario due to the elasticity of the polymer solution, parameterized by the Deborah number (De) [Graham, 2014]. The prevailing viewpoint, and

methods of analysis, in the literature have all been driven by the overriding belief that the canonical viscoelastic shearing flows (pipe and plane Couette) are linearly stable similar to their Newtonian counterparts [Graham, 2014; Morozov and van Saarloos, 2007; Samanta et al., 2013].

In contrast, both early (for example in [Little and Wiegard, 1970]) and recent experiments (for example in [Samanta et al., 2013]) indicate a continuous transition to turbulence for pipe flow of sufficiently concentrated dilute polymer solutions, and thus a linear instability of the laminar state. Similar experimental observations have been made for pressure-driven channel flow [Srinivas and Kumaran, 2017]. Motivated by these experiments, we carry out a linear stability analysis for the canonical viscoelastic shearing flows: pressure-driven pipe and channel flow, and plane Couette flow. We use the Oldroyd-B constitutive equation to model the polymeric stress, where the polymer molecules are modeled as non-interacting Hookean dumbbells. This leads to three governing parameters - (1) the Reynolds number (Re), (2) the Deborah number (De) which represents a ratio of the relaxation time of the polymer molecule to the flow imposed time scale and (3) the viscosity ratio (β) which represents the ratio of the solvent and total viscosity. The Oldroyd-B model predicts a shear-rate independent viscosity and first normal stress coefficient in viscometric flows. It has been shown to reproduce observations of linear instabilities in polymer solutions in the literature, and is therefore a natural choice for the stability analysis. The eigenvalue problem is solved numerically using a spectral collocation method. The eigenvalue, $c(Re, De, k, \beta)$, is dependent on four parameters, where k is the non-dimensional axial wavenumber of the perturbation.

The eigenspectrum for pipe flow shows a single unstable mode, multiple damped discrete modes and a pair of continuous spectra consisting of singular modes whose decay rates are set by the polymer stress relaxation in the dilute limit. The unstable mode propagates at a speed close to the base-state maximum, and is therefore termed a center-mode. The polymer force field is localized near the centerline and reinforces the velocity field, leading to the instability. For a given β and k , the instability is shown to exist in the asymptotic limit $Re \rightarrow \infty$ and $De \rightarrow \infty$ with $De/Re^{1/2} \rightarrow const$ confined to a finite interval. The unstable eigenfunction becomes localized near the centerline in this asymptotic limit. Viscous diffusion balances inertia in the near-centerline boundary layer, and the perturbation polymeric stress stays comparable since $De \sim \mathcal{O}(Re^{1/2})$. The instability thus requires a balance of inertia, viscous and elastic polymer stresses close to the centerline. The instability qualitatively explains the experimental observations of a linear pathway to turbulence in pipe flow of dilute polymer solutions [Choueiri et al., 2021; Garg et al., 2018; Little and Wiegard, 1970; Samanta et al., 2013].

The instability of viscoelastic pipe flow discussed above is in striking contrast to Newtonian pipe flow which remains linearly stable at all Reynolds numbers. A similar center-mode instability is shown to exist for pressure-driven channel flow of an Oldroyd-B fluid. Analogous results for the neutral curves and the boundary layer scalings, for the unstable eigenfunctions, are obtained. Plane Couette flow is found to be stable at all Re and De values examined. The stabilizing effect of stress diffusion is also examined. For realistic values of the stress diffusivity, the instability remains virtually unaltered. Finally, we have extended the analysis to include weakly non-linear effects on the unstable eigenmode for pressure-driven channel flow, which is used to determine the nature of the bifurcation at onset.

Exact solution for the probability density of run-and-tumble particles

Swimmer suspensions naturally constitute an important class of active systems since they violate time reversal symmetry at the scale of a single swimmer [Bechinger et al., 2016]. Based on the stochastic dynamics of the orientation vector (\mathbf{p}) of the swimmer, such active particles have been further classified into Active Brownian Particles (ABPs) and Run-and-Tumble Particles (RTPs) [Bechinger et al., 2016]. For ABPs, the orientation vector is subject to Gaussian noise, and thus evolves through infinitesimal changes on the unit sphere. In contrast, RTPs, the focus of this thesis, swim along straight trajectories (the run phase) before executing an impulsive stochastic reorientation (the tumble phase) by a large amount [Berg, 1993]. The reorientation events are generally assumed to follow Poissonian statistics with a mean tumble time τ . In the biological context, several species of bacteria exhibit run-and-tumble motion [Berg, 1993]. Some artificially constructed colloidal microswimmers have also been seen to behave as RTPs [Karani et al., 2019]. A closed form statistical description for the temporal evolution of RTP populations is not available in the existing literature.

We derive the exact solution for the joint orientation-position space probability density of RTPs ($\Omega(\mathbf{r}, \mathbf{p}, t)$), which is governed by a conservation equation that includes convection due to swimming (running along \mathbf{p}), and relaxation to isotropy due to tumbling. We perform an exact inversion of the ‘run-and-tumble operator’ in Fourier space, that governs the Fourier transformed probability density ($\tilde{\Omega}(\mathbf{k}, \mathbf{p}, t)$), in both two and three dimensions. Exact analytical expressions for the eigenfunctions (and their adjoints) of the run-and-tumble operator in Fourier space are obtained by solving integral equations. Having established both the orthogonality and completeness of the eigenfunctions, and their adjoints, these are then used to construct the Green’s function, which can be interpreted as the time dependent probability

density evolving from an infinitely localized initial condition in position-orientation space. In the analysis above, and the results stated below, the time scale is non-dimensionalized by the mean tumble time (τ) and the length scale by $U_s \tau$, where U_s is the swim speed, so that the mean tumble time and swim speed become unity in the non-dimensional units.

The eigenspectrum of the run-and-tumble operator comprises a set of continuous spectrum modes and a regular discrete mode in 3D (a regular and two singular discrete modes in 2D). The continuous spectrum modes exist for both axisymmetric and non-axisymmetric orientation modes in 3D (odd and even modes in 2D), while the discrete modes only exist for axisymmetric orientation modes in 3D (even modes in 2D). The decay of the continuous spectrum modes is solely governed by the mean tumble time and these modes therefore relax at the same rate independent of the wavenumber. These denote the fastest decaying modes in the spectrum. The finite decay rate, even in the limit of zero wavenumber, implies that the continuous spectrum modes do not contribute to the long-time behavior. The regular discrete mode shows wavenumber dependent relaxation, reducing to a diffusive mode in the long wavelength limit with an effective, non-dimensional, diffusivity given by $1/3$ in 3D ($1/2$ in 2D). The discrete eigenmode exists only for a finite range of wavenumbers, falling into the continuous spectrum at $k = 1/4$ ($k = 1/2\pi$) in 3D (2D).

We examine the time evolution of the intermediate scattering function (ISF) ($\tilde{\Omega}(k, t)$) for RTPs. For $k < 1/4$ ($k < 1/2\pi$) in 3D (2D), the ISF shows purely diffusive decay, typical of passive systems. For larger wavenumbers, the ISF shows an oscillatory decay. We next examine the probability density ($\Omega(r, t)$) of finding a swimmer at the radial distance r at time t , with any orientation, starting from an infinitely localized population at $r = 0$ at the initial time ($t = 0$).¹ In both 2D and 3D, we expect to find a contribution of the form $\delta(r - t)e^{-t}$, corresponding to the exponentially decaying fraction of swimmers that have not tumbled until time t . We examine $\Omega^{ND}(r, t) = \Omega(r, t) - \delta(r - t)e^{-t}$ to focus on the spatial structure behind the front. The Fourier inversion is carried out numerically by adding a translational diffusivity (D_T), which regularizes $\Omega(r, t)$; the results are obtained by extrapolating the numerical results to the limit of small D_T . For the 2D case, we find that the swimmers initially aggregate at the front and the spatial structure is dominated by the continuous spectrum contribution. At long times, the diffusive discrete mode dominates and the probability density has a maximum at $r = 0$. For all time t , Ω^{ND} diverges as $(t - r)^{-1/2}$ on approaching the front. We also examine $\Omega(r, t)$ in 3D, and its structure and variation with time is observed to be similar to 2D, although there is no divergence on approach towards the front from within (apart from the delta function that represents the front itself).

¹For the passive system, the simplest and classical example of which is an ensemble of diffusing spherical Brownian particles, the probability density $\Omega(r, t)$ for the chosen initial condition is a Gaussian distribution which exhibits a diffusive spread with time.

Next, we obtain the evolution of the joint probability density ($\Omega(\mathbf{r}, \mathbf{p}, t)$) in orientation-position space in both two and three dimensions, assuming an infinitely localized population at $r = 0$ with an isotropic orientation distribution at $t = 0$. In 2D, using a \mathbf{p} -aligned co-ordinate system, the joint probability density is parameterised by the radial vector $(r \cos(\chi), r \sin(\chi))$. We study the dynamics of the joint probability density ($\Omega(r, \chi, t)$) for varying r and χ , with $\Omega(r, \chi, t = 0) = \delta(r)$. For swimmers aligned with the radial direction ($\chi = 0$), at early times, we see an active regime - a power law scaling $\Omega^{ND}(r, \chi = 0, t) \propto \frac{1}{t-r}$ for all r . For longer times, we see a transition to a passive regime - the swimmers accumulate near the origin ($r = 0$) leading to a local Gaussian profile that exhibits a diffusive spread, but there is again the algebraic divergence, given by $\Omega(r, \chi = 0, t) \propto \frac{1}{t-r}$, in the neighborhood of the front. We see similar phenomenology for other values of χ - there is an active-to-passive regime transition with time for any value of χ , although the exact radial variation of $\Omega(r, \chi, t)$ in the two regimes varies with χ . We also obtain the angular variation of $\Omega(r, \chi, t)$ with χ at a given radial location and time. Similar results for the radial and angular variation are obtained in 3D.

Fluctuating kinetic theory for bacterial suspensions

Active matter systems involve energy injection at the microscale, and consequently break microscopic time reversal symmetry. This leads to non-trivial dynamics which are forbidden by symmetry in equilibrium (or near-equilibrium) systems [Cates, 2012]. Bacterial suspensions have been extensively studied, both experimentally [Gachelin et al., 2014] and theoretically [Marchetti et al., 2013], over recent years as a prototypical example of such active matter systems. Long-ranged hydrodynamic interactions lead to ‘collective motion’ in bacterial suspensions on length scales much larger than a single bacterium [Koch and Subramanian, 2011]. The collective dynamics in turn affects the material properties of the suspension, leading to enhanced velocity fluctuations and tracer diffusivities [Wu and Libchaber, 2000]. Understanding the dynamics of bacterial suspensions near ‘criticality’ would therefore lead to a greater insight into the non-equilibrium dynamics of active matter systems. Motivated by these considerations, we develop a fluctuating kinetic theory, which is used to study the correlations that develop in a bacterial suspension near the onset of collective motion. Our mathematical formalism allows us to obtain analytical results.

As mentioned earlier, an individual bacterium behaves as a run-and-tumble particle with swim speed U_s and mean tumble time, τ . To model a bacterial suspension, we therefore consider a suspension of RTPs, with volume fraction nL^3 where n is the number of particles per unit volume and L the length of a particle. The swimming motion induces a long-ranged

fluid flow, which in turn convects and rotates the other particles - these constitute the long-ranged hydrodynamic interactions. The fluid flow in the suspension is governed by the Stokes equations with an additional stress (Σ^a) due to the swimming motion. The sign of the active stress depends on whether the swimmers are pushers (like bacteria) or pullers (like algae). A suspension of pushers alone shows a transition to collective motion at a finite threshold (given by the non-dimensional number $((nL^2U_s\tau)_{cr})$) [Koch and Subramanian, 2011]. We analyze correlations for both pusher and puller suspensions.

Since swimming implies broken time reversal symmetry at the microscale, we cannot appeal to a fluctuation-dissipation theorem to derive the associated noise correlations. Instead, we derive the noise correlations starting from the master equation governing the fluctuating phase-space density ($\Omega(\mathbf{x}, \mathbf{p}, t)$). For correlations in the homogeneous isotropic state the noise is shown to become additive and its second moment suffices; a closed integro-differential equation can then be obtained for the fluctuating density in Fourier space ($\tilde{\Omega}(\mathbf{k}, \mathbf{p}, t)$). Analytical expressions for both the direct and adjoint eigenfunctions of this equation are obtained, which are then used to obtain the Green's function and the evolution of $\tilde{\Omega}$. The Fourier inversion is carried out numerically.

The fluctuating phase-space density is then used to derive the correlations for the fluid velocity field. The fluid velocity variance, defined by $\langle \mathbf{u} \cdot \mathbf{u} \rangle$, remains finite in a suspension of pullers, but diverges as $\frac{1}{((nL^2U_s\tau)_{cr}) - (nL^2U_s\tau)^{1/2}}$ for a suspension of pushers, near the threshold $(nL^2U_s\tau)_{cr}$ for collective motion. The fluid velocity covariance, $\langle \mathbf{u}(\mathbf{r}) \cdot \mathbf{u}(0) \rangle$, decays increasingly gradually, reflecting the development of long-ranged correlations as the threshold is approached. This behavior of the variance and covariance is explained by noting that the decorrelation is dominated by length scales of $O(nL^2)^{-1}$, that characterize the slowest decaying long-wavelength velocity fluctuations; these long-wavelength modes denote the coordinated effect of the disturbance fields of large number of swimmers. In contrast, away from the threshold decorrelation occurs on the length scale L of a single bacterium. Next, we obtain the diffusivity (\mathcal{D}) of a passive tracer convected by the bacterial suspension using the Green-Kubo formula. The tracer diffusivity stays finite for pullers, and diverges for pushers in the vicinity of the collective motion threshold. However, the divergence of the diffusivity is stronger than that for the velocity variance, being proportional to $\frac{1}{((nL^2U_s\tau)_{cr}) - (nL^2U_s\tau)^{3/2}}$. We also examine the polar and nematic orientation correlations near the threshold.

We have also examined the correlations in a bacterial suspension away from the threshold. Direct pair interactions due to the individual long-ranged disturbance flow fields also lead to a non-trivial variation of the velocity variance and tracer diffusivity with the volume fraction (nL^3) and swimmer run length $(U_s\tau/L)$. The variation of the velocity variance

has been examined earlier and it was found at $O(nL^3)^2$, that the velocity variance diverges logarithmically with the swimmer run length [Nambiar et al., 2021]. We extend the analysis at $O(nL^3)^2$ to the tracer diffusivity. At $O(nL^3)^2$, the tracer mean squared displacement is shown to undergo an increasingly broad crossover from the ballistic to the diffusive regime for persistent RTPs ($U_s\tau/L \gg 1$), with the tracer diffusivity exhibiting a stronger linear increase with the swimmer run length.

Table of contents

List of figures	xiv
List of tables	xviii
1 Linear instability of Pipe and Channel flow of Dilute Polymer Solutions	1
1.1 Introduction	1
1.2 Governing Equations	3
1.2.1 Laminar Flow	4
1.2.2 Formulation of the linear stability problem	4
1.3 Linear Instability	5
1.3.1 Pipe flow	5
1.3.2 Plane Poiseuille flow	8
1.3.3 Plane Couette flow	11
1.3.4 Inclusion of stress diffusivity for pipe flow	11
1.4 Weakly non-linear analysis	13
1.5 Discussion on the importance of the center-mode instability	17
2 Exact solution for the probability density of run-and-tumble particles	20
2.1 Introduction	20
2.2 The run-and-tumble operator	22
2.2.1 Governing Equation	22
2.2.2 Eigenspectrum of the Run and Tumble Operator \mathcal{L}	24
2.2.3 Adjoint Eigenfunctions of \mathcal{L}	29
2.2.4 Greens Function of \mathcal{L}	31
2.3 Results	35
2.3.1 Intermediate Scattering Function	35
2.3.2 Position-space Probability density	37
2.3.3 Orientation-position-space Probability density	40

2.4	Conclusion	47
2.5	Derivation of the adjoint eigenfunctions	48
2.5.1	Finding the adjoint eigenfunctions: 2D	48
2.5.2	Finding the adjoint eigenfunctions: 3D	50
2.5.3	Normalization of the direct and adjoint eigenfunctions	52
2.5.4	Orthogonality of the eigenfunctions	53
3	Fluctuating kinetic theory for bacterial suspensions	55
3.1	Introduction	55
3.2	Correlations (Tracer diffusivity) away from the collective motion threshold	57
3.2.1	Suspensions of non-interacting swimmers	59
3.2.2	Suspensions of interacting swimmers	61
3.3	Correlations near the collective motion threshold	65
3.3.1	Stochastic run-and-tumble Operator for interacting bacteria	66
3.3.2	Noise Correlations for the Run-And-Tumble Operator	67
3.3.3	Solving the interacting Run-And-Tumble Operator	68
3.3.4	Phase Space Density Correlation Function	72
3.3.5	Results	76
3.4	Conclusion	83
	References	85

List of figures

1.1	Numerically obtained eigenspectrum for pipe flow of an Oldroyd-B fluid for $Re = 800, De = 65, \beta = 0.65$ and $k = 1$ (for $N = 200$ and 400); the inset zooms into the region around the unstable mode.	6
1.2	Perturbation velocity (left) and polymer force (right) fields for the unstable mode for $Re = 800, De = 65, \beta = 0.6$ and $k = 1$	6
1.3	The numerically obtained neutral curves for pipe flow for varying β with $k = 1$	7
1.4	Tracking the unstable mode with varying De and β with Re, k and $De(1 - \beta)$ fixed for pipe flow.	7
1.5	The unstable center-mode eigenfunctions for the axial velocity (left) and radial velocity (right) in scaled boundary-layer coordinates in the limit $Re \rightarrow \infty$ and $De \rightarrow \infty$ for a fixed $De/Re^{1/2}$ ($k = 1$ and $\beta = 0.5$).	8
1.6	Numerically obtained eigenspectrum for plane Poiseuille flow of an Oldroyd-B fluid for $Re = 300, De = 250, k = 1$ and $\beta = 0.95$	9
1.7	The numerically obtained neutral curves for plane Poiseuille flow for varying β with $k = 1$	9
1.8	Tracking the unstable mode with varying De and β with Re, k and $De(1 - \beta)$ fixed for plane Poiseuille flow.	10
1.9	The unstable center-mode eigenfunctions for the tangential velocity (top) and normal velocity (bottom) in scaled boundary-layer coordinates in the limit $Re \rightarrow \infty$ and $De \rightarrow \infty$ for a fixed $De/Re^{1/2}$ ($k = 1$ and $\beta = 0.8$) for plane Poiseuille flow.	10
1.10	Numerically obtained eigenspectrum for plane Couette flow of an Oldroyd-B fluid for $Re = 2500, De = 100, k = 1$ and $\beta = 0.8$	11
1.11	The effect of stress diffusion ($D\lambda/R^2$) on the onset Re for pipe flow for different E, β and k values.	12
1.12	The mean axial velocity profile (v_x) at the onset for $Re = 50, De = 90, \beta = 0.95$ and $k = 1$	14

1.13	The profile for the stream-wise component of the mean normal stress a_{xx} at the onset for $Re = 50$, $De = 90$, $\beta = 0.95$ and $k = 1$	14
1.14	Variation of the Landau coefficient (a_3) along the two branches of the neutral curves in the $Re - De$ plane for $k = 1$ and $\beta = 0.8$	16
1.15	Variation of the Landau coefficient (a_3) with De with the other parameters fixed at $Re = 300$, $\beta = 0.8$, $k = 1$	17
1.16	Schematic showing the various possible dynamics in the $Re-De$ plane when accounting for the novel transition pathway examined in this chapter.	19
2.1	Schematic showing the eigenvalue spectrum of the run-and-tumble operator, \mathcal{L} . As discussed in the text, the regular discrete mode only exists for a finite range of k and the singular discrete modes only exist in 2D.	28
2.2	The time evolution of the intermediate scattering function for various wavenumbers (k) in (a) 2D and (b) 3D; the chosen k values are indicated on the RHS of each figure. In (a) the corresponding results from Martens et al. [2012] are plotted as dashed lines, and are in perfect agreement.	36
2.3	(a) The variation of the regularized probability density, $\Omega^{ND}(r)$, with the scaled radial distance, r/t in 2D for $D_T = 10^{-5}$ at various time t . The expression for $\Omega^{ND}(r)$ from Martens et al. [2012] is plotted as dashed lines and we see an exact match; note that Martens et al. [2012] have $D_T = 0$. (b) The effect of the translational diffusivity (D_T) on the regularized probability density, $\Omega^{ND}(r)$ in 2D at $t = 1$. The inset highlights the effect of D_T at the front. (c) The variation of the regularized probability density, $\Omega^{ND}(r)$, with the scaled radial distance, $1 - r/t$ in 2D for $D_T = 10^{-5}$ at various time t on a log-log plot.	38
2.4	(a) The variation of the regularized position-space probability density, $\Omega^{ND}(r)$ with the scaled radial distance, r/t in 3D for $D_T = 10^{-4}$ at various time t . (b) The affect of the translational diffusivity (D_T) on the regularized position-space probability density, $\Omega^{ND}(r)$ in 3D at $t = 1$. (c) The structure of $\Omega^{ND}(r)$ just behind the front ($0.99 < r < 1$) upon decreasing translational diffusivity (D_T) in 3D at $t = 1$	40
2.5	The variation of the regularized joint orientation-position space probability density, $\Omega^{ND}(r, \chi, t)$ with the scaled radial distance, r/t in 2D for various χ (a) $\chi = 0$, (b) $\chi = 2\pi/30$, (c) $\chi = 5\pi/30$, (d) $\chi = 10\pi/30$, (e) $\chi = 14\pi/30$ and (f) $\chi = 20\pi/30$; at various time t with $D_T = 10^{-3}$	42

- 2.6 The variation of the regularized orientation-position space probability density, $\Omega^{ND}(r, \chi = 0, t)$ with the scaled radial distance, $1 - r/t$ in 2D for $\chi = 0$ at various time t with $D_T = 10^{-3}$ 43
- 2.7 The effect of the translational diffusivity (D_T) on the regularized orientation-position space probability density, $\Omega^{ND}(r, \chi, t)$ in 2D at $t = 1$ for (a) $\chi = 0$ (b) $\chi = 2\pi/30$ (c) $\chi = 10\pi/30$ 43
- 2.8 The angular variation of the joint orientation-position space probability density, $\Omega^{ND}(r, \chi, t)$ with χ in 2D for various r at time (a) $t = 2$ and (b) $t = 4$ for $D_T = 10^{-3}$ 44
- 2.9 The variation of the joint regularized orientation-position space probability density, $\Omega^{ND}(r, \chi, t)$ with the scaled radial distance, r/t in 3D for various χ (a) $\chi = 0$, (b) $\chi = 2\pi/30$, and (c) $\chi = 5\pi/30$ 46
- 2.10 The variation of the joint regularized orientation-position space probability density, $\Omega^{ND}(r, \chi = 0, t)$ with the scaled radial distance, $1 - r/t$ in 3D for $\chi = 0$ for $D_T = 10^{-3}$ 46
- 3.1 The evolution of the mean-squared displacement of the passive tracer, in a suspension of pushers, with time for $U\tau/L = 50$ and $\kappa = 8$ for varying nL^3 . The inset shows the the correlated tracer diffusivity ($D_t|_{corr}$) at $O(nL^3)^2$ as a function of the run-length, $U\tau/L$, for $\kappa = 8$; the dashed lines show the asymptotic scalings discussed in the text. 64
- 3.2 The variation of the diffusivity of a passive tracer versus the volume fraction of swimmers (nL^3) for a fixed run-length $U\tau/L = 50$ and aspect-ratio $\kappa = 8$. 65
- 3.3 (a) The variation of the total fluid velocity variance, including the correlated (\mathcal{V}^c) and uncorrelated contributions (\mathcal{V}^u), for varying $nL^2U\tau$ for pushers and pullers; the velocity variance is normalized by the uncorrelated component (\mathcal{V}^u). (b) The variation of the correlated contribution (\mathcal{V}^c) to the velocity variance versus $((nL^2U\tau)_{cr}) - (nL^2U\tau)$ on a log-log plot, which shows that the power law of the divergence is $-1/2$ on approaching the threshold of collective motion for pushers; $(nL^2U\tau)_{cr} \sim 20.125$ 78
- 3.4 The spatial decay of the net fluid velocity co-variance, including the correlated and uncorrelated contributions, for varying $nL^2U\tau$ for pushers; where the velocity co-variance is normalized with corresponding velocity ($\mathcal{V}(0)$) variance and the radial distance r is non-dimensionalised by the length scale $(nL^2)^{-1}$. On approaching the threshold of collective motion $((nL^2U\tau)_{cr} \sim 20.125)$, the co-variance becomes long ranged. 79

-
- 3.5 (a) The variation of the total tracer diffusivity, including the correlated and uncorrelated contributions, of a passive tracer for varying $nL^2U\tau$ for pushers and pullers. (b) The variation of the correlated contribution (D^c) to the tracer diffusivity versus $((nL^2U\tau)_{cr}) - (nL^2U\tau)$ on a log-log plot, which shows that the power law of the divergence is $-3/2$ on approaching the threshold of collective motion for pushers; $(nL^2U\tau)_{cr} \sim 20.125$ 81
- 3.6 The variation of the nematic correlations of the swimmers orientations for varying $nL^2U\tau$ for pushers; $(nL^2U\tau)_{cr} \sim 20.125$ 82

List of tables

Chapter 1

Linear instability of Pipe and Channel flow of Dilute Polymer Solutions

Please note that the work presented in this chapter has been done in collaboration with Prof. Shankar at IIT Kanpur.

1.1 Introduction

Since the discovery by Toms that the addition of small amounts of a high molecular weight polymer to a Newtonian fluid significantly reduces the pressure drop in turbulent pipe flow [Toms, 1977; Virk, 1975], turbulent flows of dilute polymer solutions have been widely studied for both their fundamental and industrial importance [Berman, 1978; Burger et al., 1982; Lumley, 1969; Toms, 1977; Virk, 1975; White and Mungal, 2008]. Understanding the transition to turbulence in shearing flows of viscoelastic fluids, including dilute polymer solutions, is thus crucial [Graham, 2014; Morozov and van Saarloos, 2007]. A central question underlying this field of study is if the laminar state is stable to infinitesimal amplitude perturbations [Graham, 2014; Larson, 1992; Morozov and van Saarloos, 2007].

Newtonian pipe flow is known to be linearly stable at all Reynolds numbers (Re) [Drazin and Reid, 1981; Gill, 1965; Kerswell, 2005; Meseguer and Trefethen, 2003; Schmid and Henningson, 2001]. By carefully minimizing external perturbations, laminar flow has been maintained in experiments upto $Re \sim 100,000$ [Pfenniger, 1961]; in contrast, when forced with finite amplitude disturbances, transition occurs around an Re of 2000 [Avila et al., 2011; Ben-Dov and Cohen, 2007; Eckhardt et al., 2007; Hof et al., 2003; Mullin, 2011]. Theoretically, this sub-critical scenario is explained by the appearance, above a threshold Re , of non-trivial three-dimensional solutions of the Navier-Stokes equations

(termed exact coherent states) which are disconnected from the laminar state [Eckhardt et al., 2007; Kerswell, 2005; Waleffe, 1998]. Rectilinear shearing flows, including pipe flow, of dilute polymer solutions are also believed to be linearly stable at all Deborah numbers (De) in the inertialess limit ($Re = 0$) [Gorodtsov and Leonov, 1967; Larson, 1992; Renardy and Renardy, 1986; Wilson et al., 1999]; De here being the ratio of the polymer relaxation time to the flow time scale. A non-linear mechanism has been proposed for transition to (elastic) turbulence in such flows, where an initial finite amplitude perturbation induces curved streamlines, which then become unstable to a hoop-stress-driven elastic instability that operates at linear order in canonical curvilinear geometries [Bertola et al., 2003; Larson et al., 1990; Morozov and van Saarloos, 2007, 2005; Pan et al., 2013; Shaqfeh, 1996]. Theoretical work explaining transition, and turbulent drag reduction, at finite Re and De has focused on the modification of the Newtonian scenario, by mapping the domain of existence of the (simplest) exact coherent states in the Re - De plane [Graham, 2014; Roy et al., 2006; Stone et al., 2004, 2002]. That a subset of these finite amplitude solutions do not exist above a critical De , for fixed Re , is indicative of a distinct transition mechanism at larger De [Graham, 2014; Li et al., 2006]. A separate line of work has focused on the linear transient growth of disturbances from a stable laminar state [Agarwal et al., 2014; Hoda et al., 2008; Lieu et al., 2013]. In summary, the viewpoint with regard to transition in dilute polymer solutions is rooted in the (assumed) linear stability of the laminar state everywhere in the Re - De plane [Graham, 2014; Larson, 1992; Morozov and van Saarloos, 2007]. This is despite the absence of a rigorous linear stability analysis for pipe flow valid at large Re and De .

There have, however, been scattered observations that point to a linear instability in pipe flow experiments involving dilute polymer solutions. In a series of experiments in the 1960s and 70s, transition to turbulence was observed in dilute polymer solutions, at Reynolds numbers much lower than the Newtonian threshold by several groups, the phenomenon being dubbed ‘early turbulence’ [Forame et al., 1972; Goldstein et al., 1969; Hansen et al., 1973; Hansen and Little, 1974; Hoyt, 1977; Jones and Maddock., 1966; Jones et al., 1976; Little and Wiegard, 1970; Ram and Tamir, 1964; Zakin et al., 1977]. Later, Draad et al. [Draad et al., 1998] observed an order of magnitude reduction in the natural (unforced) transition Re for a polymer solution. More recently, Samanta et al. [Samanta et al., 2013] studied transition in polyacrylamide solutions, in smaller diameter pipes, thereby accessing higher Deborah numbers. In a 4 mm diameter pipe, the transition process for concentrations lesser than 200 parts per million (ppm) was analogous to the Newtonian one with forced and natural transitions occurring at disparate Reynolds numbers. In sharp contrast, for the 500 parts per million (ppm) solution, the transition occurred at $Re \sim 800$ independent of the perturbation amplitude. Further, spatially localized structures (puffs), characteristic of the

bistability associated with the Newtonian sub-critical transition [Barkley, 2016; Wignanski and Champagne, 1973; Wignanski et al., 1975], were absent. Subsequently, this new transitional pathway, connecting the laminar state to a novel elasto-inertial turbulent state, has been demonstrated over a much wider parameter range [Chandra et al., 2018, 2020; Choueiri et al., 2018].

Although a linear instability has occasionally been speculated upon [Forame et al., 1972; Graham, 2014], the consensus in the field assumes otherwise [Morozov and van Saarloos, 2007, 2005; Pan et al., 2013; Samanta et al., 2013; Sid et al., 2018b]. This assumption is sometimes stated as a fact, for instance in [Morozov and van Saarloos, 2005; Pan et al., 2013; Sid et al., 2018b]. Even the authors of Samanta et al. [2013], despite observing signatures of a linear instability, expect the transition to be governed by a non-linear process. Contrary to this widely held view we demonstrate a linear instability in the $Re-De$ plane in this chapter.

1.2 Governing Equations

We study the linear stability of the three canonical viscoelastic shearing flows - plane Couette, plane Poiseuille and pressure-driven pipe flow. The governing system of equations for an incompressible viscoelastic fluid (in non-dimensional form) is

$$Re\left(\frac{\partial}{\partial t} + \mathbf{u} \cdot \nabla\right)\mathbf{u} = -\nabla p + \frac{1-\beta}{De}\nabla \cdot \mathbf{A}_p + \beta \nabla^2 \mathbf{u}, \nabla \cdot \mathbf{u} = 0, \quad (1.1)$$

where \mathbf{u} , p and \mathbf{A}_p are the velocity field, pressure and the elastic stress tensor, respectively. The relevant non-dimensional parameters are $\beta = \frac{\mu_s}{\mu_p + \mu_s}$, $De = \frac{U_s \tau}{a}$ and $Re = \frac{\rho U_s a}{\mu_s + \mu_p}$ where μ_s and μ_p are the solvent and polymer contributions to the viscosity, τ the relaxation time of the polymer molecule, ρ the density of the fluid, a the pipe radius and U_s (the centerline velocity) the imposed velocity scale. The elastic stress is assumed to be governed by the Oldroyd-B constitutive equation, corresponding to polymer molecules in the solution being modeled as non-interacting Hookean dumbbells. This gives $\mathbf{A}_p \propto \langle \mathbf{R}\mathbf{R} \rangle$, where \mathbf{R} is the dumbbell end-to-end vector and $\langle \cdot \rangle$ denotes a configurational average. The affine deformation of \mathbf{R} , together with linear relaxation in a time τ , leads to the following equation for \mathbf{A}_p [Larson, 1988]:

$$\left(\frac{\partial}{\partial t} + \mathbf{u} \cdot \nabla\right)\mathbf{A}_p - \mathbf{A}_p \cdot \nabla \mathbf{u} - (\nabla \mathbf{u})^\dagger \cdot \mathbf{A}_p = -\frac{\mathbf{A}_p - \mathbf{I}}{De}. \quad (1.2)$$

The Oldroyd-B model predicts a shear-rate independent viscosity and first normal stress coefficient in viscometric flows [Larson, 1988]. It has been shown to reproduce observations of linear instabilities in polymer solutions in various curvilinear [Shaqfeh, 1996] and extensional flows [Poole et al., 2007] as well as the inertialess non-linear instability in rectilinear

shearing flows [Bertola et al., 2003; Morozov and van Saarloos, 2007], and is thus appropriate for a first effort. For $\beta = 0$, (1.1) and (1.2) reduce to the Upper Convected Maxwell (UCM) model, with no solvent stress contribution.

1.2.1 Laminar Flow

The laminar velocity and stress profiles for an Oldroyd-B fluid are, for plane Couette flow,

$$U = y, A_{xx} = 1 + 2De^2, A_{xy} = De, A_{yy} = 1, \quad (1.3)$$

for plane Poiseuille flow,

$$U = 1 - y^2, A_{xx} = 1 + 8De^2y^2, A_{xy} = -2yDe, A_{yy} = 1, \quad (1.4)$$

and finally for pipe flow,

$$U = 1 - r^2, A_{zz} = 1 + 8De^2r^2, A_{rz} = -2rDe, A_{rr} = 1. \quad (1.5)$$

Thus we see that the laminar velocity profile remains the same as in the Newtonian case. However, an associated first normal stress difference ($N_1 = A_{xx} - A_{yy}$ or $N_1 = A_{zz} - A_{rr}$) arises. This is owing to the polymer molecules being stretched and aligned with the flow, leading to a tension along the streamlines.

1.2.2 Formulation of the linear stability problem

We study the stability of the laminar state to infinitesimal perturbations, ($\mathbf{u} = U + \mathbf{u}'$, $\mathbf{A}_p = \mathbf{A} + \mathbf{a}'$, $p = p_0 + p'$). For plane Couette and Poiseuille flow, we assume a normal mode form for the perturbations $f' = \hat{f}(y)e^{ik(x-ct)}$ where k is the axial wavenumber. Similarly for pipe flow, the perturbations take the form $f' = \hat{f}(r)e^{ik(z-ct)}$ where k is again the axial wavenumber. Linearizing about the aforementioned base-state, one obtains the following eigenvalue problem,

$$\mathcal{L}\hat{\mathbf{f}} = c\hat{\mathbf{f}},$$

such that $c = c_r + ic_i$ where c_r is the wave speed and c_i the growth rate; $c_i > 0$ implies exponentially growing normal modes and thus an instability of the laminar state. $c \equiv c(Re, De, k, \beta)$. Therefore, the linear stability of the laminar state depends on 4 dimensionless parameters. Note that we have restricted the formulation to two dimensional (axisymmetric) perturbations here. This is not a restriction for the two planar shearing flows owing to the existence of a Squire's theorem [Bistagnino et al., 2007]. We had briefly examined three

dimensional (non-axisymmetric) perturbations for pipe flow, and found no instabilities over the parameter range of interest.

A spectral collocation method in which the perturbation fields are expanded in terms of Chebyshev polynomials is used to solve the linear eigenvalue problem [Boyd, 1999; Schmid and Henningson, 2001]. To avoid spurious modes, convergence was checked, for both eigenvalues and eigenfunctions, with respect to N (the number of Chebyshev polynomials in the spectral expansion). The only prior work on linear stability of viscoelastic pipe flow neglected the convected derivative in (1.2) and hence is of restricted validity [Hansen, 1973]. We have verified the numerical scheme by reproducing earlier stability results for plane Poiseuille flow of an Oldroyd-B fluid [Sureshkumar and Beris, 1995b; Zhang et al., 2013] and for Newtonian pipe flow [Schmid and Henningson, 2001]. We also verified our linear stability results against those provided by Prof. Shankar and his students, who have also examined the same problem using two distinct numerical approaches.

1.3 Linear Instability

1.3.1 Pipe flow

We first discuss the stability of pipe flow. The eigenvalue spectrum in figure 1.1, for $Re = 800, De = 65, \beta = 0.65, k = 1$, shows a single unstable mode, multiple damped discrete modes and a pair of continuous spectra (these appear as balloons due to the finite discretization). The continuous spectrum eigenvalues are given by $c = U - i/(kDe)$ and $c = U - i/(\beta kDe)$, with the first set corresponding to singular modes whose decay rates are set by the polymeric stress relaxation [Graham, 1998; Grillet et al., 2002; Kupferman, 2005; Sureshkumar and Beris, 1995b; Wilson et al., 1999; Zhang et al., 2013]. The unstable mode is an axisymmetric center-mode propagating at a speed close to the base-state maximum. Figure 1.2 shows the associated perturbation velocity and polymer force density ($\nabla \cdot \mathbf{a}'$) fields. The polymer force field is localized near the centerline and reinforces the velocity field, leading to the instability.

Figure 1.3 shows the numerically obtained neutral curves, which mark the region of existence of the instability in the $Re-De$ plane for varying β and a fixed wavenumber (k). For $Re, De \rightarrow \infty$, the neutral curves follow the scaling $De \sim Re^{1/2}$ at a given β and k . The unstable region in the $Re-De$ plane is seen to be highly sensitive to the viscosity ratio. To further examine the dependence on β , Figure 1.4 shows the variation of the unstable eigenvalue for varying De and β with Re and k fixed. Even at very high solvent viscosities ($\beta \rightarrow 1$), the instability survives with $De \sim (1 - \beta)^{-1}$, which ensures that both solvent and polymeric stresses stay comparable.

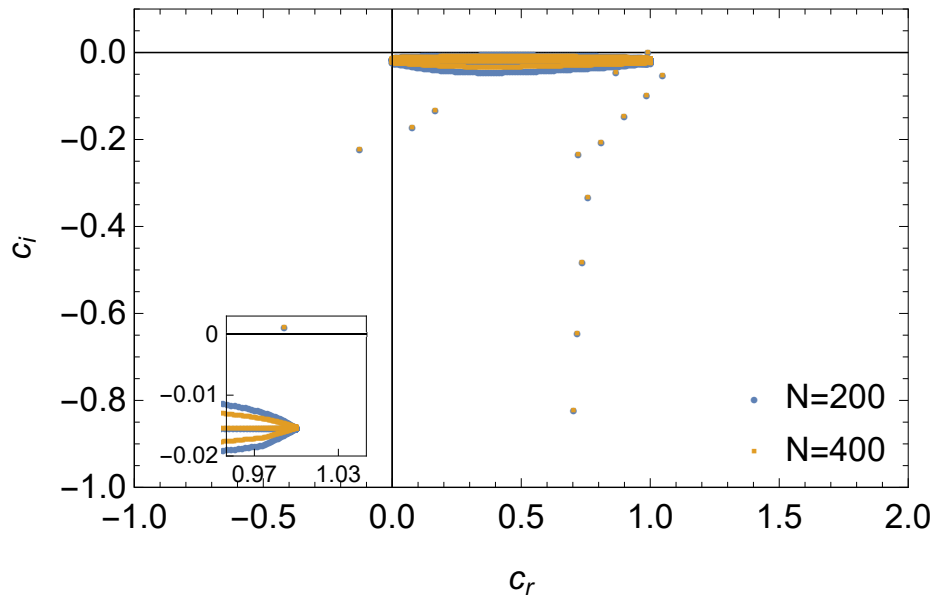


Fig. 1.1 Numerically obtained eigenspectrum for pipe flow of an Oldroyd-B fluid for $Re = 800, De = 65, \beta = 0.65$ and $k = 1$ (for $N = 200$ and 400); the inset zooms into the region around the unstable mode.

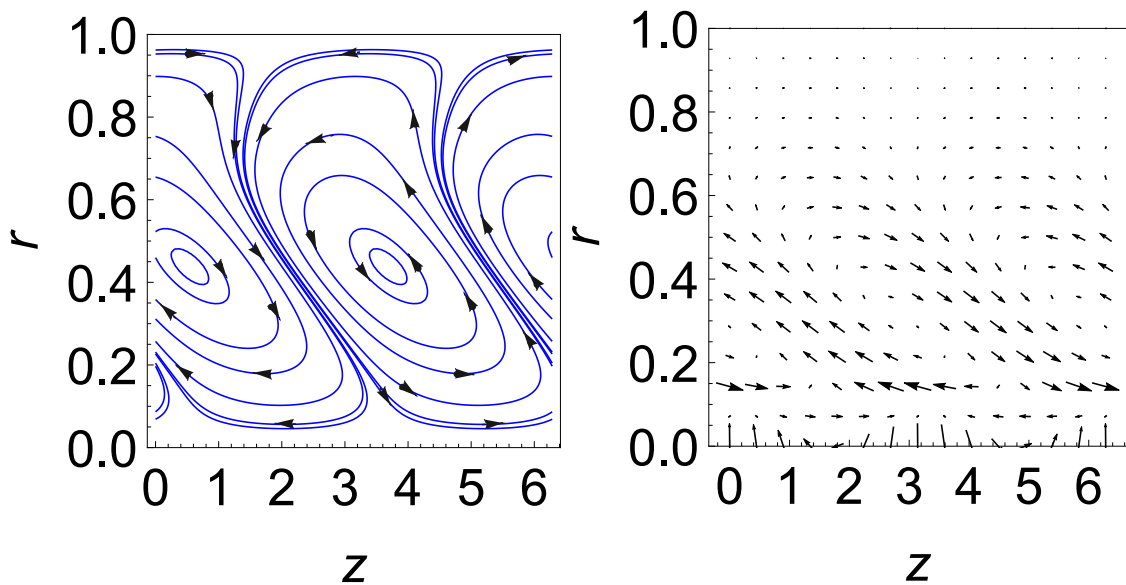


Fig. 1.2 Perturbation velocity (left) and polymer force (right) fields for the unstable mode for $Re = 800, De = 65, \beta = 0.6$ and $k = 1$.

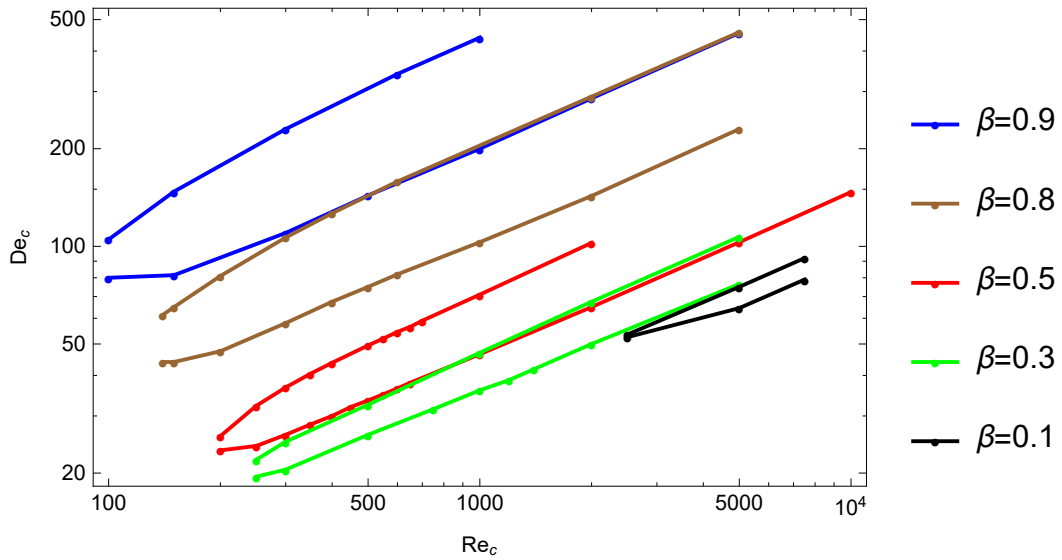


Fig. 1.3 The numerically obtained neutral curves for pipe flow for varying β with $k = 1$.

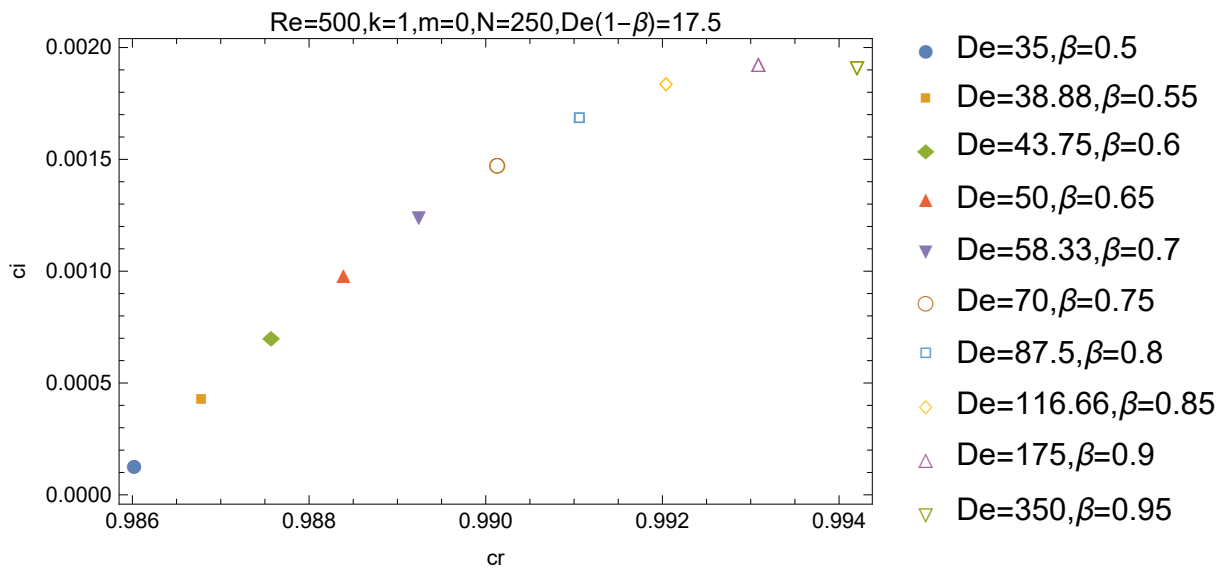


Fig. 1.4 Tracking the unstable mode with varying De and β with Re , k and $De(1 - \beta)$ fixed for pipe flow.

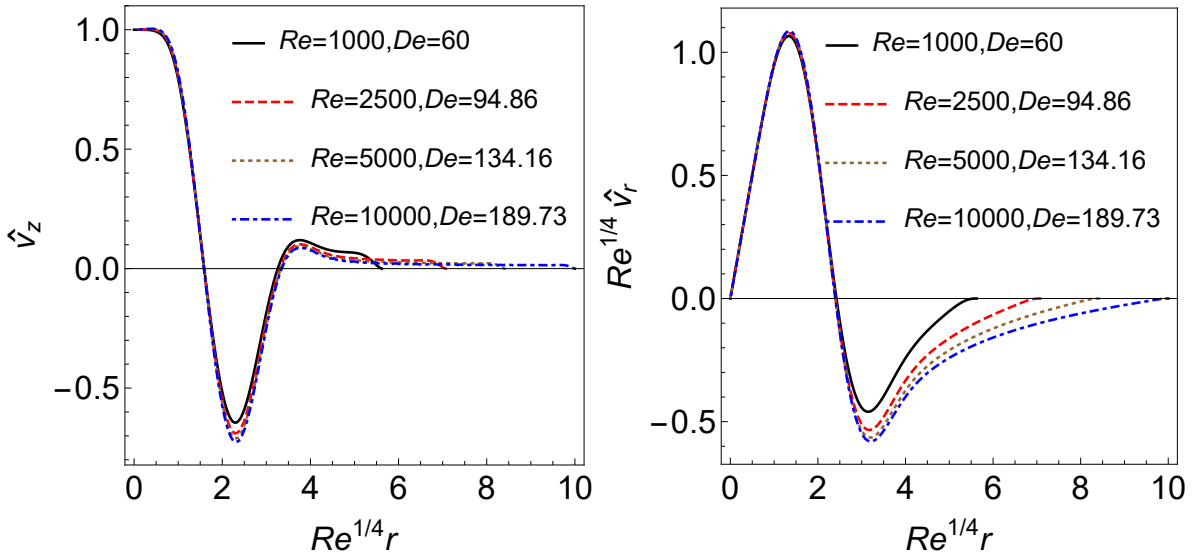


Fig. 1.5 The unstable center-mode eigenfunctions for the axial velocity (left) and radial velocity (right) in scaled boundary-layer coordinates in the limit $Re \rightarrow \infty$ and $De \rightarrow \infty$ for a fixed $De/Re^{1/2}$ ($k = 1$ and $\beta = 0.5$).

Figure 1.5 shows the appropriately scaled axial and radial velocity eigenfunctions for the unstable center mode, for varying parameters. In the limit $Re, De \rightarrow \infty$ with $De/Re^{1/2}$ (and k) fixed, the unstable eigenfunctions become increasingly localized in a boundary layer of $\mathcal{O}(Re^{-1/4})$ around the centerline (figure 1.5). Viscous diffusion balances inertia in this boundary layer, analogous to a Newtonian center-mode [Gill, 1965], and for the perturbation polymeric stress to stay comparable requires $De \sim \mathcal{O}(Re^{1/2})$. The instability thus requires a balance of inertia, viscous and elastic polymer stresses close to the centerline. The centerline localization is in contrast to the original Newtonian and the elastically modified Tollmien-Schlichting instability for plane Poiseuille flow, where the eigenfunction is localized near the channel walls for large Re [Schmid and Henningson, 2001; Sureshkumar and Beris, 1995b; Zhang et al., 2013].

1.3.2 Plane Poiseuille flow

Figure 1.6 shows the elastoinertial eigenspectrum for plane Poiseuille flow. A center-mode instability is also seen to exist in this case. Further, the results in Figures 1.7 and 1.8 show that the instability dynamics and physical mechanism is very similar to that of pipe flow case discussed earlier. Once again we see the crucial role played by the parameter β in delineating the region of instability. Figure 1.9 shows the unstable eigenfunctions for plane Poiseuille flow. Similar to the earlier case, we see the emergence of a boundary layer at the centerline where polymeric, viscous and inertial forces balance.

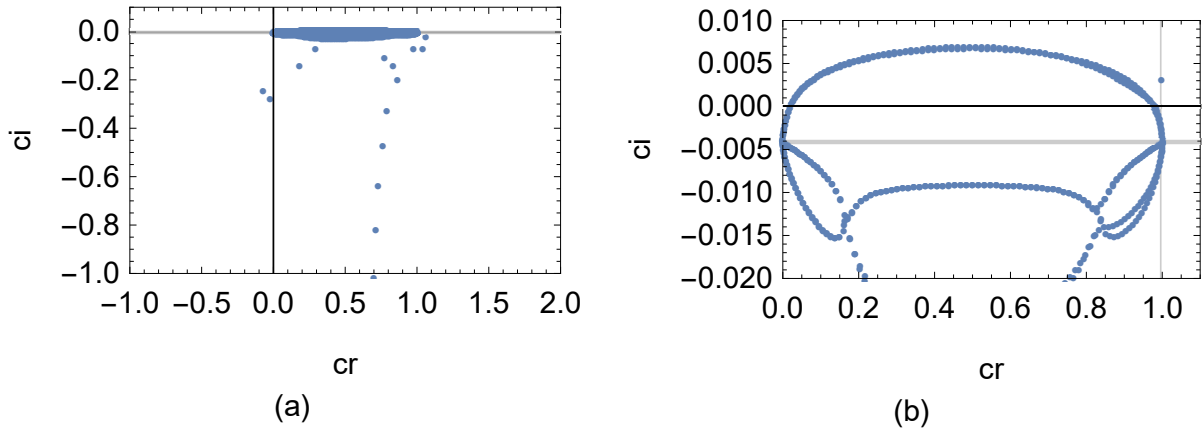


Fig. 1.6 Numerically obtained eigenspectrum for plane Poiseuille flow of an Oldroyd-B fluid for $Re = 300, De = 250, k = 1$ and $\beta = 0.95$.

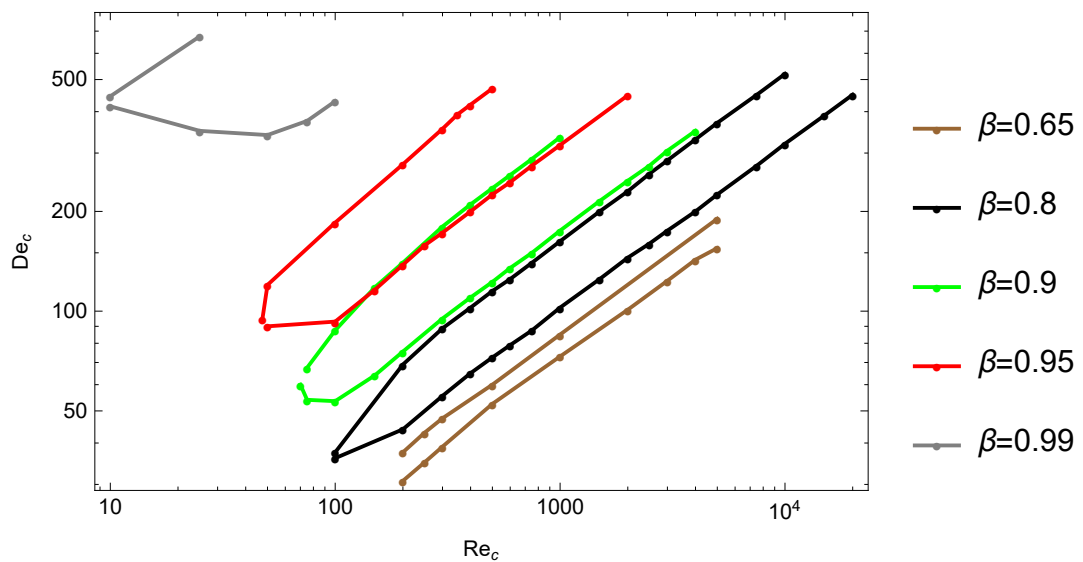


Fig. 1.7 The numerically obtained neutral curves for plane Poiseuille flow for varying β with $k = 1$.

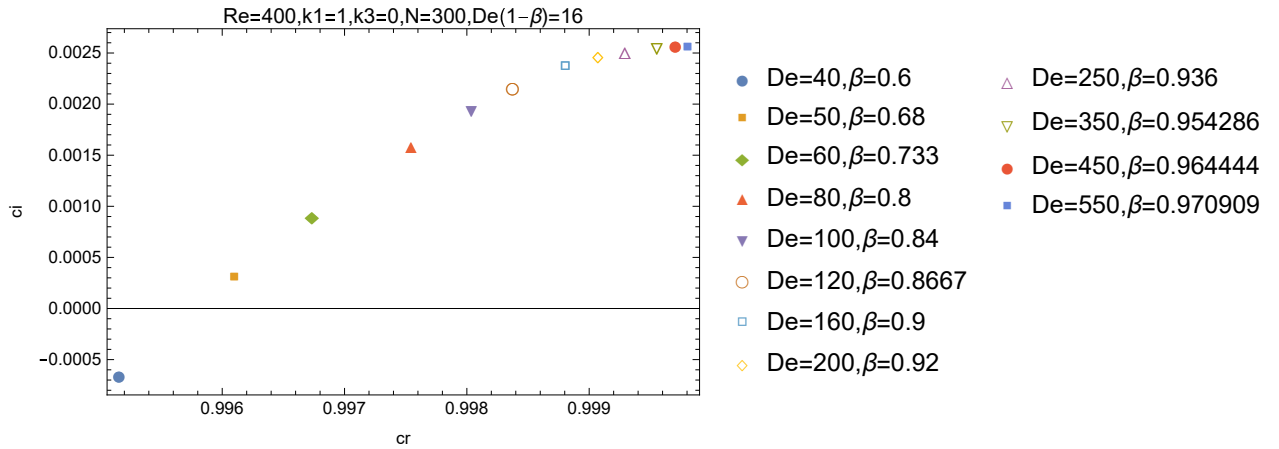


Fig. 1.8 Tracking the unstable mode with varying De and β with Re , k and $De(1 - \beta)$ fixed for plane Poiseuille flow.

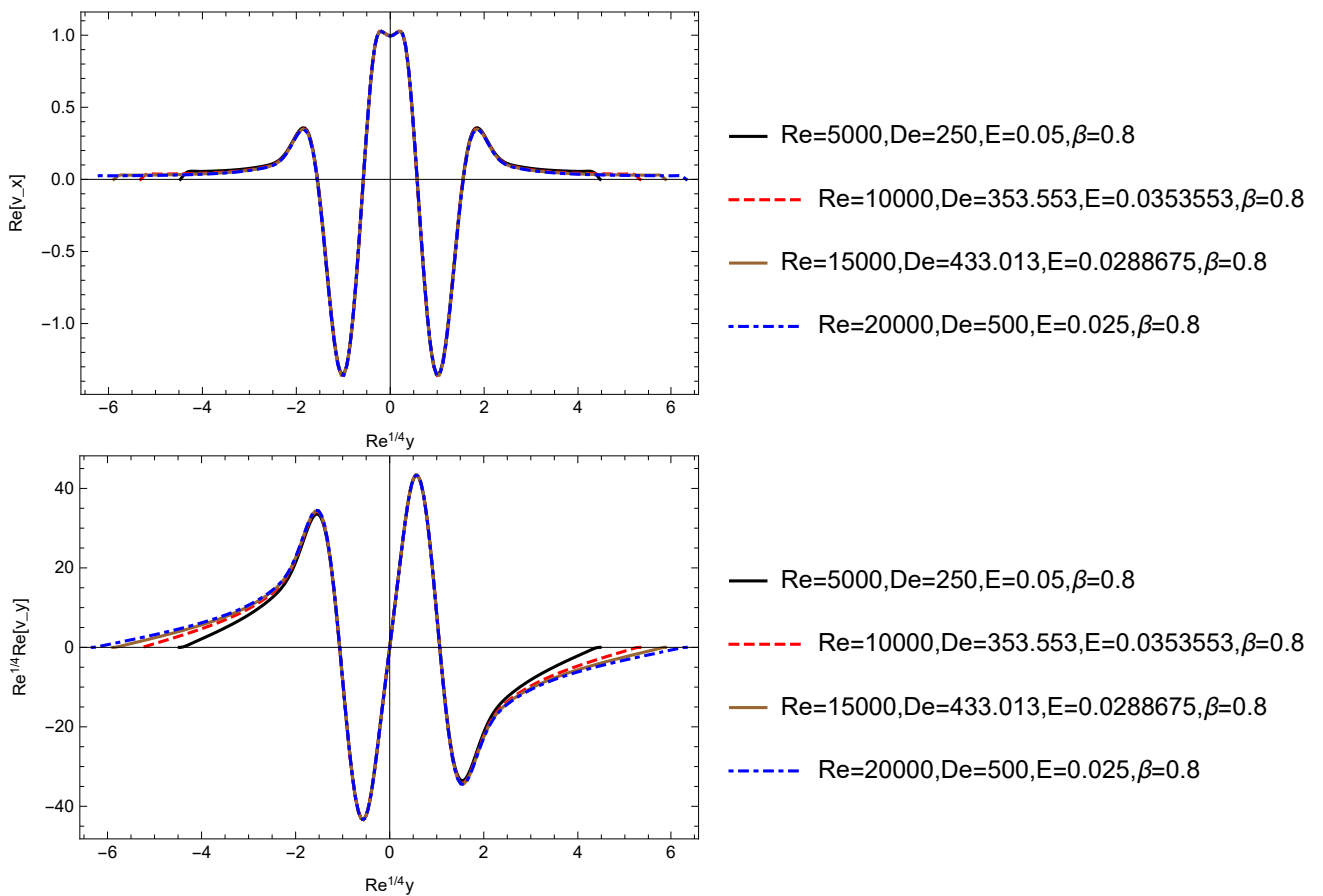


Fig. 1.9 The unstable center-mode eigenfunctions for the tangential velocity (top) and normal velocity (bottom) in scaled boundary-layer coordinates in the limit $Re \rightarrow \infty$ and $De \rightarrow \infty$ for a fixed $De/Re^{1/2}$ ($k = 1$ and $\beta = 0.8$) for plane Poiseuille flow.

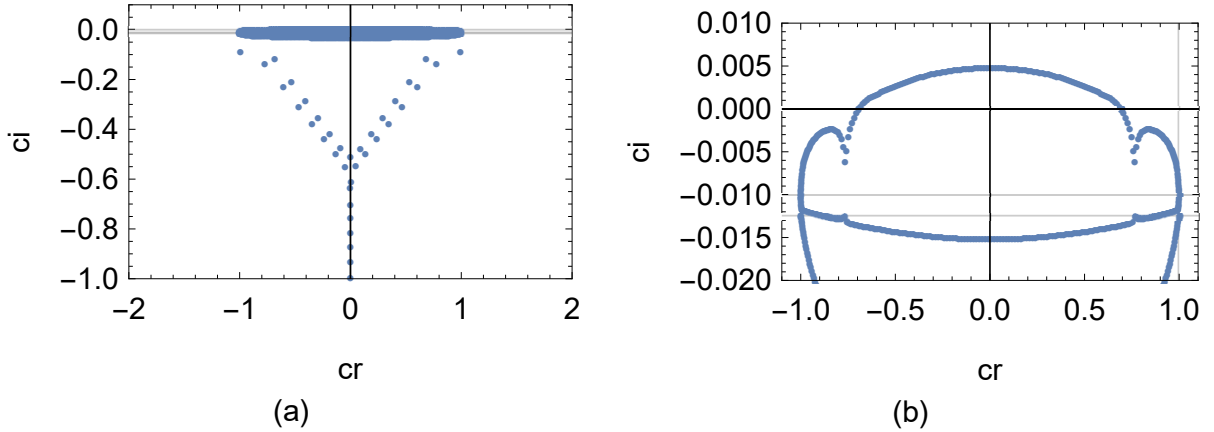


Fig. 1.10 Numerically obtained eigenspectrum for plane Couette flow of an Oldroyd-B fluid for $Re = 2500$, $De = 100$, $k = 1$ and $\beta = 0.8$.

1.3.3 Plane Couette flow

Finally, figure 1.10 shows the eigenspectrum for plane Couette flow which was found to be stable at all Re and De values examined.

1.3.4 Inclusion of stress diffusivity for pipe flow

Artificial stress diffusion is often used for regularization when simulating viscoelastic flows to ensure that the stress tensor remains positive definite [Sureshkumar and Beris [1995a], Sureshkumar et al. [1997], Lopez et al. [2019]]. Recently, it has been shown that this additional diffusivity can artificially impact the stress dynamics [Gupta and Vincenzi, 2019], even suppressing elasto-inertial turbulence [Sid et al., 2018a]. In this section, we thus briefly examine the effect of stress diffusion on the onset of the center mode instability. The polymeric stress equation takes the form,

$$W \left(\frac{\partial \mathbf{T}}{\partial t} + (\mathbf{v} \cdot \nabla) \mathbf{T} - \mathbf{T} \cdot (\nabla \mathbf{v}) - (\nabla \mathbf{v})^T \cdot \mathbf{T} \right) + \mathbf{T} + \frac{D\lambda}{R^2} \nabla^2 \mathbf{T} = \frac{1-\beta}{Re} \{ \nabla \mathbf{v} + (\nabla \mathbf{v})^T \}, \quad (1.6)$$

where D is the stress diffusivity. El-Kareh and Leal [1989] showed that the stress diffusion term results from the translational diffusion of the polymer molecules and estimated the diffusivity $D \sim 10^{-12} m^2/s$.

The linearized equations for the perturbations are derived following section 2 and solved using a spectral method. Additional boundary conditions are now required for the stress components. At the pipe wall ($r = 1$), the stress equation is imposed without the diffusivity, while the regularity condition for the stress is imposed at the centerline [Beris and

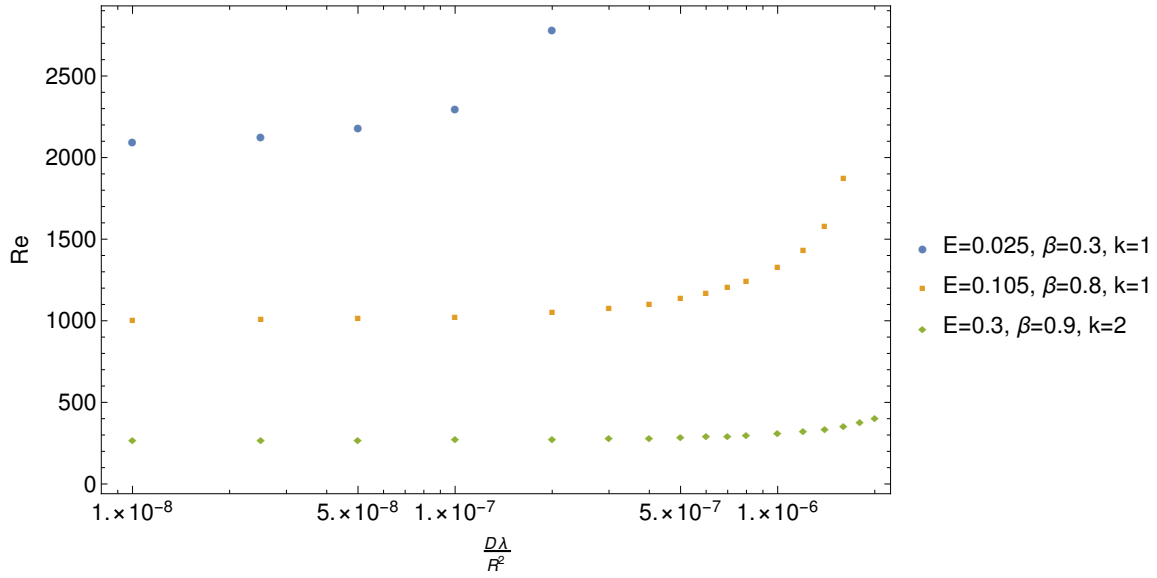


Fig. 1.11 The effect of stress diffusion ($D\lambda/R^2$) on the onset Re for pipe flow for different E , β and k values.

[Dimitropoulos, 1999; Lopez et al., 2019]. The addition of stress diffusivity regularizes the continuous spectrum modes and leads to an additional family of diffusive, stable modes with increasing decay rates. The decay rate of this family of modes increases with increasing stress diffusion as characterized by the dimensionless parameter $D\lambda/R^2$ that appears in 1.6. However, the modes that exist even in the absence of stress diffusion are only regularly perturbed for small values of the diffusivity ($D\lambda/R^2 \rightarrow 0$).

Figure 1.11 shows that the stress diffusivity has a stabilizing effect, as the onset Re increases with increasing diffusivity ($D\lambda/R^2$). For $D\lambda/R^2 \rightarrow 0$, the onset threshold becomes independent of the diffusivity whereas the instability ceases to exist at a finite $D\lambda/R^2$. The threshold diffusivity for stabilization is also seen to depend on E and β (see figure 1.11). The instability thus continues to exist for the experimentally relevant values of $D\lambda/R^2 \sim 10^{-10} - 10^{-8}$ [El-Kareh and Leal, 1989]. However, the much larger values of $D\lambda/R^2 \sim 10^{-4} - 10^{-2}$ especially used in the early numerical simulations [Sureshkumar and Beris, 1995a; Sureshkumar et al., 1997] suppress the instability. Thus, simulation techniques which do not impose a large artificial diffusivity [Singh et al., 2011, 2022] are required to access the phase-space structures associated with the center-mode instability.

1.4 Weakly non-linear analysis

The dynamics at the onset of the center-mode instability can be further understood by undertaking a weakly non-linear analysis. Near the threshold of the instability, we can derive an equation for the amplitude (A) of the dominant unstable mode, such that

$$\partial_t A = cA + a_3 A^3. \quad (1.7)$$

Thus, the (Stuart-)Landau coefficient (a_3) is the crucial element in the weakly non-linear analysis. If $a_3 > 0$, a stationary solution for the amplitude (A) does not exist and the instability dynamics must be sub-critical in nature. On the other hand, if $a_3 < 0$ a saturated non-linear solution exists near the onset threshold and the dynamics are super-critical. To solve for a_3 , we need to find the eigenfunction (e^{ikx}), the associated second harmonic (e^{2ikx}), the mean modification (e^{0ikx}) and the adjoint. The corresponding linear problems for each of the harmonics are solved using spectral collocation methods. Our numerical results are validated by comparing with [Morozov and Van Saarloos \[2019\]](#) for varying De and Chebyshev polynomials used, with $Re = 0$, $\beta = 0.05$, $k_x = 1$, $k_z = 2$. We see a reasonable agreement as shown below,

De	$N = 100$	$N = 250$	$N = 400$	Morozov et al. (2019)
2	9.4881	9.4767	9.4756	9.5015
2.8	8.2216	8.2266	8.2282	8.0893
3.6	6.5493	6.5478	6.5475	6.3819

Figures [1.12](#) and [1.13](#) show the mean axial velocity and stress for the weakly non-linear solution at onset for $Re = 50$, $De = 90$, $\beta = 0.95$ and $k = 1$. The stress shows enhanced localisation and structure near the centerline, in agreement with the results of the linear analysis. Such stress localisation is likely susceptible to inertio-elastic instabilities which would provide a pathway towards turbulence [[Baumert and Muller, 1999](#); [Roy et al., 2022](#)]. The structure of the mean stress is reminiscent of recent simulations of elasto-inertial turbulence (for plane Poiseuille flow) wherein regions of high polymer stretch, localized in the gradient direction, were observed [[Dubief et al., 2013](#); [Samanta et al., 2013](#); [Sid et al., 2018b](#)]. However, an exact connection with the weakly non-linear results in this section is not obviously clear.

First, we examine the Landau coefficient at the onset of the instability for a given elasticity number $E = De/Re$ and viscosity ratio (β). For fixed E and β , the onset is determined by a critical Reynolds number (Re_c) with an associated critical wavelength (k_c). The set of Re_c - k_c

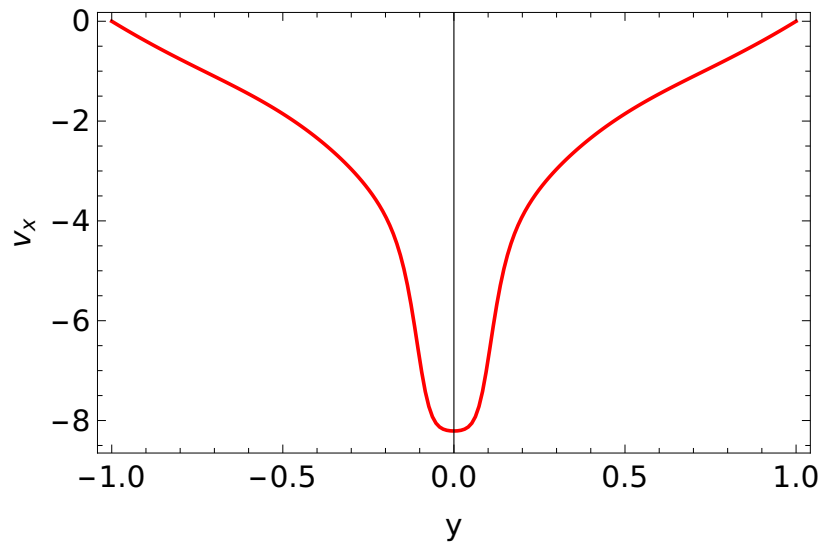


Fig. 1.12 The mean axial velocity profile (v_x) at the onset for $Re = 50$, $De = 90$, $\beta = 0.95$ and $k = 1$.

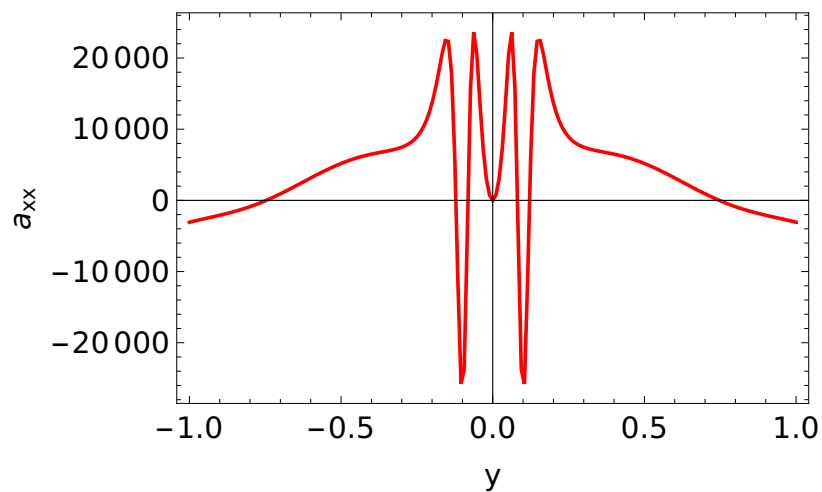


Fig. 1.13 The profile for the stream-wise component of the mean normal stress a_{xx} at the onset for $Re = 50$, $De = 90$, $\beta = 0.95$ and $k = 1$.

values were provided by Prof. Shankar and his students. Here, we find out the nature of the instability at onset for these parameters by obtaining the Landau coefficient. For $\beta = 0.65$, the Landau coefficient (a_3) for different (Re_c - k_c) pairs, and along a sequence of increasing E , is given by,

Re_c	E	k_c	a_3
1870.22	0.04	1.9621	-9.3387
1016.11	0.06	1.6036	-3.8523
657.37	0.08	1.3923	-2.1091
473.19	0.1	1.2389	-1.3645
341.18	0.12	1.1671	-0.8053
230.51	0.14	1.1985	-0.3604
159.29	0.18	1.0749	-0.3465
187.02	0.2	0.7975	-0.3291
246.83	0.21	0.5713	-0.2496

The instability is seen to be super-critical at these parameter values. For $\beta = 0.98$, the Landau coefficient (a_3), again for different (Re_c - k_c) pairs, is found to be as follows,

Re_c	E	k_c	a_3
107.512	1.5	3.3640	-3101.2595
67.991	2	2.7830	3421.1401
48.812	2.5	2.4519	637.3097
39.678	3	2.2760	459.6215
31.237	4	2.0090	246.3439
27.248	5	1.7910	150.5509
22.802	8	1.3035	52.7459
22.398	10	1.0559	30.7717
30.384	15	0.5155	8.3401

The instability is seen to be mostly sub-critical at higher β , pointing to the importance of the viscosity ratio (β) in determining the nature of the instability at onset.

Recall that, for fixed β and k , the neutral curves approach an $Re \propto De^{1/2}$ scaling form, along which the eigenfunctions collapse to within an interval of $O(Re^{-1/4})$ near the centerline. One could try to see if a similar scaling is seen for the Landau coefficient (a_3) along the neutral curves, and figure 1.14 therefore shows the variation for the Landau coefficient along the neutral curves in the $Re - De$ plane. We see that, unlike the eigenfunctions, the

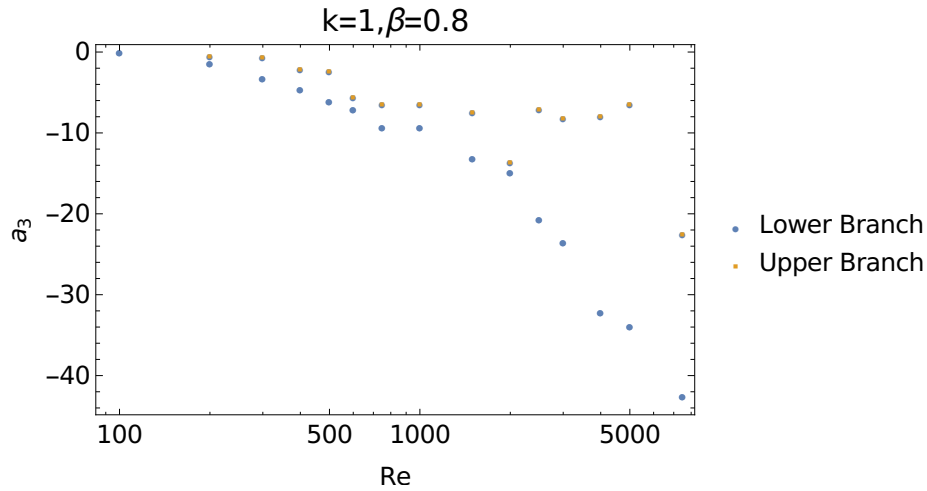


Fig. 1.14 Variation of the Landau coefficient (a_3) along the two branches of the neutral curves in the $Re - De$ plane for $k = 1$ and $\beta = 0.8$.

Landau Coefficient does not display any consistent pattern along the $Re - De^{1/2}$ neutral curve. Finally we consider the variation of the Landau coefficient with De as one moves away from the neutral curve with the other parameters being fixed in figure 1.15. For the particular choice of parameters, at larger De , the instability tends to be sub-critical. With the various parametric combinations examined here, we see that there is no distinct pattern for the Landau coefficient in the 4-dimensional parameter space ($Re - De - \beta - k$) that governs the instability.

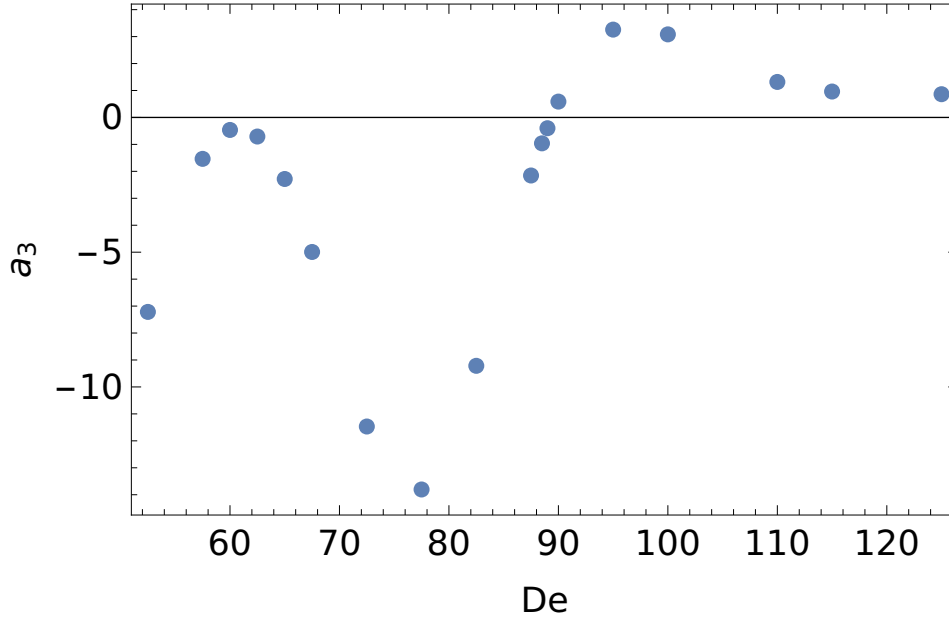


Fig. 1.15 Variation of the Landau coefficient (a_3) with De with the other parameters fixed at $Re = 300, \beta = 0.8, k = 1$.

1.5 Discussion on the importance of the center-mode instability

The centermode instability is predicted to exist over a wide range of Re , even as low as 10-100 (see Figure 1.7). The regime $Re_c \sim \mathcal{O}(100)$, $E \sim \mathcal{O}(1)$ is achievable in microfluidic devices [Ram and Tamir, 1964; Srinivas and Kumaran, 2017]. For (E, β) values such that Re_c is $\mathcal{O}(2000)$ or greater, pertinent to macroscopic geometries, the sub-critical Newtonian transition might mask the linear instability unless external perturbations are carefully minimized. A natural transition Re of around 8000 was reported by Draad et al. [1998] for a 20 parts per million (ppm) solution of partially hydrolysed polyacrylamide in demineralized water ($\beta \sim 0.1$ based on the zero shear viscosity); as opposed to the much higher transition Re of 60,000 for Newtonian fluids for their experimental facility. Our calculations do yield an unstable mode at the corresponding Re and β , for $E = 0.01$, although the strong shear thinning exhibited by the solution prevents a quantitative comparison. Similar observations of a significantly lower natural transition Re have been reported for dilute solutions of polyethylene oxide [Paterson and Abernathy., 1972]. The instability also qualitatively explains the observations of ‘early turbulence’ in Forame et al. [1972]; Goldstein et al. [1969]; Hansen and Little [1974]; Jones and Maddock. [1966]; Little and Wiegard [1970]; Ram and Tamir [1964]. For the 500 ppm polyacrylamide solution used by Samanta et al. [2013], $\beta = 0.65$.

The Re_c for the instability at this β is well below that at which Newtonian turbulence sets in. This is in qualitative agreement with the experiment where transition was reported at $Re \sim 800$. However, the minimum E required for the center-mode instability is around 0.05, which is an order of magnitude larger than the experimentally reported value of 0.004, based on a measurement of the relaxation time using a capillary break-up elongational rheometer (CaBER). This discrepancy may be attributed to the known difficulty in associating the time inferred from CaBER measurements to the relaxation rate relevant to the Oldroyd-B model [Clasen et al., 2006; Neelamegam et al., 2013; Samanta, 2013; Srinivas and Kumaran, 2017; Zell et al., 2010]. The $(Re-De-\beta)$ dependent threshold of the center-mode instability calls for a re-examination of the expectation that early transition, even in the absence of finite amplitude perturbations, is governed by a critical De , regardless of Re [Ram and Tamir, 1964; Samanta et al., 2013]. Observations of pressure-driven flow through a channel of a polyacrylamide solution becoming turbulent at $Re \sim 350$, $De \sim 250$ and $\beta = 0.92$ were reported in Srinivas and Kumaran [2017]. A center-mode instability exists at these parameter values.

Recently Choueiri et al. [2021] have studied the transition in a 600 ppm polyacrylamide solution in a water-glycerol mixture, ensuring a lower viscosity ratio ($\beta = 0.5$) than was generally used in similar experiments in the literature earlier. Thus, the importance of the viscosity ratio parameter, as the results in this chapter indicate, has been experimentally seen. They have verified that the dynamics at the onset of "elasto-inertial turbulence" are indeed controlled by the center-mode instability studied in this chapter. Further the experiments observed transition even at Re values lower than that predicted by the linear analysis, thus suggesting that for certain parameters the onset can still be dominated by non-linear dynamics, which would point to the importance of the weakly-non linear analysis in section 1.4.

The instability described in this chapter should form the first step in a new pathway to turbulence, and the maximum drag reduction (MDR) asymptote, in dilute polymer solutions. The absence of bistability, characteristic of the Newtonian scenario [Avila et al., 2011; Barkley, 2016], implies very different transitional dynamics. Complementing recent experimental [Choueiri et al., 2018; Samanta, 2013] and numerical efforts [Dubief et al., 2013; Sid et al., 2018b], ours is the first theoretical work that points to a state of elasto-inertial turbulence (EIT) with novel spatiotemporal dynamics, particularly at large De , underlying the MDR asymptote. At the linear instability threshold, elasto-inertial traveling wave solutions, associated with the unstable center-mode eigenfunctions, would be created in a Hopf bifurcation from the laminar state [Barkley, 1990; Soibelman and Meiron, 1991]. These traveling wave solutions and associated phase space structures are expected to be relevant for describing both EIT and MDR dynamics [Choueiri et al., 2018; Dubief et al., 2013;

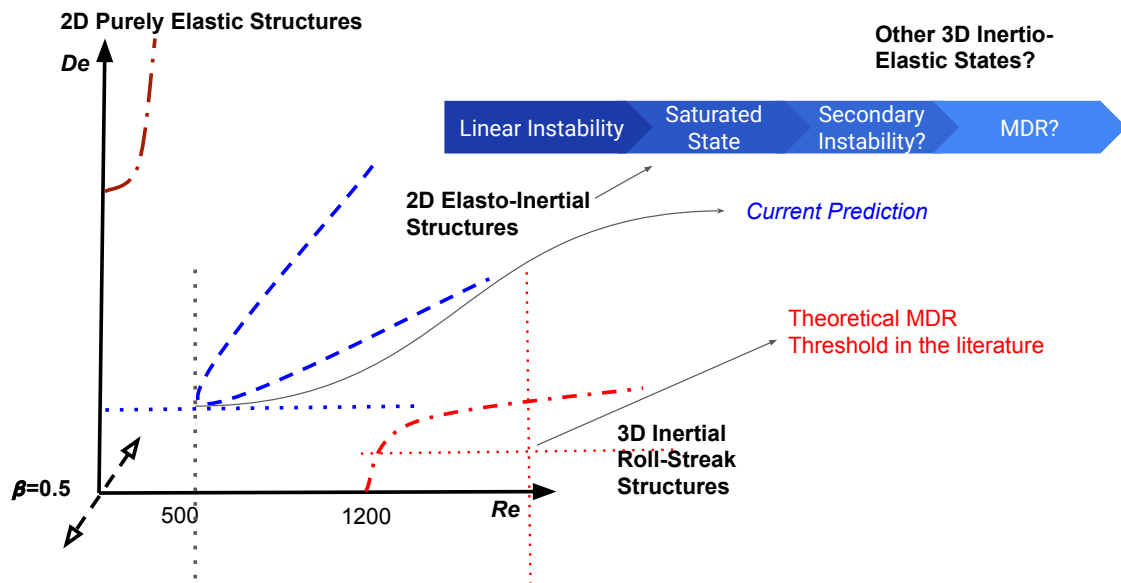


Fig. 1.16 Schematic showing the various possible dynamics in the Re - De plane when accounting for the novel transition pathway examined in this chapter.

[Samanta, 2013; Sid et al., 2018b]. Further the radial structure of the polymer forcing in the unstable mode is reminiscent of recent simulations of elasto-inertial turbulence (for plane Poiseuille flow) wherein regions of high polymer stretch, localized in the gradient direction, were observed; however in the simulations these were observed closer to the walls unlike what the linear stability results predict [Dubief et al., 2013; Samanta et al., 2013; Sid et al., 2018b]. The implied contrast between the state space for viscoelastic pipe flow and the Newtonian one has fundamental consequences for the dynamical systems interpretation of the maximum drag reduction state which, currently, crucially relies on a similarity between the two [Graham, 2014; Roy et al., 2006; Sid et al., 2018b; Stone et al., 2002; Xi and Graham, 2012]. Figure 1.16 sketches out a schematic summarizing how the various dynamics are likely to be distributed in the parameter-space.

The general mechanism will be applicable to inertial flows of other viscoelastic fluids such as wormlike micellar surfactant solutions which show drag reduction [Samanta, 2013; Zakin et al., 1998]. Practically, a detailed understanding of the transitional pathway associated with the instability would help develop control strategies to induce early (or delayed) transition to turbulence, which would be of special relevance to microfluidic devices [Hong et al., 2016; Kumaran, 2015; Li et al., 2012; Lim et al., 2014; Squires and Quake, 2005].

Chapter 2

Exact solution for the probability density of run-and-tumble particles

2.1 Introduction

Recent years have seen an enormous interest in the study of active matter systems where constituent particles, at the micro-scale, break the time-reversal symmetry [Bechinger et al., 2016; Cates, 2012; Doostmohammadi et al., 2018; Marchetti et al., 2013]. Consequently, active matter systems show a host of surprising behavior ruled out in equilibrium [Kurchan, 2009]. To mention a select few, these include, large-scale collective motion and flocking [Koch and Subramanian, 2011; Marchetti et al., 2013; Vicsek and Zafeiris, 2012], novel forms of phase-separation [Cates and Tailleur, 2015; Cates and Tjhung, 2018; Chaté, 2020], and surprising material properties [Ben Dor et al., 2018; Dufresne, 2019; Saintillan, 2018]. Understanding the origins of the aforementioned phenomena in terms of the underlying constituents of such systems is therefore of immense interest.

Swimmers that instantaneously swim with an orientation (\boldsymbol{p}) are the elementary constituents of a wide-class of active systems [Bechinger et al., 2016; Elgeti et al., 2015; Lauga and Powers, 2009; Subramanian and Nott, 2011]. Based on the stochastic dynamics of the orientation vector (\boldsymbol{p}) such particles have been further classified into Active Brownian Particles (ABPs) and Run-and-Tumble Particles (RTPs) [Bechinger et al., 2016; Cates and Tailleur, 2015; Romanczuk et al., 2012]. For ABPs, the rate of change of orientation is subject to a white noise term, and thus evolves in a continuous manner through infinitesimal changes on the unit-sphere. In contrast, RTPs, the focus of this chapter, swim along straight trajectories (the run phase) before executing an impulsive stochastic reorientation (the tumble phase) with the orientation changing by a large amount [Berg, 1993]. The reorientation

event is generally assumed to follow Poissonian statistics with a mean tumble time τ . In the biological context, several species of bacteria exhibit run-and-tumble motion, as shown in the seminal work of Berg and co-workers [Berg, 1993, 2008; Berg and Brown, 1972; Koch and Subramanian, 2011; Lauga, 2016]. It was recently shown that certain algae also execute run-and-tumble motion [Bennett and Golestanian, 2013; Goldstein, 2015; Polin et al., 2009; Wan and Goldstein, 2018]. Some artificially constructed colloidal microswimmers have also been seen to behave as RTPs [Ebbens et al., 2010; Karani et al., 2019; Lozano et al., 2018].

The widespread relevance of the RTP paradigm, for the micro-scale motion of both biological and synthetic swimmers, has thus inspired a large amount of work studying their dynamics (see for instance Angelani [2013]; Detcherri [2015]; Dhar et al. [2019]; Ezhilan et al. [2015]; Malakar et al. [2018]; Martens et al. [2012]; Sevilla et al. [2019]; Solon et al. [2015]; Tailleur and Cates [2009]; Thompson et al. [2011]; Wang et al. [2014]). Despite such extensive interest, almost no analytical solutions are available describing the dynamics of RTPs even in the absence of interactions. The joint-probability density ($\Omega(\mathbf{r}, \mathbf{p}, t)$) of finding a run-and-tumble particle at position \mathbf{r} with orientation \mathbf{p} at a given time t is governed by an integro-differential equation in two and higher dimensions (see section 2.2.1). Thus, analytical approaches are usually limited to one-dimension, where the orientation vector takes only two discrete values [Ben Dor et al., 2018; Dhar et al., 2019; Malakar et al., 2018; Tailleur and Cates, 2009]. The one dimensional case is unique since an exact closed form solution can be obtained [Othmer et al., 1988; Schnitzer, 1993]. In higher dimensions, prior studies have mostly focused on the position-space probability density ($\Omega(\mathbf{r}, t)$) of finding a particle at position \mathbf{r} with any orientation \mathbf{p} . For instance, Martens et al. [2012] used an analogy with the Lorentz-gas model to derive an analytical expression for $\Omega(\mathbf{r}, t)$ in two dimensions. Alternatively, in the long-time limit, the dynamics of RTPs may be studied using either a moment-hierarchy approach [Ezhilan et al., 2015; Yan and Brady, 2015] or a multiple-scales analysis [Vennamneni et al., 2020]. However, these methods only give limited information about the joint orientation-position dynamics owing to the assumed separation of scales, and one expects the short-time dynamics in particular to show distinct behavior.

Moving beyond the aforementioned limitations, in this chapter we provide the exact solution for the joint orientation-position space probability density of RTPs in the absence of an imposed external field for both 2D and 3D. Obtaining the exact solution requires a detailed knowledge of the spectrum of the integro-differential run-and-tumble operator. We show that this eigenspectrum has both a continuous spectrum and discrete modes. We derive analytical expressions for the eigenfunctions (and their adjoints) of the run-and-tumble operator, governing $\Omega(\mathbf{r}, \mathbf{p}, t)$, in Fourier space (section 2.2.2 and 2.2.3). Using a bilinear superposition of the discrete and adjoint eigenfunctions, we then construct the exact

Green's function of the run-and-tumble operator (section 2.2.4). The Green's function, when interpreted as probability density, denotes the evolution of a population of RTPs from a delta function initial condition in orientation-position space. Via a convolution integral with the Green's function as a kernel one may study the evolution of the joint-probability density from an arbitrary initial condition. In section 2.3, we present results for the evolution of the joint probability density in orientation-position space. Our results are valid at all length and time-scales, and therefore yield complete information about the joint orientation-position space probability density. We also show that our approach exactly recovers earlier limiting results in two-dimensions derived by Martens et al. [2012], thus validating our eigenfunction superposition. We show that the radial variation of $\Omega(\mathbf{r}, \mathbf{p}, t)$ undergoes a transition from an active to passive-regime with increasing time for any orientation \mathbf{p} . Further, our approach allows us to study the regularizing effect of a finite translational diffusivity. We summarize our results and briefly discuss possible extensions in section 2.4. At the end, section 2.5 gives the exact steps for the detailed derivation of the adjoint eigenfunctions that are needed for the Green's function.

2.2 The run-and-tumble operator

2.2.1 Governing Equation

We examine run-and-tumble particles (RTPs) which swim in a given direction (\mathbf{p}) with a finite speed U_s (the run event) whereafter they randomly reorient (the tumble event), changing their swimming direction in the process (the new run event). The tumbles are assumed to be instantaneous, and obey Poissonian statistics with the average time between two tumbles being τ [Berg, 2008; Berg and Brown, 1972; Lauga, 2016; Subramanian and Koch, 2009]. For such RTPs in the absence of interactions induced by their disturbance fields, the joint-probability density, $\Omega(\mathbf{r}, \mathbf{p}, t)$, of finding a swimmer at position \mathbf{r} with orientation \mathbf{p} at time t , is governed by the conservation equation,

$$\frac{\partial \Omega}{\partial t} + \nabla_{\mathbf{x}} \cdot (U_s \mathbf{p} \Omega) + \frac{1}{\tau} \left(\Omega - \frac{1}{\Omega_{ist}} \int \Omega d\mathbf{p} \right) = 0 \quad (2.1)$$

where $\Omega_{ist} = 2\pi$ in 2D and $\Omega_{ist} = 4\pi$ in 3D. Here, we have assumed random tumbling with no correlations between pre- and post-tumble orientations, which leads to the simplified tumbling kernel in (2.1). On Fourier transforming (2.1) we get,

$$\frac{\partial \tilde{\Omega}}{\partial t} + 2\pi i \mathbf{k} \cdot \mathbf{p} U_s \tilde{\Omega} + \frac{1}{\tau} \left(\tilde{\Omega} - \frac{1}{\Omega_{ist}} \int \tilde{\Omega} d\mathbf{p} \right) = 0, \quad (2.2)$$

where the Fourier transformed probability density, the characteristic function, is defined as [Lighthill, 1958],

$$\tilde{\Omega}(\mathbf{k}, \mathbf{p}, t) = \int \Omega(\mathbf{x}, \mathbf{p}, t) e^{-2\pi i \mathbf{k} \cdot \mathbf{x}} d\mathbf{x}. \quad (2.3)$$

We look for eigenfunctions of the Fourier transformed run-and-tumble operator, \mathcal{L} in (2.2), by substituting a normal-form with an exponential time dependence, $\tilde{\Omega} = \hat{\Omega}(\mathbf{x}, \mathbf{p}) e^{\sigma t}$, to get,

$$\left(\sigma + 2\pi i \mathbf{k} \cdot \mathbf{p} U_s + \frac{1}{\tau}\right) \hat{\Omega} = \frac{1}{\Omega_{ist} \tau} \int \hat{\Omega} d\mathbf{p}, \quad (2.4)$$

where σ denotes the eigenvalue. To derive the eigenfunction, $\hat{\Omega}$, one needs to solve the integral equation, (2.4). We outline the solution of (2.4) in both two and three dimensions. To solve (2.4), we choose a wavevector-aligned co-ordinate system. In 2D, use of a plane polar coordinate system gives,

$$\left(\sigma + 2\pi i k \cos \theta U_s + \frac{1}{\tau}\right) \hat{\Omega} = \frac{1}{2\pi\tau} \int \hat{\Omega} d\theta, \quad (2.5)$$

where we have used $\mathbf{k} \cdot \mathbf{p} = k \cos \theta$ and $\theta \in (-\pi, \pi)$. In 3D, use of a spherical polar coordinate system gives

$$\left(\sigma + 2\pi i k \cos \theta U_s + \frac{1}{\tau}\right) \hat{\Omega} = \frac{1}{4\pi\tau} \int \hat{\Omega} \sin \theta d\theta d\phi, \quad (2.6)$$

where θ is the polar angle ($\theta \in (0, \pi)$) and ϕ is the azimuthal angle measured in the $\mathbf{I} - \hat{\mathbf{k}}\hat{\mathbf{k}}$ plane ($\hat{\mathbf{k}}$ being the unit vector along \mathbf{k}).

Now, without loss of generality, one may express $\hat{\Omega}$ as the sum of odd and even parts about $\theta = 0$ (with $\theta \in (-\pi, \pi)$) in 2D, $\hat{\Omega} = \hat{\Omega}^o + \hat{\Omega}^e$; and as a sum of axisymmetric and non-axisymmetric modes in 3D, $\hat{\Omega} = \hat{\Omega}^0 + \sum_{m=1}^{\infty} \hat{\Omega}^m(k, \theta) \cos(m\phi)$. Only the even (axisymmetric) modes carry concentration perturbations and hence for the odd (non-axisymmetric) eigenfunctions in 2D (3D), the integral kernel in (2.5) (or 2.6) vanishes. This gives in 2D, for the odd mode,

$$\left(\sigma + 2\pi i k U_s \cos \theta + \frac{1}{\tau}\right) \hat{\Omega}^o = 0, \quad (2.7)$$

and, for the even mode,

$$\left(\sigma + 2\pi i k U_s \cos \theta + \frac{1}{\tau}\right) \hat{\Omega}^e = \frac{1}{2\pi\tau} \int_{-\pi}^{\pi} \hat{\Omega}^e d\theta. \quad (2.8)$$

In 3D, for the non-axisymmetric modes (for $m \neq 0$)

$$\left(\sigma + 2\pi i k U_s \mu + \frac{1}{\tau}\right) \hat{\Omega}^m = 0, \quad (2.9)$$

and, for the axisymmetric mode,

$$(\sigma + 2\pi ikU_s\mu + \frac{1}{\tau})\hat{\Omega}^0 = \frac{1}{2\tau} \int_{-1}^1 \hat{\Omega}^0 d\mu, \quad (2.10)$$

where we have used $\cos \theta = \mu$, and the integration over ϕ has been carried out.

2.2.2 Eigenspectrum of the Run and Tumble Operator \mathcal{L}

Continuous Spectrum

In 2D, $\sigma = -1/\tau - 2\pi iU_s k \cos \theta_0$ for $\theta_0 \in [-\pi, \pi]$ forms a continuous set of eigenvalues for \mathcal{L} . The associated odd eigenfunctions (Φ_{cs}^o) then satisfy the equation,

$$(\cos \theta - \cos \theta_0)\Phi_{cs}^o = 0, \quad (2.11)$$

which is solved by,

$$\Phi_{cs}^o(\theta; \theta_0) = \delta(\theta - \theta_0) - \delta(\theta + \theta_0), \quad (2.12)$$

where the particular superposition of delta functions satisfies the constraint of being odd in θ . The even eigenfunctions (Φ_{cs}^e) satisfy,

$$2\pi ikU_s(\cos \theta - \cos \theta_0)\Phi_{cs}^e = \frac{1}{2\pi\tau} \int \Phi_{cs}^e d\theta. \quad (2.13)$$

To solve (2.13), we assume $\Phi_{cs}^e = \delta(\theta - \theta_0) + \delta(\theta + \theta_0) + c \frac{1}{\cos \theta - \cos \theta_0}$, where both the delta function superposition and the third term satisfy the constraint of being even in θ . On substituting and simplifying we obtain,

$$\Phi_{cs}^e(\theta; \theta_0) = \delta(\theta - \theta_0) + \delta(\theta + \theta_0) + \frac{1}{2\pi^2 ikU_s \tau} \mathcal{P} \frac{1}{\cos \theta - \cos \theta_0}, \quad (2.14)$$

where \mathcal{P} denotes a Principal-Value (PV) interpretation of the singularity [[Balmforth and Morrison, 1995b](#); [Case, 1959](#); [Gakhov, 2014](#); [Roy and Subramanian, 2014a](#)].

The eigenfunction and eigenvalue expressions are derived similarly in 3D. In this case, $\sigma = -1/\tau - 2\pi iU_s k \mu_0$ with $\mu_0 \in [-1, 1]$ gives the continuous set of eigenvalues; the non-axisymmetric eigenfunctions satisfying (2.9) are

$$\Phi_{cs}^m(\mu; \mu_0) = \delta(\mu - \mu_0), \quad (2.15)$$

and the axisymmetric eigenfunctions, satisfying (2.10), are

$$\Phi_{cs}^0(\mu; \mu_0) = \left[1 - \frac{1}{4\pi ik U_s \tau} \int_{-1}^1 \frac{1}{\mu' - \mu_0} d\mu' \right] \delta(\mu - \mu_0) + \frac{1}{4\pi ik U_s \tau} \mathcal{P} \frac{1}{\mu - \mu_0}, \quad (2.16)$$

where the second term may be derived in a manner similar to the 2D case above and again has a PV-interpretation.

The continuous spectrum eigenfunctions are thus generalized functions [Lighthill, 1958]. Since the odd (non-axisymmetric) modes have no associated concentration inhomogeneity, they correspond to spatially homogeneous modes that propagate with a phase speed that is swimming velocity projected along the wave vector. The orientation space structure corresponds to swimmers aligned along and against a particular direction in 2D; and to swimmers on the surface of a cone in 3D. The PV term in the even (axisymmetric) eigenfunction, on the other hand, denotes the contribution of the inverse tumbles (the integral terms in (2.13) and (2.16)), and leads to a non-trivial orientation space structure. These continuous spectrum eigenmodes decay due to tumbling at the rate τ^{-1} , and are convected due to swimming with a continuum of phase speeds in the interval $[-2\pi U_s k, 2\pi U_s k]$ which constitute the imaginary part of the eigenvalues. In over-damped systems, complex eigenvalues signify the lack of microscopic time-reversibility [Kurchan, 2009]. Thus, in the convective part of the eigenvalues we see the manifestation of the swimming-induced breakdown in time reversibility for run-and-tumble particles [Cates, 2012].

While analysing Landau damping in plasmas, Van Kampen [1955] was the first one to suggest the possibility of singular eigenfunctions associated with a continuous spectrum. Such a continuous spectrum usually arises in physical situations without dissipative relaxations; examples include plasma oscillations where the singularity occurs in the probability distribution in velocity space [Case, 1978, 1959; Sedlacek, 1971; Van Kampen, 1955], inviscid shear-flows where the singularity occurs in the vorticity field [Balmforth and Morrison, 1995a,b; Roy and Subramanian, 2014a,b] and the Kuramoto model of coupled oscillators where one again has the orientation field [Strogatz and Mirollo, 1991; Strogatz et al., 1992]. We see here that RTPs, on the other hand, have singular eigenfunctions in orientation space even in the presence of relaxation. This is because tumbling, in corresponding to a non-local relaxation of orientation, does not penalize rapid angular variations of the orientation probability and thus allowing for singular eigenfunctions.

Regular Discrete Mode

In addition to the singular eigenfunctions discussed above, one may also look for regular eigenfunctions of \mathcal{L} i.e. the discrete modes. Such regular eigenfunctions only exist for the even (axisymmetric) modes in 2D (3D). In 2D, we assume the following ansatz for the discrete eigenvalue, $\sigma_d = -1/\tau - 2\pi i U_s k \cos \theta_d$. The associated eigenfunction is then seen to be

$$\Phi_d^e(\theta; \theta_d) = \frac{1}{\cos \theta - \cos \theta_d}, \quad (2.17)$$

which lacks the Dirac delta function term seen earlier. On substituting (2.17) in the governing equation (2.13), one can derive the relation for the discrete eigenvalue. After simplification, we obtain the dispersion relation, in 2D, as

$$4\pi^2 ik U_s \tau = \int_{-\pi}^{\pi} \frac{1}{\cos \theta - \cos \theta_d} d\theta, \quad (2.18)$$

which leads to,

$$\cos \theta_d = - \left(1 - \frac{1}{(2\pi k U_s \tau)^2} \right)^{1/2}, \quad (2.19)$$

and finally,

$$\theta_d = \arccos \left(- \left(1 - \frac{1}{(2\pi k U_s \tau)^2} \right)^{1/2} \right), \quad (2.20)$$

for $2\pi k U_s \tau \leq 1$. Similarly, in 3D, the discrete eigenvalue $\sigma_d = -1/\tau - 2\pi i U_s k \mu_d$ is associated with the eigenfunction,

$$\Phi_d^0(\mu; \mu_d) = \frac{1}{\mu - \mu_d}. \quad (2.21)$$

This leads to the dispersion relation,

$$4\pi ik U_s \tau = \int_{-1}^1 \frac{1}{\mu - \mu_d} d\mu. \quad (2.22)$$

with the solution

$$\mu_d = i \cot(2\pi k U_s \tau). \quad (2.23)$$

Based on θ_d as given in (2.20), and μ_d in (2.23), the discrete eigenvalue is purely real, and therefore non-oscillatory, signifying a monotonic decay of concentration fluctuations; these fluctuations are obtained from integrating the discrete mode over orientation space. The discrete mode exists only for a finite range of wavenumbers given by $k \in (0, 1/(2\pi U_s \tau))$ in 2D and $k \in (0, 1/(4U_s \tau))$ in 3D. For long times ($t \gg \tau$), RTPs behave as passive Brownian

particles with an effective translational diffusivity and this long-time behavior is dominated by the long-wavelength modes ($k \rightarrow 0$) [Bechinger et al., 2016; Tailleur and Cates, 2008]. By taking the long-wavelength limit of the discrete modes, we recover the diffusive behavior with the discrete eigenvalue representing a diffusive relaxation with an effective diffusivity given by $U_s^2/2\tau$ in 2D and $U_s^2/3\tau$ in 3D. At the other extreme, the discrete mode falls into the continuous spectrum for $k \rightarrow 1/(2\pi U_s \tau)$ ($k \rightarrow 1/(4U_s \tau)$) in 2D (3D), with the discrete mode eigenvalue approaching $\theta_d \rightarrow 0$ in 2D (and $\mu_d \rightarrow 0$ in 3D) which in turn implies $\sigma_d \rightarrow -1/\tau$ in both instances. In contrast, the continuous spectrum modes in contrast have a finite decay rate for $k \rightarrow 0$, and hence, do not contribute to the long-time behavior.

Singular Discrete Modes

The 2D dispersion relation in (2.18) has additional solutions given by

$$\cos \theta_I = \pm \left(1 - \frac{1}{(2\pi k U_s \tau)^2} \right)^{1/2}, \quad (2.24)$$

for any $k > 1/(2\pi U_s \tau)$. Since $\cos \theta_I \in [-1, 1]$, the eigenfunction given by (2.17) has a singularity. The singular eigenfunction associated with $\cos \theta_I$ may be derived by taking the limit of $\cos \theta_d$ approaching the real axis in (2.17),

$$\Phi_I^e(\theta; \theta_I) = \lim_{\varepsilon \rightarrow 0} \frac{1}{\cos \theta - \cos \theta_d + i\varepsilon}, \quad (2.25)$$

which gives, upon using the Sokhotski-Plemelj formula,

$$\Phi_I^e(\theta; \theta_I) = \delta(\theta - \theta_I) + \delta(\theta + \theta_I) + \frac{1}{2\pi^2 i k U_s \tau} \mathcal{P} \frac{1}{\cos \theta - \cos \theta_I}, \quad (2.26)$$

which is the same as the continuous spectrum eigenfunction for $\theta_0 = \theta_I$. The need to single out θ_I from the continuous spectrum arises when deriving the adjoint (see the discussion in section 2.2.3).

Thus, once the discrete mode falls into the continuous spectrum ($k = 1/(2\pi U_s \tau)$) in 2D, it morphs into a pair of singular discrete modes for $k > 1/(2\pi U_s \tau)$. Such singular discrete modes were first discussed by Case [1978] in the context of plasmas, and have also been found in inviscid shear flows [Balmforth and Morrison, 1995b]. In contrast, in 3D, as the discrete mode eigenvalue approaches the continuous spectrum, the eigenfunction does not become singular, and there is no need to define a separate singular discrete mode. To summarise, in 2D, on approaching the continuous spectrum the discrete eigenfunction

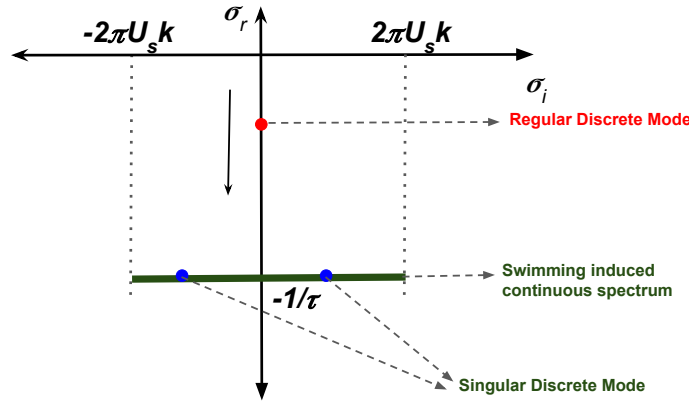


Fig. 2.1 Schematic showing the eigenvalue spectrum of the run-and-tumble operator, \mathcal{L} . As discussed in the text, the regular discrete mode only exists for a finite range of k and the singular discrete modes only exist in 2D.

approaches a limiting singular form, in contrast in 3D the discrete eigenfunction stays regular as it crosses the CS. One thus expects the discrete mode in 3D to cross the continuous spectrum, and move onto a distinct Riemann sheet, and behave as a quasi-mode thereafter; the latter is known as the underlying reason for the phenomenon of Landau damping in plasmas [Balmforth et al., 2013; Case, 1959; Roy and Subramanian, 2014b; Strogatz et al., 1992; Van Kampen, 1955].

Summary of the Eigenspectrum

The eigenspectrum of the run-and-tumble operator, \mathcal{L} , is summarized in figure 2.1. The fastest decaying eigenvalues correspond to the continuous spectrum modes and have a real part that equals the inverse of the mean tumble time (τ); no relaxation can occur on a smaller time-scale. Further, all the continuous spectrum modes relax at the same rate independent of the wavevector. The regular discrete mode shows wavevector-dependent relaxation, reducing to a diffusive mode in the long-wavelength limit. The continuous spectrum modes include both odd and even (axisymmetric and non-axisymmetric) orientation modes, while the discrete modes only include even (axisymmetric) orientation modes.

This should be contrasted with the known eigenspectrum for active Brownian particles (ABPs), where orientation relaxation occurs due to rotary diffusion. Such a local orientation relaxation mechanism does not allow for the singular eigenfunctions associated with the continuous-spectrum, and the eigenspectrum consists instead of an infinite number of discrete modes [Kurzthaler et al., 2018; Kurzthaler and Franosch, 2017; Kurzthaler et al., 2016].

2.2.3 Adjoint Eigenfunctions of \mathcal{L}

The adjoint eigenfunctions are also needed to construct the Green's function analytically, and in this section we outline the expressions for the adjoints associated with each of the eigenfunctions discussed in the previous section.

Continuous Spectrum

Adjoint for the continuous spectrum eigenfunctions may be derived by solving a singular integral equation [Balmforth and Morrison, 1995b; Case, 1959, 1960; Roy and Subramanian, 2014a]. This rather involved calculation is detailed at the end of the chapter in section 2.5, and here we just give the expressions for adjoints to the various eigenfunctions. In 2D, for the odd eigenfunctions, the adjoint, corresponding to the eigenvalue θ_0 with $\theta_0 \in [-\pi, \pi]$, is given by,

$$\tilde{\Phi}_{cs}^o(\theta_0; \theta') = \delta(\theta' - \theta_0) - \delta(\theta' + \theta_0), \quad (2.27)$$

while the even adjoint eigenfunction, corresponding to the eigenvalue θ_0 , is given by,

$$\tilde{\Phi}_{cs}^e(\theta_0; \theta') = \frac{1}{D(\theta_0)} \left(\delta(\theta' - \theta_0) + \delta(\theta' + \theta_0) + \frac{1}{2\pi^2 ik U_s \tau} \mathcal{P} \frac{1}{\cos \theta' - \cos \theta_0} \right), \quad (2.28)$$

where

$$D(\theta_0) = 1 - \frac{1}{(2\pi k U_s \tau \sin \theta_0)^2}. \quad (2.29)$$

$D(\theta_0)$ is known as the dielectric function in the plasma literature [Nicholson, 1983]. Similarly, in 3D, the non-axisymmetric adjoint eigenfunction, corresponding to the eigenvalue μ_0 , is given by,

$$\tilde{\Phi}_{cs}^m(\mu_0; \mu') = \delta(\mu' - \mu_0), \quad (2.30)$$

while the axisymmetric adjoint eigenfunction, corresponding to the eigenvalue μ_0 , is given by,

$$\tilde{\Phi}_{cs}^0(\mu_0; \mu') = \frac{1}{D(\mu_0)} \left(\left[1 - \frac{1}{4\pi ik U_s \tau} \int_{-1}^1 \frac{1}{\mu'' - \mu_0} d\mu'' \right] \delta(\mu' - \mu_0) + \frac{1}{4\pi ik U_s \tau} \mathcal{P} \frac{1}{\mu' - \mu_0} \right), \quad (2.31)$$

with the dielectric function,

$$D(\mu) = 1 - \frac{1}{2\pi ik U_s \tau} \int_{-1}^1 \frac{1}{\mu' - \mu} d\mu' - \left(\frac{1}{4k U_s \tau} \right)^2 \left[1 + \left(\frac{1}{\pi} \int_{-1}^1 \frac{1}{\mu' - \mu} d\mu' \right)^2 \right]. \quad (2.32)$$

Regular Discrete Mode

The adjoint for the discrete mode may be derived by imposing the orthonormality constraint $\int_{-\pi}^{\pi} \Phi_d^e \tilde{\Phi}_d^e d\theta = 1$. This gives, in 2D,

$$\tilde{\Phi}_d^e(\theta_d; \theta') = \frac{1}{\cos \theta' - \cos \theta_d} \frac{1}{\int_{-\pi}^{\pi} (\cos \theta - \cos \theta_d)^{-2} d\theta}. \quad (2.33)$$

Similarly in 3D, we get the adjoint for the discrete mode as

$$\tilde{\Phi}_d^0(\mu_d; \mu') = \frac{1}{\mu' - \mu_d} \frac{1}{\int_{-1}^1 (\mu - \mu_d)^{-2} d\mu}. \quad (2.34)$$

Singular Discrete Mode

In 2D, the adjoint, given by (2.28), has singularities at $\theta_I = \pm \arcsin\left(\frac{1}{2\pi k U_s \tau}\right)$ for $2\pi k U_s \tau > 1$, corresponding to the singular discrete modes discussed earlier. To compute the corresponding adjoint, we displace θ_0 in (2.28) from the real axis and then take the appropriate limit, as follows,

$$\tilde{\Phi}^e(\theta_0; \theta') = \lim_{\varepsilon \rightarrow 0} \frac{1}{1 - \frac{1}{(2\pi k U_s \tau \sin \theta_0)^2} + i\varepsilon} \left(\delta(\theta' - \theta_0) + \delta(\theta' + \theta_0) + \frac{1}{2\pi^2 i k U_s \tau} \mathcal{P} \frac{1}{\cos \theta' - \cos \theta_0} \right), \quad (2.35)$$

to give,

$$\begin{aligned} \tilde{\Phi}^e(\theta_0; \theta') = & \mathcal{P} \frac{1}{1 - \frac{1}{(2\pi k U_s \tau \sin \theta_0)^2}} \left(\delta(\theta' - \theta_0) + \delta(\theta' + \theta_0) + \frac{1}{2\pi^2 i k U_s \tau} \mathcal{P} \frac{1}{\cos \theta' - \cos \theta_0} \right) \\ & + \sum_{\theta_I} \frac{i\pi}{2} \delta(\theta_0 - \theta_I) \frac{\sin \theta_I}{\cos \theta_I} \left(\delta(\theta' - \theta_0) + \delta(\theta' + \theta_0) + \frac{1}{2\pi^2 i k U_s \tau} \mathcal{P} \frac{1}{\cos \theta' - \cos \theta_0} \right) \end{aligned} \quad (2.36)$$

where the summation in the second term is over the two solutions for θ_I . The first term in (2.36) is the adjoint for the continuous spectrum modes given as,

$$\tilde{\Phi}_{cs}^e(\theta_0; \theta') = \mathcal{P} \frac{1}{1 - \frac{1}{(2\pi k U_s \tau \sin \theta_0)^2}} \left(\delta(\theta' - \theta_0) + \delta(\theta' + \theta_0) + \frac{1}{2\pi^2 i k U_s \tau} \mathcal{P} \frac{1}{\cos \theta' - \cos \theta_0} \right), \quad (2.37)$$

and the second term gives the adjoint for the singular discrete modes with,

$$\tilde{\Phi}_I^e(\theta_I; \theta') = \sum_{\theta_I} \frac{i\pi}{2} \delta(\theta_0 - \theta_I) \frac{\sin \theta_I}{\cos \theta_I} \left(\delta(\theta' - \theta_0) + \delta(\theta' + \theta_0) + \frac{1}{2\pi^2 ik U_s \tau} \mathcal{P} \frac{1}{\cos \theta' - \cos \theta_0} \right), \quad (2.38)$$

where $\theta_I = \pm \arcsin\left(\frac{1}{2\pi k U_s \tau}\right)$ for $2\pi k U_s \tau > 1$.

2.2.4 Greens Function of \mathcal{L}

For a general operator in Hilbert space, the complete set of eigenfunctions and their adjoints may be used to construct the Green's function [Friedman, 1990; Ramkrishna and Amundson, 1985],

$$G(\lambda, t | \lambda', 0) = \int \Phi_{cs}(\lambda; \lambda_0) \tilde{\Phi}_{cs}(\lambda_0; \lambda') e^{\lambda_0 t} d\lambda_0 + \sum_n \Phi_d(\lambda; \lambda_n) \tilde{\Phi}_d(\lambda_n; \lambda') e^{\lambda_n t}, \quad (2.39)$$

where the first and second term represent the continuous and discrete spectrum contributions, respectively and λ represents the relevant variable while λ' the associated initial condition. For (2.39) to be valid, the eigenfunctions and their adjoints must follow orthogonality relations which are proved in section 2.5.3 at the end of this chapter.

Using (2.39), we obtain the exact Green's function for the Fourier transformed run-and-tumble operator (2.2) in 2D as,

$$\begin{aligned} G_k(\theta, t | \theta', 0) &= \int_{-\pi}^{\pi} \Phi_{cs}^e(\theta; \theta_0) \tilde{\Phi}_{cs}^e(\theta_0; \theta') e^{-2\pi i k \cos \theta_0 U_s t - \frac{t}{\tau}} d\theta_0 \\ &+ \mathcal{H} \left(\frac{1}{2\pi U_s \tau} - k \right) \Phi_d^e(\theta; \theta_d) \tilde{\Phi}_d^e(\theta_d; \theta') e^{-2\pi i k \cos \theta_d U_s t - \frac{t}{\tau}} \\ &+ \mathcal{H} \left(k - \frac{1}{2\pi U_s \tau} \right) \sum_{\pm \arcsin\left(\frac{1}{2\pi k U_s \tau}\right)} \Phi_I^e(\theta; \theta_I) \tilde{\Phi}_I^e(\theta_I; \theta') e^{-2\pi i k \cos \theta_I U_s t - \frac{t}{\tau}} \\ &+ (\delta(\theta - \theta') - \delta(\theta + \theta')) e^{-2\pi i k \cos \theta U_s t - \frac{t}{\tau}}, \end{aligned} \quad (2.40)$$

and in 3D as,

$$\begin{aligned}
G_k(\mu, \phi, t | \mu', \phi', 0) &= \frac{1}{2\pi} \int_{-1}^1 \Phi_{cs}^0(\mu; \mu_0) \tilde{\Phi}_{cs}^0(\mu_0; \mu') e^{-2\pi i k \mu_0 U_s t - \frac{t}{\tau}} d\mu_0 \\
&+ \frac{1}{2\pi} \mathcal{H} \left(\frac{1}{4U_s \tau} - k \right) \Phi_d^0(\mu; \mu_d) \tilde{\Phi}_d^0(\mu_d; \mu') e^{-2\pi i k \mu_d U_s t - \frac{t}{\tau}} \\
&+ \sum_{m=1}^{\infty} \delta(\mu - \mu') \cos(m(\phi - \phi')) e^{-2\pi i k \mu U_s t - \frac{t}{\tau}}, \tag{2.41}
\end{aligned}$$

where \mathcal{H} denotes the Heaviside-function. In (2.40) and (2.41), the eigenvalue integral over the odd and non-axisymmetric contributions is trivial, and has therefore been carried out, leading to a particularly simple expression for the corresponding Green's function contribution. The integrated result displays non-separable dependence on orientation and time, as is expected for the continuous spectrum.

Completeness

At $t = 0$, the Green's function must equal the relevant orientation space Dirac delta function by definition. Hence (2.40) and (2.41) reduce to the following completeness identities at $t = 0$,

$$\begin{aligned}
2\delta(\theta - \theta') &= \int_{-\pi}^{\pi} \Phi_{cs}^e(\theta; \theta_0) \tilde{\Phi}_{cs}^e(\theta_0; \theta') d\theta_0 + \mathcal{H} \left(\frac{1}{2\pi U_s \tau} - k \right) \Phi_d^e(\theta; \theta_d) \tilde{\Phi}_d^e(\theta_d; \theta') \\
&+ \mathcal{H} \left(k - \frac{1}{2\pi U_s \tau} \right) \sum_{\pm \arcsin\left(\frac{1}{2\pi k U_s \tau}\right)} \Phi_I^e(\theta; \theta_I) \tilde{\Phi}_I^e(\theta_I; \theta') + (\delta(\theta - \theta') - \delta(\theta + \theta')), \tag{2.42}
\end{aligned}$$

and

$$\begin{aligned}
\delta(\mu - \mu') \delta(\phi - \phi') &= \frac{1}{2\pi} \int_{-1}^1 \Phi_{cs}^0(\mu; \mu_0) \tilde{\Phi}_{cs}^0(\mu_0; \mu') d\mu_0 \\
&+ \frac{1}{2\pi} \mathcal{H} \left(\frac{1}{4U_s \tau} - k \right) \Phi_d^0(\mu; \mu_d) \tilde{\Phi}_d^0(\mu_d; \mu') + \sum_{m=1}^{\infty} \delta(\mu - \mu') \cos(m(\phi - \phi')). \tag{2.43}
\end{aligned}$$

The method of finding the adjoint ensures that these identities hold (see section 2.5.1 and 2.5.2). We have also verified (2.42) and (2.43) by numerical evaluation after integrating over the initial condition. We have, thus, found the complete set of eigenfunctions of the run-and-tumble operator. Hence, the Green's function expression can be used to construct the

solution for an arbitrary initial condition in both orientation-position space [Friedman, 1990; Ramkrishna and Amundson, 1985]. For an arbitrary initial condition $B(\theta')$, in the 2D case, the time evolution of the probability density in terms of the Green's function is thus given by,

$$\begin{aligned}\tilde{\Omega}(k, \theta, t) &= \int_{-\pi}^{\pi} G_k(\theta, t | \theta', 0) (B(\theta')) d\theta' \\ &= (B(\theta) - B(-\theta)) e^{-2\pi i k \cos \theta U_s t - \frac{t}{\tau}}.\end{aligned}\quad (2.44)$$

To proceed further, we separate the initial condition into subsets with net-zero and finite concentrations.

Initial Conditions with net-zero concentration of RTPs

An initial condition with net zero concentration of RTPs that is $\tilde{\Omega}(k, \theta, t)$ satisfying $\int_{-\pi}^{\pi} d\theta \tilde{\Omega}(k, \theta, t) = 0$ would project only onto the odd (non-axisymmetric) part of the Green's function. For an arbitrary function, $B(\theta')$ in the 2D case, this initial condition may be written in the form $B(\theta') - B(-\theta')$ and the resulting evolution in time is simply given by,

$$\begin{aligned}\tilde{\Omega}(k, \theta, t) &= \int_{-\pi}^{\pi} G_k(\theta, t | \theta', 0) (B(\theta') - B(-\theta')) d\theta' \\ &= (B(\theta) - B(-\theta)) e^{-2\pi i k \cos \theta U_s t - \frac{t}{\tau}},\end{aligned}\quad (2.45)$$

where the even terms in the Green's function integrate to zero. Similarly for a non-axisymmetric initial condition, $\sum_{m=1}^{\infty} B(\mu') \cos(m\phi')$ in 3D, the axisymmetric terms in the Green's function integrate to zero and we get,

$$\begin{aligned}\tilde{\Omega}(k, \mu, \phi, t) &= \int_{-1}^1 G_k(\mu, \phi, t | \mu', \phi', 0) \sum_{m=1}^{\infty} B(\mu') \cos(m\phi') d\mu' \phi' \\ &= \sum_{m=1}^{\infty} B(\mu) \cos(m\phi) e^{-2\pi i k \mu U_s t - \frac{t}{\tau}},\end{aligned}\quad (2.46)$$

Thus, we see that such initial conditions, representing pure orientation dynamics, have a simple time evolution, being convected in space due to swimming, as the amplitude decays exponentially due to tumbling. These initial conditions are important when considering fluid velocity correlations in a bacterial suspension [Belan and Kardar, 2019; Nambiar et al., 2021].

Initial Conditions with a finite concentration of RTPs

Initial conditions corresponding to a non-zero concentration of RTPs project onto the even (axisymmetric) parts of the Green's function and develop a non-trivial spatial structure as they evolve in time. For an isotropic initial condition, we obtain for the joint-probability density in 2D,

$$\begin{aligned}\tilde{\Omega}(k, \theta, t) &= \frac{1}{2\pi} \int_{-\pi}^{\pi} G_k(\theta, t | \theta', 0) d\theta' = \frac{1}{2\pi} \int_{-\pi}^{\pi} \frac{\Phi_{cs}^e(\theta; \theta_0)}{D(\theta_0)} e^{-2\pi i k \cos \theta_0 U_s t - \frac{t}{\tau}} d\theta_0 \\ &+ \frac{1}{2\pi} \Phi_d^e(\theta; \theta_d) \frac{4\pi^2 i k U_s \tau}{\int_{-\pi}^{\pi} (\cos \theta - \cos \theta_d)^{-2} d\theta} e^{-2\pi i k \cos \theta_d U_s t - \frac{t}{\tau}} \\ &+ \frac{1}{2\pi} \sum_{\pm \arcsin\left(\frac{1}{2\pi k U_s \tau}\right)} \Phi_I^e(\theta; \theta_I) \frac{i\pi \sin \theta_I}{2 \cos \theta_I} e^{-2\pi i k \cos \theta_I U_s t - \frac{t}{\tau}}\end{aligned}\quad (2.47)$$

and similarly in 3D,

$$\begin{aligned}\tilde{\Omega}(k, \mu, t) &= \frac{1}{4\pi} \int G_k(\mu, \phi, t | \mu', \phi', 0) d\mu' d\phi' \\ &= \frac{1}{4\pi} \int_{-1}^1 \frac{\Phi_{cs}^0(\mu; \mu_0)}{D(\mu_0)} e^{-2\pi i k \mu_0 U_s t - \frac{t}{\tau}} d\mu_0 \\ &+ \frac{1}{4\pi} \mathcal{H} \left(\frac{1}{4U_s \tau} - k \right) \Phi_d^0(\mu; \mu_d) \frac{4\pi i k U_s \tau}{\int_{-1}^1 (\mu - \mu_d)^{-2} d\mu} e^{-2\pi i k \mu_d U_s t - \frac{t}{\tau}}.\end{aligned}\quad (2.48)$$

To derive (2.47) and (2.48), we have used the normalization expressions derived in section 2.5.3. (2.47) and (2.48) are used to further study the probability density in section 2.3.

Approaching the straight swimmer limit

We illustrate how the general solution approaches the straight swimmer limit ($\tau \rightarrow \infty$) in 2D. Recall that the regular discrete mode only exists for a limited range where $k \in (0, 1/(2\pi U_s \tau))$. For $\tau \rightarrow \infty$, the discrete mode contribution thus vanishes and only the continuous spectrum remains, where the CS eigenfunctions simplify as follows, with $\tau \rightarrow \infty$,

$$\Phi_{cs}^e(\theta; \theta_0) = \delta(\theta - \theta_0) + \delta(\theta + \theta_0) \quad (2.49)$$

where the additional singular term has dropped out. The odd CS eigenfunctions remain unchanged. The same simplification happens for the adjoint eigenfunctions, and as a result

the final limit of the Green's function can be seen to be,

$$G_k(\theta, t | \theta', 0) = \delta(\theta - \theta') e^{-2\pi i k \cos \theta U_s t}, \quad (2.50)$$

which physically represents the initial probability density being convected unchanged a swimming along a straight trajectory corresponding to the initial orientation. Similarly in 3D, we get

$$G_k(\mu, t | \mu', 0) = \delta(\mu - \mu') e^{-2\pi i k \mu U_s t}. \quad (2.51)$$

2.3 Results

In the rest of the chapter, we present results for the evolution of run-and-tumble particles calculated for an isotropic initial condition in orientation space and delta function initial condition in position space at an arbitrary point which, without loss of generality, is taken to be the origin. All length and time scales can naturally be non-dimensionalized by the run length, $U_s \tau$, and the relaxation time, τ , respectively. The swim speed thus becomes unity in non-dimensional units. All the results in this section are presented in terms of the aforementioned non-dimensional variables.

2.3.1 Intermediate Scattering Function

We first examine the time evolution of the intermediate scattering function (ISF) for RTPs, which in general is defined as,

$$\tilde{\Omega}(\mathbf{k}, t) = \int d\mathbf{p} \tilde{\Omega}(\mathbf{k}, \mathbf{p}, t). \quad (2.52)$$

Integrating (2.47) over the orientation degrees of freedom, and using the fact that the ISF must be isotropic, gives an expression for the intermediate scattering function (ISF), in 2D as

$$\begin{aligned} \tilde{\Omega}(k, t) &= \int_{-\pi}^{\pi} \frac{1}{D(\theta_0)} e^{-2\pi i k \cos \theta_0 t - t} d\theta_0 \\ &+ \mathcal{H} \left(\frac{1}{2\pi} - k \right) \frac{(4\pi^2 i k)^2}{\int_{-\pi}^{\pi} (\cos \theta - \cos \theta_d)^{-2} d\theta} e^{-2\pi i k \cos \theta_d t - t} \\ &+ \mathcal{H} \left(k - \frac{1}{2\pi} \right) \sum_{\pm \arcsin \left(\frac{1}{2\pi k U_s \tau} \right)} \frac{i\pi \sin \theta_I}{2 \cos \theta_I} e^{-2\pi i k \cos \theta_I t - t} \end{aligned} \quad (2.53)$$

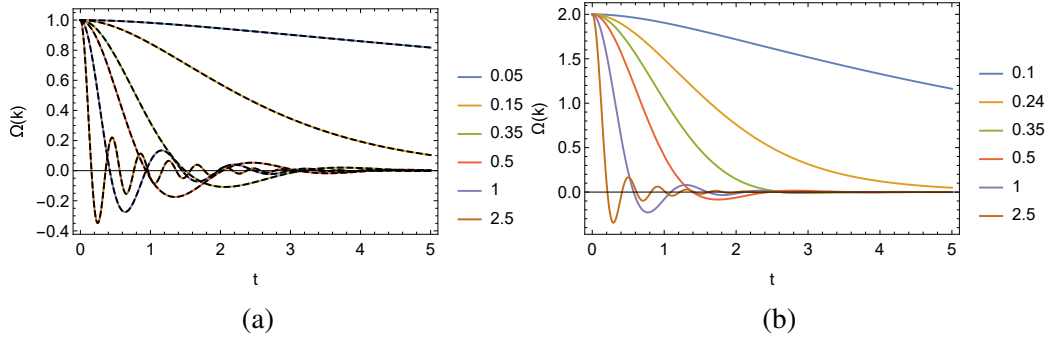


Fig. 2.2 The time evolution of the intermediate scattering function for various wavenumbers (k) in (a) 2D and (b) 3D; the chosen k values are indicated on the RHS of each figure. In (a) the corresponding results from [Martens et al. \[2012\]](#) are plotted as dashed lines, and are in perfect agreement.

and similarly from (2.48) in 3D,

$$\begin{aligned} \tilde{\Omega}(k, t) = & \int_{-1}^1 \frac{1}{D(\mu_0)} e^{-2\pi i k \mu_0 t - t} d\mu_0 \\ & + \mathcal{H}\left(\frac{1}{4} - k\right) \frac{(4\pi i k)^2}{\int_{-1}^1 (\mu - \mu_d)^{-2} d\mu} e^{-2\pi i k \mu_d t - t}, \end{aligned} \quad (2.54)$$

where we have again used the normalization expressions derived at the end of the chapter in section 2.5.3. (2.53) and (2.54) reduce to the ballistic and diffusive forms in the limits $k \rightarrow \infty$ and $k \rightarrow 0$, respectively. First lets consider the ballistic straight swimmer limit, where the ISF is seen to be, in 2D from (2.53),

$$\begin{aligned} \tilde{\Omega}(k, t) &= \int_{-\pi}^{\pi} e^{-2\pi i k \cos \theta_0 t} d\theta_0 \\ &= 2\pi J_0(2\pi k t) \end{aligned} \quad (2.55)$$

where J_0 represents the Bessel function of the first kind. The discrete mode contribution drops off in this limit since the contribution comes from wavenumbers k such that $k > 1/2\pi$. In 3D similarly we get from (2.54),

$$\begin{aligned} \tilde{\Omega}(k, t) &= \int_{-1}^1 e^{-2\pi i k \cos \mu_0 t} d\mu_0 \\ &= \frac{\sin(2\pi k t)}{\pi k t}, \end{aligned} \quad (2.56)$$

where the discrete mode again doesn't contribute. In the diffusive regime, we get the usual solutions for passive Brownian particles, with $e^{-D_{eff}k^2t}$, where $D_{eff} = 1/2$ in 2D and $D_{eff} = 1/3$ in 3D.

Figure 2.2 plots the time evolution of the intermediate scattering function for various wavenumbers numerically evaluated from (2.53) and (2.54). For $k < 1/2\pi$ ($k < 1/4$) in 2D (3D), the ISF shows a monotonic decay, typical of passive systems. This is the range of wavenumbers for which the discrete mode exists as discussed earlier. For larger wavenumbers, the ISF shows an oscillatory decay, with the dynamics controlled by the continuous spectrum modes. The oscillatory decay thus results from the convection due to swimming as discussed earlier in the interpretation of the continuous spectrum modes. Wilson et al. [2011] measured the ISF for motile bacteria using differential dynamic microscopy [Schwarz-Linek et al., 2016]. However, they could access only very small length scales. More recently Kurzthaler et al. [2018] have observed a transition from oscillatory to diffusive behavior of the ISF, for self-propelled Janus particles which are modeled as active Brownian particles (ABPs) [Kurzthaler et al., 2018, 2016].

The ISF for RTPs in 2D was earlier evaluated in closed form by Martens et al. [2012] by using an analogy with the Lorentz gas. Although we have not been able to analytically find a way to convert our integral superposition into their infinite series sum, the numerically evaluated values from both the approaches shows excellent agreement (see figure 2.2a). In 3D, to the best of our knowledge, (2.54) is the only closed form expression for the ISF available in the literature.

2.3.2 Position-space Probability density

The probability density $(\Omega(r), t)$ of finding a swimmer at the radial distance r , with any orientation, is obtained by Fourier inversion of the ISF, $\tilde{\Omega}(k, t)$, given in (2.53) and (2.54). Owing to the isotropy of $\tilde{\Omega}(k, t)$ the angular integrals can be carried out, but the remaining integrals for the Fourier inversion need to be carried out numerically. Since RTPs swim at a finite speed (U_s , which is equal to 1 with the scaling used), at any given time t , no swimmer can be found at a distance $r > t$. Thus, $\Omega(r)$ must have compact support [Cates, 2012] and the Fourier inversion of (2.53) and (2.54) has numerical difficulties. They are overcome by adding a translational diffusivity (D_T), which is expected to regularize $\Omega(r)$. ISF for a finite D_T is easily obtained by multiplying the ISF ($\tilde{\Omega}(k, t)$), in equations (2.53) and (2.54), with $e^{-D_T k^2 t}$. Without translational diffusivity ($D_T = 0$), there must be at least one swimmer at the front, $r = t$, which would not have tumbled since $t = 0$ with the probability of finding such a swimmer decreasing exponentially with time as e^{-t} . Thus, in both 2D and 3D, in addition to the compact support we also expect to find a singular front contribution to $\Omega(r)$, of the form

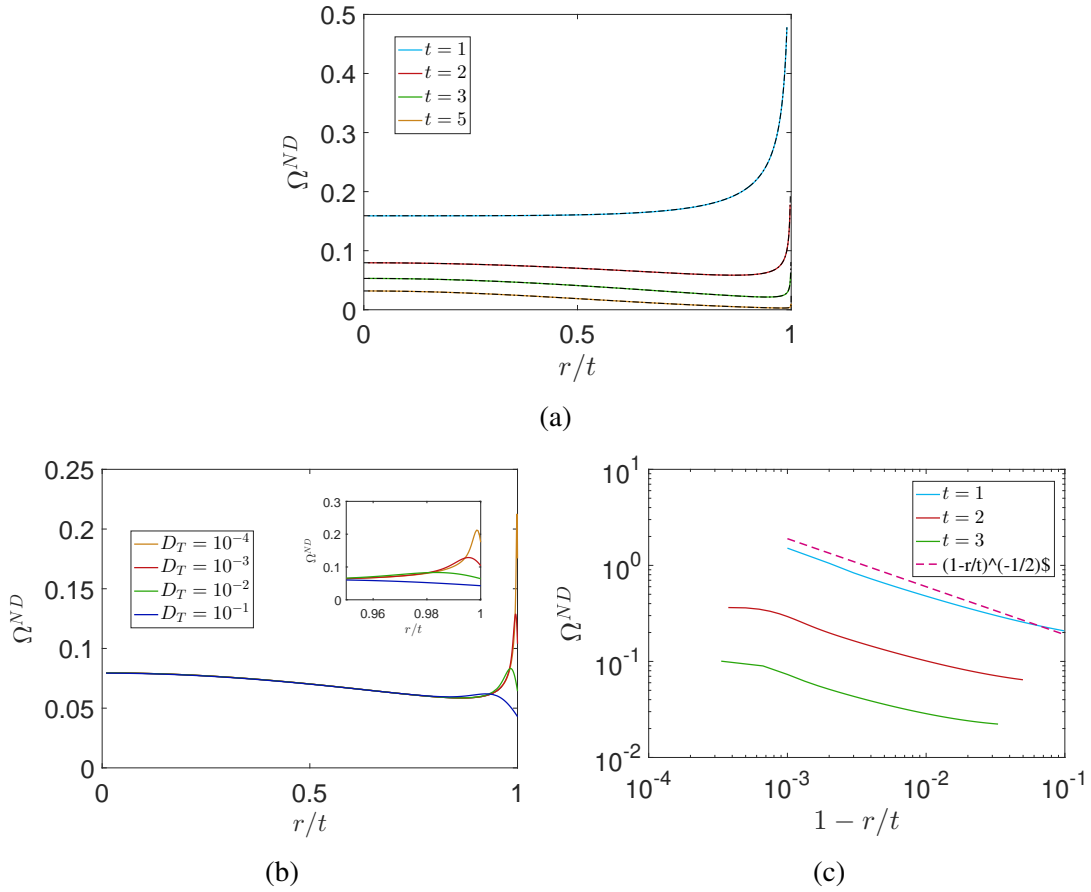


Fig. 2.3 (a) The variation of the regularized probability density, $\Omega^{ND}(r)$, with the scaled radial distance, r/t in 2D for $D_T = 10^{-5}$ at various time t . The expression for $\Omega^{ND}(r)$ from Martens et al. [2012] is plotted as dashed lines and we see an exact match; note that Martens et al. [2012] have $D_T = 0$. (b) The effect of the translational diffusivity (D_T) on the regularized probability density, $\Omega^{ND}(r)$ in 2D at $t = 1$. The inset highlights the effect of D_T at the front. (c) The variation of the regularized probability density, $\Omega^{ND}(r)$, with the scaled radial distance, $1 - r/t$ in 2D for $D_T = 10^{-5}$ at various time t on a log-log plot.

$\delta(r-t)e^{-t}$ for $D_T = 0$. This expression also causes numerical difficulties for small D_T and hence is analytically removed from the exact expression to obtain a regularized probability density that allows for efficient numerical evaluation. We denote this form, with the delta function contribution removed, by $\Omega^{ND}(r)$ in both 2D and 3D. Below, we present results for the regularized probability density, $\Omega^{ND}(r) = \Omega(r) - \delta(r-t)e^{-t}$, in order to clearly focus on the spatial structure behind the front.

Figure 2.3a shows $\Omega^{ND}(r)$ in 2D. The value of D_T chosen is low enough such that the run and tumble motion dominates and we can capture the $D_T \rightarrow 0$ behavior, with the diffusivity only leading to a local regularization in the immediate neighborhood of the front for the times considered. We see that initially the swimmers aggregate at the front and the spatial structure is dominated by the continuous spectrum contribution. At long times, the diffusive, discrete mode dominates and the radial probability density has a maxima at $r = 0$ instead. However, 2.3c shows that $\Omega^{ND}(r)$ diverges as $(t-r)^{-1/2}$ on approaching the front at all times t implying that, for $D_T = 0$, in addition to the front itself being singular, there is an additional algebraic divergence on approach towards this singular front [Martens et al., 2012]. Note that for any finite D_T , Ω^{ND} exhibits the algebraic divergence upon approaching the front, until it is regularized in a certain D_T dependent neighborhood of the front (see 2.3c). Further, at low D_T considered here, beyond the front, such that $r > t$, the probability density is negligibly small compared to the values behind the front and hence it is not shown in the figure. But this is expected since the probability density beyond the front is exactly zero without D_T . The results also show an excellent agreement with the expression derived in Martens et al. [2012], thus validating our approach. Further note that Martens et al. [2012] have $D_T = 0$ exactly and thus the value of D_T here is low enough to capture the run and tumble dynamics. We use this for the rest of the results to choose the corresponding values of D_T . Figure 2.3b shows the effect of the translational diffusivity (D_T). As expected, for small D_T the regularizing effect is confined to the front, where spatial gradients are the largest. Increasing D_T smoothens out the singularity at the front, replacing it with a peak behind the front (figure 2.3b). The probability density in the bulk on the other hand stays unaffected by D_T . For the same reason, the effect of D_T is also less pronounced at later times when the swimmers are primarily confined to the bulk (not shown).

Figure 2.4a shows the regularized radial probability density in 3D for small $D_T (= 10^{-4})$ where the run and tumble motion dominates. The evolution with time is similar to 2D, but the probability density peaks just before the front and sharply reduces to a finite value at the front. Thus, unlike 2D, there is no additional, algebraic, divergence behind the front in this case. Figure 2.4a shows that the sharpness of the peak reduces with increasing time and figure 2.4b shows that with increasing D_T the peak at the front disappears. To more closely

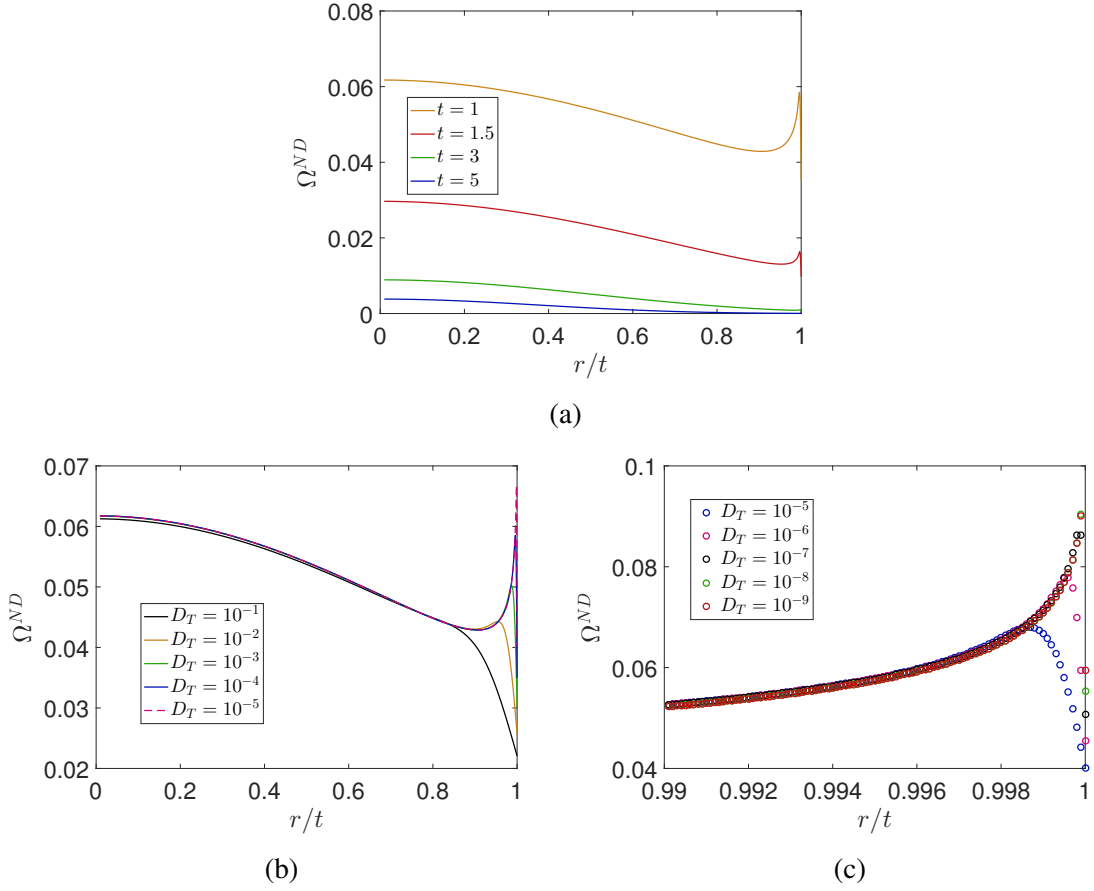


Fig. 2.4 (a) The variation of the regularized position-space probability density, $\Omega^{ND}(r)$ with the scaled radial distance, r/t in 3D for $D_T = 10^{-4}$ at various time t . (b) The affect of the translational diffusivity (D_T) on the regularized position-space probability density, $\Omega^{ND}(r)$ in 3D at $t = 1$. (c) The structure of $\Omega^{ND}(r)$ just behind the front ($0.99 < r < 1$) upon decreasing translational diffusivity (D_T) in 3D at $t = 1$.

examine what happens to the front, we examine the regularized position-space probability density, $\Omega^{ND}(r)$, just behind the front for $0.99 < r < 1$ upon decreasing D_T in figure 2.4c, which shows that the finite value of the regularized radial probability density just behind the front in 3D is not due to a finite D_T .

2.3.3 Orientation-position-space Probability density

The probability density, $\Omega(\mathbf{r}, \mathbf{p}, t)$, of finding a swimmer with orientation \mathbf{p} at position \mathbf{r} at time t , starting from an isotropically localized population at the origin at $t = 0$, is obtained by Fourier inversion of the expressions in (2.47) and (2.48), and the results are presented in this section.

Radial Variation in 2D

In 2D, using a \mathbf{p} -aligned co-ordinate system, where the position-vector \mathbf{r} is given by $(r \cos \chi, r \sin \chi)$ in 2D we get from (2.47),

$$\begin{aligned} \Omega(r, \chi, t) = & \frac{1}{2\pi} \int_0^\infty dk \int_{-\pi}^\pi d\theta e^{2\pi i k r (\cos \theta \cos \chi + \sin \theta \sin \chi)} \int_{-\pi}^\pi \frac{\Phi_{cs}^e(\theta; \theta_0)}{D(\theta_0)} e^{-2\pi i k \cos \theta_0 t - t} d\theta_0 \\ & + \int_0^\infty dk \int_{-\pi}^\pi d\theta e^{2\pi i k r (\cos \theta \cos \chi + \sin \theta \sin \chi)} \frac{1}{2\pi} \Phi_d^e(\theta; \theta_d) \frac{4\pi^2 i k}{\int_{-\pi}^\pi (\cos \theta - \cos \theta_d)^{-2} d\theta} e^{-2\pi i k \cos \theta_d t - t} \\ & + \int_0^\infty dk \int_{-\pi}^\pi d\theta e^{2\pi i k r (\cos \theta \cos \chi + \sin \theta \sin \chi)} \frac{1}{2\pi} \sum_{\pm \arcsin\left(\frac{1}{2\pi k U_s \tau}\right)} \Phi_l^e(\theta; \theta_l) \frac{i\pi \sin \theta_l}{2 \cos \theta_l} e^{-2\pi i k \cos \theta_l t - t}. \end{aligned} \quad (2.57)$$

The Fourier inversion is performed by carrying out the integrals numerically as in the previous section. We again expect to find a ‘front’ contribution of the form $\delta(r-t)\delta(\chi)e^{-t}$ due to a bacteria that has not tumbled since $t=0$. Like the previous section, we subtract this contribution from the probability density to regularize it, the regularized probability density being denoted by Ω^{ND} . We present results for $\Omega^{ND}(r, \chi, t) = \Omega(r, \chi, t) - \delta(r-t)\delta(\chi)e^{-t}$ in the rest of the section. Figure 2.5a-f show the regularized probability density $\Omega^{ND}(r, \chi, t)$ versus r in 2D for various t and relative angles χ ; note that for any $\chi \neq 0$, we have $\Omega^{ND} = \Omega$ since no regularization is required at the front for $\chi \neq 0$.

To examine swimmers aligned with the radial location ($\chi=0$) in more detail, in addition to 2.5a, we plot $\Omega^{ND}(r, \chi=0, t)$ versus $1-r/t$ on a log-log plot in figure 2.6. This suggests a power-law scaling for $\Omega^{ND}(r, \chi=0, t) \propto \frac{1}{t-r}$. The scaling is seen to hold everywhere in the bulk at early times ($t < 1$) but is confined near the front for increasing t . The divergence at the front is numerically regularized in a boundary layer at any finite translational-diffusivity as it must be but we can capture the behavior sufficiently with $D_T = 10^{-3}$. Solon et al. [2015] saw the same scaling for RTPs trapped in a potential-well when the trap radius was smaller than the run-length ($U\tau$). In the previous section, we saw that the divergence for the orientation-averaged position space probability density is milder $\propto \frac{1}{(t-r)^{1/2}}$. This suggests that a differential angular element of $O((t-r)^{1/2})$ is the dominant contribution to the orientation average. For longer times, the swimmers accumulate in two-distinct regions, a diffusive region in the bulk with the swimmers concentrated near the origin and another region near the front where again $\Omega(r, \chi=0, t) \propto \frac{1}{t-r}$. With increasing time, we thus see a transition from an active-regime to a passive-regime.

We see similar phenomenology for other values of χ (see figure 2.5b-f). At early times, one still sees accumulation near the front; however with increasing χ the maxima of $\Omega(r, \chi, t)$

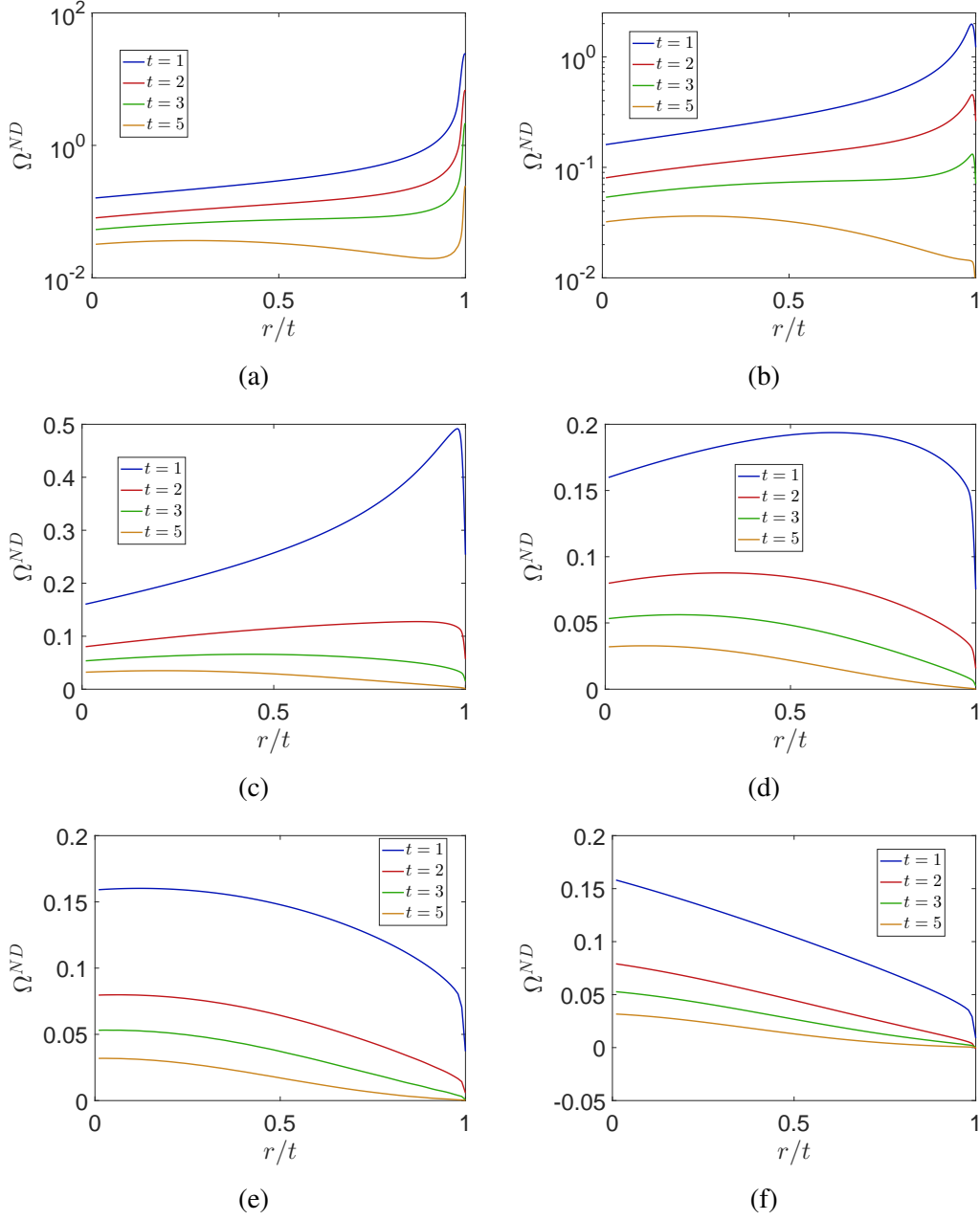


Fig. 2.5 The variation of the regularized joint orientation-position space probability density, $\Omega^{ND}(r, \chi, t)$ with the scaled radial distance, r/t in 2D for various χ (a) $\chi = 0$, (b) $\chi = 2\pi/30$, (c) $\chi = 5\pi/30$, (d) $\chi = 10\pi/30$, (e) $\chi = 14\pi/30$ and (f) $\chi = 20\pi/30$; at various time t with $D_T = 10^{-3}$.

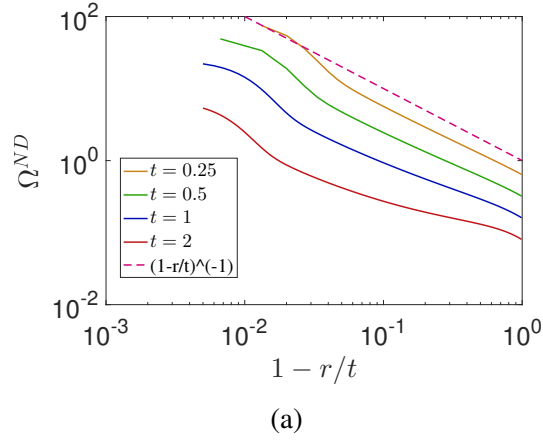


Fig. 2.6 The variation of the regularized orientation-position space probability density, $\Omega^{ND}(r, \chi = 0, t)$ with the scaled radial distance, $1 - r/t$ in 2D for $\chi = 0$ at various time t with $D_T = 10^{-3}$.

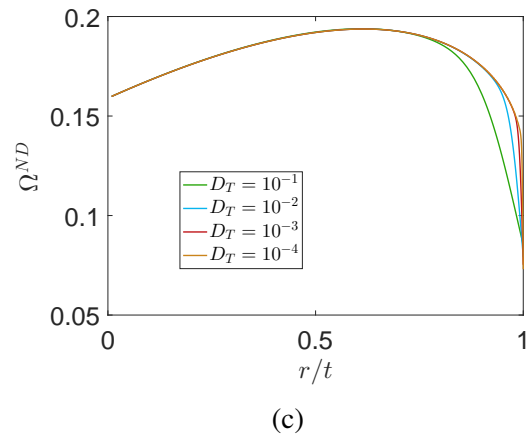
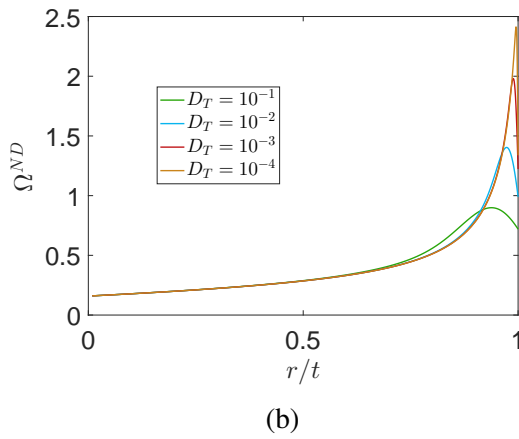
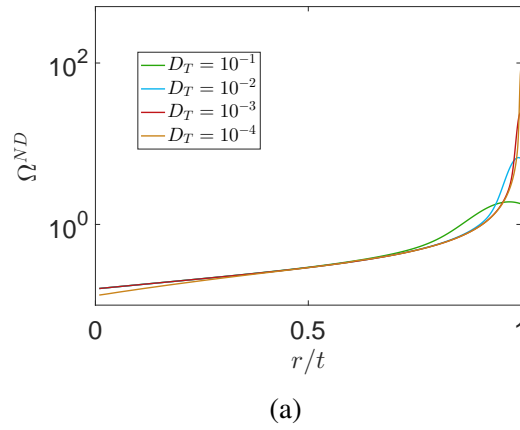


Fig. 2.7 The effect of the translational diffusivity (D_T) on the regularized orientation-position space probability density, $\Omega^{ND}(r, \chi, t)$ in 2D at $t = 1$ for (a) $\chi = 0$ (b) $\chi = 2\pi/30$ (c) $\chi = 10\pi/30$.

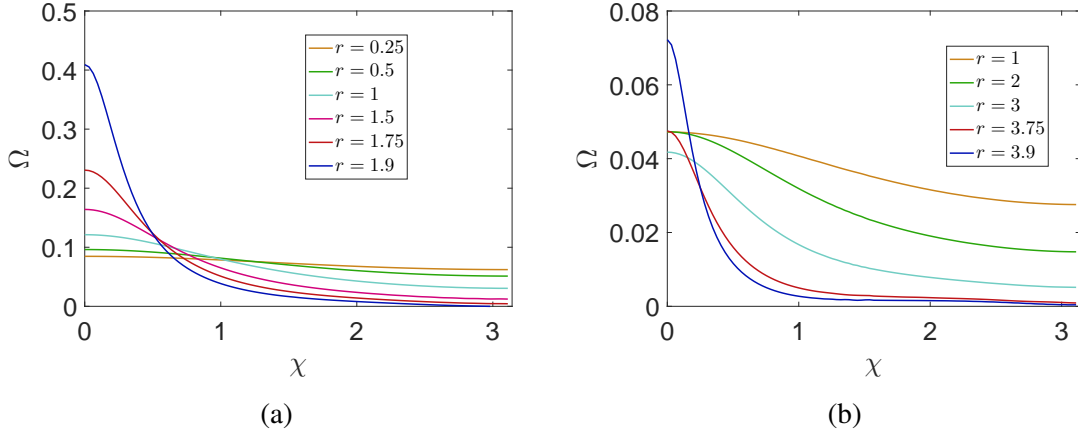


Fig. 2.8 The angular variation of the joint orientation-position space probability density, $\Omega^{ND}(r, \chi, t)$ with χ in 2D for various r at time (a) $t = 2$ and (b) $t = 4$ for $D_T = 10^{-3}$.

moves away from the front and towards the origin. As $\chi \sim \pi/2$ we see that the maxima has moved to the origin (figure 2.5e). For $\chi > \pi/2$, the maximum number of swimmers is at the origin even at early times, and $\Omega(r, \chi, t)$ is a monotonically decreasing function of r . However, the functional form of $\Omega(r, \chi, t)$ is still distinct from a Gaussian at early times for any χ . At long times one sees the expected transition to the diffusive regime for any value of χ , with $\Omega(r, \chi, t)$ having a maxima at the origin. Thus we see that there is an active-regime to a passive-regime transition with time for any value of χ , although the form of the active regime is itself dependent on χ . Malakar et al. [2018] have also found a similar active-passive transition for RTPs in one-dimension.

Figure 2.7a-c shows results for joint orientation-position for varying D_T . The effect of the translational diffusivity is the largest for aligned swimmers i.e. for $\chi = 0$. As D_T is reduced, the algebraic divergence extends further upto the front, while the probability density in the bulk stays unaffected (see figure 2.7a). Thus in the absence of the translational diffusivity, the probability distribution would diverge linearly on approaching the front. For $\chi \neq 0$, the effect of translational diffusivity is not as pronounced. Further note that there is no divergence at the front even in the limit of $D_T \rightarrow 0$ for non-aligned swimmers (see figure 2.7b-c).

Angular Variation in 2D

Figure 2.8a-b shows the angular variation of $\Omega(r, \chi, t)$ with χ at a given radial location and time. We see that the swimmers are isotropically distributed near the origin, with $\Omega(r, \chi, t)$ becoming increasingly anisotropic as we approach the front at $r = t$. Clearly, the closer the swimmer is found to the front, the more aligned its orientation would be with the radial vector. The probability of non-aligned swimmers ($\chi \neq 0$) while approaching the front is

finite; this can also be seen in figure 2.5. In contrast to the radial variation discussed earlier, we see no qualitative change in the angular variation with increasing time.

Radial Variation in 3D

In 3D, the position vector \mathbf{r} in the \mathbf{p} -aligned coordinate system is given by $(r \cos(\chi), r \sin(\chi) \sin(\psi), r \sin(\chi) \cos(\psi))$. Clearly for an isotropic initial condition, $\Omega(\mathbf{r}, \mathbf{p}, t)$ must be invariant of ψ for all times, so we only consider $\psi = 0$ here. Thus the joint probability density is again given as $\Omega(r, \chi, t)$ in 3D. The final expression is derived from (2.48) and is given as,

$$\begin{aligned} \Omega(r, \chi, t) = & \frac{1}{2} \int_0^\infty dk \int_{-1}^1 d\mu e^{2\pi i k r \mu \cos \chi} \int_{-1}^1 \frac{\Phi_{cs}^0(\mu; \mu_0)}{D(\mu_0)} e^{-2\pi i k \mu_0 t - t} d\mu_0 \\ & + \frac{1}{2} \int_0^\infty dk \int_{-1}^1 d\mu e^{2\pi i k r \mu \cos \chi} \mathcal{H} \left(\frac{1}{4U_s \tau} - k \right) \Phi_d^0(\mu; \mu_d) \frac{4\pi i k}{\int_{-1}^1 (\mu - \mu_d)^{-2} d\mu} e^{-2\pi i k \mu_d t - t}. \end{aligned} \quad (2.58)$$

Figure 2.9a-c shows the variation of $\Omega^{ND}(r, \chi, t)$ versus r for various times t and polar angles χ . We thus see that the joint orientation-position dynamics are similar to that in 2D. For aligned swimmers ($\chi = 0$), figure 2.10 shows the log plot of $\Omega^{ND}(r, \chi = 0, t)$ versus $1 - r/t$ which shows that the power-law scaling for aligned swimmers is different from 2D and is given by $\Omega^{ND}(r, \chi = 0, t) \propto \frac{1}{(t-r)^2}$. The angular variation of $\Omega(r, \chi, t)$ in 3D is similar to 2D and hence is not presented.

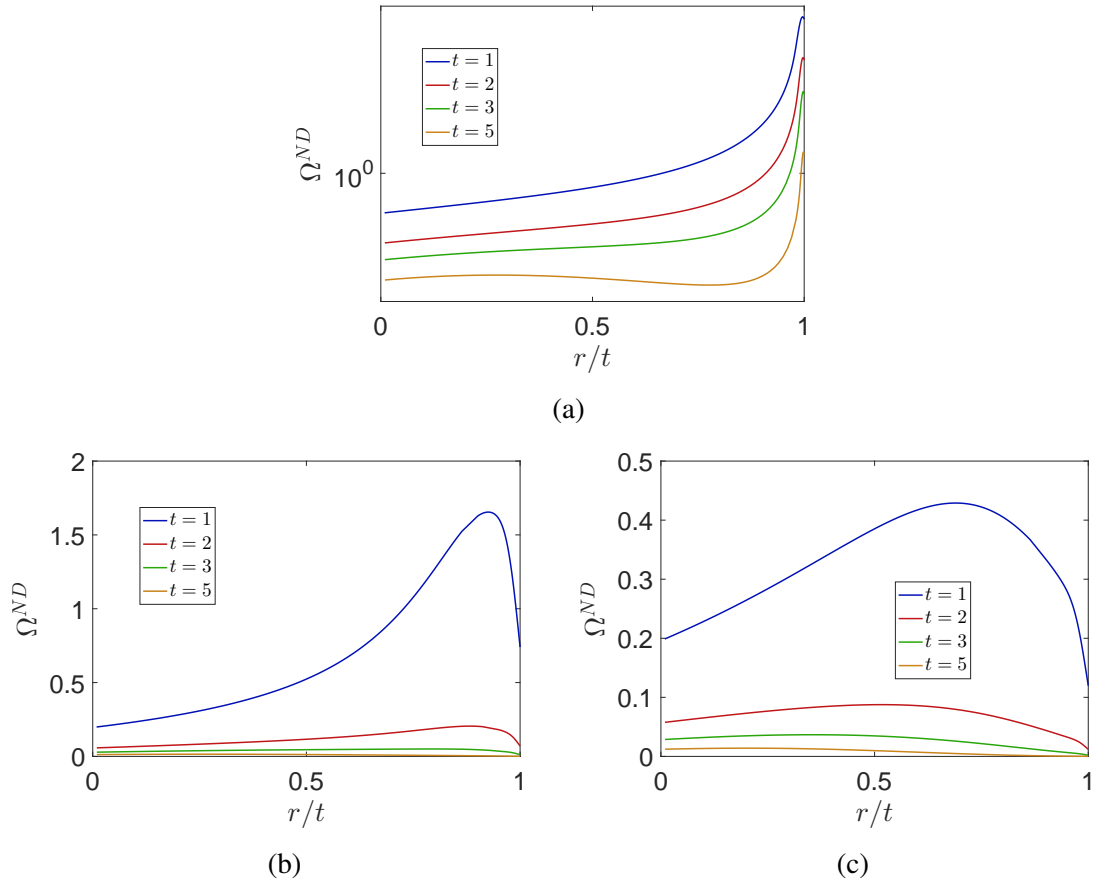


Fig. 2.9 The variation of the joint regularized orientation-position space probability density, $\Omega^{ND}(r, \chi, t)$ with the scaled radial distance, r/t in 3D for various χ (a) $\chi = 0$, (b) $\chi = 2\pi/30$, and (c) $\chi = 5\pi/30$.

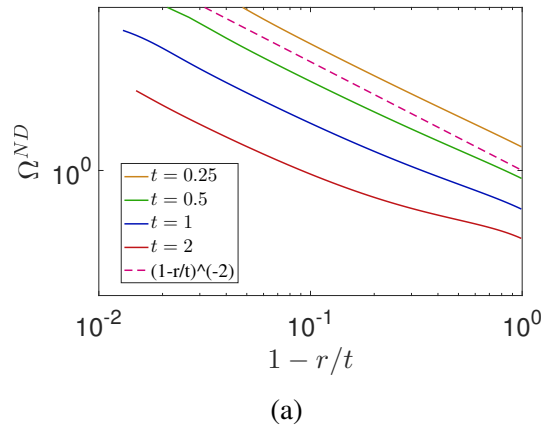


Fig. 2.10 The variation of the joint regularized orientation-position space probability density, $\Omega^{ND}(r, \chi = 0, t)$ with the scaled radial distance, $1 - r/t$ in 3D for $\chi = 0$ for $D_T = 10^{-3}$.

2.4 Conclusion

In this chapter, we have presented an exact solution for the time evolution of the joint-probability density in orientation-position space of run-and-tumble particles. We constructed the Green's function of the run-and-tumble operator by deriving analytical expressions for the eigenfunctions and their adjoints, and constructing the required bilinear superposition. We have provided exact results in both two and three dimensions. Importantly, the eigenspectrum governing the dynamics of RTPs would consist of a swimming-induced continuous spectrum, and a regular discrete mode corresponding to long-time diffusive behavior, in any arbitrary dimension greater than one. The Green's function can also thus be constructed in any arbitrary dimension following the method detailed in this chapter. We also showed that there is an active to passive-regime transition with increasing time for the radial variation of the joint probability density. This transition occurred in both two and three dimensions and should persist in all higher dimensions.

Further generalizations are possible using the formalism developed in this chapter. It is evident that our approach can be extended to dimensions higher than three. In arbitrary dimension D , we would consider hyper-spherical polar coordinates, the radius (r), $D - 2$ polar angles and an azimuthal angle. By writing the swimming dependency in terms of the $D - 2$ polar angles and expanding the remaining polar angles dependency in terms of the Legendre polynomials, we can separate out the equation for the concentration perturbation. One would thus obtain a similar eigenspectrum in all higher dimensions, comprising of the swimming induced continuous spectrum and the discrete mode that reduces to diffusion in the $k \rightarrow 0$ limit.

Here, we have considered the simplest realization of RTPs, where the runs are instantaneous and Poisson distributed. In nature bacteria show several variations on this basic paradigm, some of which have been studied in the literature recently where the tumbles could take a finite amount of time or the tumbles are correlated to each other [Angelani, 2013; Detcher, 2015, 2017; Stocker, 2011; Taktikos et al., 2013]. Our method could be extended to study the dynamics of generic run-and-tumble motion, however it is not a priori obvious whether complete analytic progress can be made in the general case. Further, run-and-tumble particles subject to an external harmonic potential or shearing flows lead to non-trivial dynamics and steady-state probability distributions, and have thus been intensely studied in recent years [Cates, 2012; Malakar et al., 2018; Nash et al., 2010; Sandoval et al., 2014; Solon et al., 2015; Vennamneni et al., 2020; Woillez et al., 2019].

Importantly, the methodology described in this chapter can be extended to study the dynamics of hydrodynamically interacting RTPs. This is done in the next chapter to study correlations in a bacterial suspension on approaching the collective motion threshold.

2.5 Derivation of the adjoint eigenfunctions

2.5.1 Finding the adjoint eigenfunctions: 2D

To derive the adjoint eigenfunctions, we consider an arbitrary initial condition $B(\theta, k)$. For the eigenfunctions (and adjoints) since k can be considered to be fixed, $B(\theta, k) \equiv B(\theta)$ can be an arbitrary function of θ with k being treated as a parameter in the following analysis to derive the adjoint eigenfunctions. $B(\theta)$ can be projected onto the eigenfunctions discussed earlier. In 2D this gives

$$B(\theta) = \int_{-\pi}^{\pi} \Lambda_{cs}(\theta_0) \phi_{cs} d\theta_0, \quad (2.59)$$

where $\Lambda_{cs}(\theta_0)$ is the unknown amplitude distribution that needs to be found. Without loss of generality, we can separate any initial condition into odd and even parts. The odd component of the initial condition clearly projects only onto the odd eigen-modes,

$$B(\theta) - B(-\theta) = \int_{-\pi}^{\pi} \Lambda_{cs}^o(\theta_0) \Phi_{cs}^o d\theta_0, \quad (2.60)$$

and using the expression for Φ_{cs}^o , from (2.27), we get

$$B(\theta) - B(-\theta) = \Lambda_{cs}^o(\theta) - \Lambda_{cs}^o(-\theta), \quad (2.61)$$

For purposes of deriving the adjoint, we take $B(\theta) = \delta(\theta - \theta')$, in which case $\Lambda_{cs}^o = \tilde{\Phi}_{cs}^o$, and the adjoint of the odd eigenfunction is seen to be given by,

$$\tilde{\Phi}_{cs}^o = \delta(\theta' - \theta_0) - \delta(\theta' + \theta_0). \quad (2.62)$$

For the even component of the initial condition,

$$B(\theta) + B(-\theta) = \int_{-\pi}^{\pi} \Lambda_{cs}^e(\theta_0) \Phi_{cs}^e d\theta_0. \quad (2.63)$$

Using Φ_{cs}^e from (2.14), and on further simplifying, we get:

$$B(\theta) + B(-\theta) = \Lambda^e(\theta) + \Lambda^e(-\theta) + \frac{1}{2\pi^2 ik U_s \tau} \int_0^{\pi} \frac{\Lambda^e(\theta_0) + \Lambda^e(-\theta_0)}{\cos \theta - \cos \theta_0} d\theta_0. \quad (2.64)$$

Note again that when $B(\theta) = \delta(\theta - \theta')$, $\Lambda_{cs}^e = \tilde{\Phi}_{cs}^e$. Thus, unlike the odd component we need to solve the singular integral equation (2.64) for the unknown amplitude Λ_{cs}^e to derive the adjoint eigenfunction. This was first carried out by Case in the context of plasma-oscillations [Case, 1959, 1960] and has since been extended to inviscid shear flows [Balmforth and

[Morrison, 1995b; Roy and Subramanian, 2014b]. Here, we adapt the method for the Fourier transformed run-and-tumble operator. Interpreting θ as a complex variable, we define the following functions:

$$\Phi = \frac{1}{2\pi i} \int_0^\pi \frac{\Lambda^e(\theta_0) + \Lambda^e(-\theta_0)}{\cos \theta - \cos \theta_0} d\theta_0, \quad (2.65)$$

$$\Psi = \frac{1}{2\pi i} \frac{1}{2\pi^2 ik U_s \tau} \int_0^\pi \frac{1}{\cos \theta - \cos \theta_0} d\theta_0, \quad (2.66)$$

and

$$Q = \frac{1}{2\pi i} \int_0^\pi \frac{B(\theta_0) + B(-\theta_0)}{\cos \theta - \cos \theta_0} d\theta_0. \quad (2.67)$$

All the above three functions are singular integrals for $\theta \in [-\pi, \pi]$ so that there is a branch cut for each of the integrals in (2.65)-(2.67). Using the Plemelj formula [Ablowitz et al., 2003; Gakhov, 2014], we get for each of the integrals,

$$\Phi^\pm = \pm \frac{\Lambda^e(\theta) + \Lambda^e(-\theta)}{2(1 - \cos \theta^2)^{1/2}} + \frac{1}{2\pi i} \int_0^\pi \frac{\Lambda^e(\theta_0) + \Lambda^e(-\theta_0)}{\cos \theta - \cos \theta_0} d\theta_0,$$

$$\Psi^\pm = \pm \frac{1}{2\pi^2 ik U_s \tau} \frac{1}{2(1 - \cos \theta^2)^{1/2}},$$

and

$$Q^\pm = \pm \frac{B(\theta) + B(-\theta)}{2(1 - \cos \theta^2)^{1/2}} + \frac{1}{2\pi i} \int_0^\pi \frac{B(\theta_0) + B(-\theta_0)}{\cos \theta - \cos \theta_0} d\theta_0.$$

We can show that

$$Q^+ - Q^- = \Phi^+ - \Phi^- + (2\pi i)(\Phi^+ \Psi^+ - \Phi^- \Psi^-), \quad (2.68)$$

$$Q^+ - \Phi^+ - (2\pi i)(\Phi^+ \Psi^+) = Q^- - \Phi^- - (2\pi i)(\Phi^- \Psi^-), \quad (2.69)$$

$$(2.70)$$

and hence the the particular combination of Q , Φ and Ψ given by $Q - \Phi - (2\pi i)(\Phi\Psi)$ is continuous about the branch cut and by definition has no singularities elsewhere in the complex plane. By using the Liouville theorem [Ablowitz et al., 2003; Gakhov, 2014], we can then say that this combination must be a constant which then leads to,

$$\implies Q - \Phi - (2\pi i)(\Phi\Psi) = \text{const.} = 0 \quad (2.71)$$

$$\implies \Phi = \frac{Q}{1 + 2\pi i\Psi}. \quad (2.72)$$

Finally upon using,

$$\Lambda^e(\theta) + \Lambda^e(-\theta) = (\Phi^+ - \Phi^-)(1 - \cos \theta^2)^{1/2} \quad (2.73)$$

$$= \left(\frac{Q^+}{1 + 2\pi i \Psi^+} - \frac{Q^-}{1 + 2\pi i \Psi^-} \right) \frac{(1 - \cos \theta^2)^{1/2}}{2}, \quad (2.74)$$

and simplifying we get,

$$\Lambda^e(\theta) + \Lambda^e(-\theta) = \frac{B(\theta) - \frac{1}{2\pi^2 ik U_s \tau} \int d\theta_0 \frac{B(\theta_0)}{\cos \theta - \cos \theta_0}}{1 - \frac{1}{(2\pi k U_s \tau \sin \theta)^2}} \quad (2.75)$$

from which we can see the adjoint as,

$$\tilde{\Phi}_{cs}^e(\theta_0; \theta') = \frac{1}{D(\theta_0)} \left(\delta(\theta' - \theta_0) + \delta(\theta' + \theta_0) + \frac{1}{2\pi^2 ik U_s \tau} \mathcal{P} \frac{1}{\cos \theta' - \cos \theta_0} \right), \quad (2.76)$$

which was stated in (2.28).

2.5.2 Finding the adjoint eigenfunctions: 3D

The procedure to derive the adjoint in 3D follows similar steps. We represent an arbitrary condition $B(\mu, \phi)$, without loss of generality, in terms of axisymmetric and non-axisymmetric modes,

$$B(\mu, \phi) = B^0(\mu) + \sum_{m=1}^{\infty} B^m(\mu) \cos(m\phi). \quad (2.77)$$

It is evident that each of the modes would project independently unto the corresponding eigenfunctions. Thus, we get for the non-axisymmetric modes,

$$B^m(\mu) = \int_{-1}^1 \Lambda^m(\mu_0) \Phi_{cs}^m(\mu; \mu_0) d\mu_0. \quad (2.78)$$

Using Φ_{cs}^m s from (2.15), we arrive at the adjoint expression in (2.30) for the non-axisymmetric modes. For the axisymmetric mode,

$$B^0(\mu) = \int_{-1}^1 \Lambda^0(\mu_0) \Phi_{cs}^0(\mu; \mu_0) d\mu_0. \quad (2.79)$$

and using Φ_c^0 s from (2.16), we get.

$$B^0(\mu) = \left[\Lambda^0(\mu) - \frac{\Lambda^0(\mu)}{4\pi i k U_s \tau} \int_{-1}^1 \frac{1}{\mu' - \mu} d\mu' \right] + \frac{1}{4\pi i k U_s \tau} \int_{-1}^1 \frac{\Lambda^0(\mu)}{\mu - \mu_0} d\mu'. \quad (2.80)$$

with $\Lambda^0(\mu_0)$ is the amplitude that needs to be solved for. An integral equation (2.80) needs to be inverted just like the 2D case [Balmforth and Morrison, 1995b; Case, 1959, 1960; Roy and Subramanian, 2014b]. Again, three functions $\chi(\mu)$, $\Psi(\mu)$ and $Q(\mu)$ are defined:

$$\chi(\mu) = \frac{1}{2\pi i} \int_{-1}^1 \frac{\Lambda^0(\mu')}{\mu - \mu'} d\mu', \quad (2.81a)$$

$$\Psi(\mu) = \frac{1}{2\pi i} \left(\frac{1}{U_s \tau} \right) \int_{-1}^1 \frac{1}{\mu - \mu'} d\mu', \quad (2.81b)$$

$$Q(\mu) = \frac{1}{2\pi i} \int_{-1}^1 \frac{B(\mu')}{\mu - \mu'} d\mu'. \quad (2.81c)$$

(2.81a)-(2.81c) are singular integrals, for $\mu \in [-1, 1]$, implying that this interval is the branch cut. We therefore, use the Plemelj formulae [Ablowitz et al., 2003; Gakhov, 2014] to get:

$$\chi(\mu)^\pm = \pm \frac{\Lambda^0(\mu)}{2} + \frac{1}{2\pi i} \int_{-1}^1 \frac{\Lambda^0(\mu')}{\mu - \mu'} d\mu' \quad (2.82a)$$

$$\Psi(\mu)^\pm = \pm \frac{1}{2} \left(\frac{1}{U_s \tau} \right) + \frac{1}{2\pi i} \left(\frac{1}{U_s \tau} \right) \int_{-1}^1 \frac{1}{\mu - \mu'} d\mu' \quad (2.82b)$$

$$Q(\mu)^\pm = \pm \frac{B^0(\mu)}{2} + \frac{1}{2\pi i} \int_{-1}^1 \frac{B^0(\mu')}{\mu - \mu'} d\mu'. \quad (2.82c)$$

Again $Q^+ - Q^- = \chi^+ - \chi^- + 2\pi i(\Phi^+\Psi^+ - \Phi^-\Psi^-)$, so $Q^+ - \chi^+ - 2\pi i\chi^+\Psi^+ = Q^- - \chi^- - 2\pi i\chi^-\Psi^-$. Just like the 2D case, $Q - \chi - 2\pi i\chi\Psi$ is continuous about the branch cut, and since its analytic everywhere else by definition, it is analytic in the finite complex plane. Moreover, the fact that an entire function can only be a constant [Ablowitz et al., 2003; Gakhov, 2014], and that each of the three functions decay to 0 as $\mu_0 \rightarrow \infty$, gives $Q - \chi - 2\pi i\chi\Psi = 0$, or:

$$\chi = \frac{Q}{(1 + 2\pi i\Psi)}. \quad (2.83)$$

From (2.82a), $\Lambda^0(\mu) = \chi^+ - \chi^-$, and on using (2.81b)-(2.81c) in (2.83), the amplitude is now expressible as:

$$\Lambda^0(\mu) = \int_{-1}^1 d\mu_0 B^0(\mu_0) \frac{1}{D(\mu)} \left\{ \left[1 - \frac{1}{4\pi ik U_s \tau} \int_{-1}^1 \frac{1}{\mu' - \mu_0} d\mu' \right] \delta(\mu - \mu_0) - \frac{1}{4\pi ik U_s \tau} \frac{1}{\mu - \mu_0} \right\}, \quad (2.84)$$

$$D(\mu) = 1 - \frac{1}{2\pi ik U_s \tau} \int_{-1}^1 \frac{1}{\mu' - \mu} d\mu' - \left(\frac{1}{4k U_s \tau} \right)^2 \left[1 + \left(\frac{1}{\pi} \int_{-1}^1 \frac{1}{\mu' - \mu} d\mu' \right)^2 \right]. \quad (2.85)$$

For $B^0(\mu) = \delta(\mu - \mu')$, we obtain the adjoint expression

$$\tilde{\Phi}_{cs}^0(\mu_0; \mu') = \frac{1}{D(\mu_0)} \left(\left[1 - \frac{1}{4\pi ik U_s \tau} \int_{-1}^1 \frac{1}{\mu'' - \mu_0} d\mu'' \right] \delta(\mu' - \mu_0) + \frac{1}{4\pi ik U_s \tau} \mathcal{P} \frac{1}{\mu' - \mu_0} \right), \quad (2.86)$$

which was stated in (2.31).

2.5.3 Normalization of the direct and adjoint eigenfunctions

Following Case [1959], the continuous spectrum eigenfunction for the even mode in 2D is normalized as,

$$\begin{aligned} \int_{-\pi}^{\pi} \Phi_{cs}^e(\theta; \theta_0) d\theta &= \int_{-\pi}^{\pi} \delta(\theta - \theta_0) + \delta(\theta + \theta_0) + \frac{1}{2\pi^2 ik U_s \tau} \mathcal{P} \frac{1}{\cos \theta - \cos \theta_0} d\theta \\ &= 1, \end{aligned} \quad (2.87)$$

where we have used that the PV-integral is the Glauert's integral and similarly for the adjoint eigenfunction

$$\begin{aligned} \int_{-\pi}^{\pi} \tilde{\Phi}_{cs}^e(\theta_0; \theta') d\theta' &= \int_{-\pi}^{\pi} \frac{1}{D(\theta_0)} \left(\delta(\theta' - \theta_0) + \delta(\theta' + \theta_0) + \frac{1}{2\pi^2 ik U_s \tau} \mathcal{P} \frac{1}{\cos \theta' - \cos \theta_0} \right) d\theta' \\ &= \frac{1}{D(\theta_0)}. \end{aligned} \quad (2.88)$$

Proceeding in the same manner we can easily derive the normalization in 3D as follows for the axisymmetric continuous spectrum eigenfunction,

$$\int_{-1}^1 \Phi_{cs}^0(\mu; \mu_0) d\mu = 1, \quad (2.89)$$

and similarly, for the corresponding adjoint eigenfunction

$$\int_{-1}^1 \tilde{\Phi}_{cs}^0(\mu_0; \mu') d\mu' = \frac{1}{D(\mu_0)}. \quad (2.90)$$

The normalization for the discrete mode in 2D gives,

$$\int_{-\pi}^{\pi} \Phi_d^e(\theta; \theta) d\theta = 4\pi^2 ik U_s \tau, \quad (2.91)$$

where we have used the dispersion relation in (2.18). Similarly for the adjoint,

$$\int_{-\pi}^{\pi} \tilde{\Phi}_d^e(\theta_d; \theta') d\theta' = \frac{4\pi^2 ik U_s \tau}{\int_{-\pi}^{\pi} (\cos \theta - \cos \theta_d)^{-2} d\theta}. \quad (2.92)$$

In 3D for the discrete mode we have,

$$\int_{-1}^1 \Phi_d^0(\mu; \mu_d) d\mu = 4\pi ik U_s \tau, \quad (2.93)$$

and for the adjoint,

$$\int_{-1}^1 \tilde{\Phi}_d^0(\mu_d; \mu') d\mu' = \frac{4\pi ik U_s \tau}{\int_{-1}^1 (\mu - \mu_d)^{-2} d\mu}, \quad (2.94)$$

2.5.4 Orthogonality of the eigenfunctions

The continuous spectrum eigenfunctions further satisfy the orthogonality constraint,

$$\int_{-1}^1 \Phi_{cs}^0(\mu; \mu_0) \tilde{\Phi}_{cs}^0(\mu_0; \mu') d\mu_0 = \delta(\mu - \mu'). \quad (2.95)$$

Using the expressions for Φ_{cs}^0 from (2.16) and $\tilde{\Phi}_{cs}^0$ from (2.31) gives,

$$\begin{aligned}
& \int_{-1}^1 d\mu_0 \Phi_{cs}^0(\mu; \mu_0) \tilde{\Phi}_{cs}^0(\mu_0; \mu') d\mu_0 \\
&= \frac{1}{D(\mu')} \left[\left(1 - \frac{1}{4\pi ik U_s \tau} \int_{-1}^1 \frac{1}{\mu'' - \mu'} d\mu'' \right)^2 \delta(\mu - \mu') \right. \\
&\quad - \frac{1}{4\pi ik U_s \tau} \left(1 - \frac{1}{4\pi ik U_s \tau} \int_{-1}^1 \frac{1}{\mu'' - \mu} d\mu'' \right) \frac{1}{\mu' - \mu} \\
&\quad + \frac{1}{4\pi ik U_s \tau} \left(1 - \frac{1}{4\pi ik U_s \tau} \int_{-1}^1 \frac{1}{\mu'' - \mu'} d\mu'' \right) \frac{1}{\mu' - \mu} \\
&\quad \left. - \left(\frac{1}{4\pi ik U_s \tau} \right)^2 \int_{-1}^1 d\mu_0 \frac{1}{\mu_0 - \mu} \frac{1}{\mu_0 - \mu'} \right]. \quad (2.96)
\end{aligned}$$

On recasting the final integral term on the right-hand side of (2.96) using the Poincaré-Bertrand theorem [Balmforth and Morrison, 1995b; Gakhov, 2014], one obtains:

$$\begin{aligned}
& \int_{-1}^1 d\mu_0 \mathcal{P} \left[\frac{1}{\mu_0 - \mu} \right] \mathcal{P} \left[\frac{1}{\mu_0 - \mu'} \right] = -\pi^2 \delta(\mu - \mu') \\
&\quad + \frac{1}{\mu' - \mu} \left[\int_{-1}^1 \frac{1}{\mu'' - \mu} d\mu'' - \int_{-1}^1 \frac{1}{\mu'' - \mu'} d\mu'' \right], \quad (2.97)
\end{aligned}$$

which when used in (2.96), yields (2.95).

Similarly one can, easily, verify that the continuous spectrum and the discrete mode are orthogonal to each other,

$$\int_{-1}^1 \Phi_d^0(\mu; \mu_d) \tilde{\Phi}_{cs}^0(\mu_0; \mu) d\mu = 0, \quad (2.98)$$

and

$$\int_{-1}^1 \Phi_{cs}^0(\mu; \mu_0) \tilde{\Phi}_d^0(\mu_d; \mu) d\mu = 0. \quad (2.99)$$

This ensures that any initial condition has independent projections on the continuous-spectrum and discrete mode eigenfunctions, and implies the validity of the generic expression for the Green's function (2.39) [Friedman, 1990]. Analogous relations can be readily derived for the 2D eigenfunctions and the derivation is omitted for brevity.

Chapter 3

Fluctuating kinetic theory for bacterial suspensions

3.1 Introduction

In the previous chapter we theoretically examined the dynamics of non-interacting run-and-tumble particles, the latter being a standard paradigm for active particles. A collection of such particles is often termed ‘active matter’ and has been widely studied in recent years [Bechinger et al., 2016; Cates, 2012; Marchetti et al., 2013]. Active particles, by definition, inject energy at the micro-scale and break time reversal-symmetry. Consequently, active matter systems can often lead to non-trivial dynamics forbidden by symmetry in equilibrium (or near-equilibrium) systems [Cates, 2012; Chaikin and Lubensky, 2000]. Thus, there has been a lot of effort in understanding interactions between active particles, and how such interactions can often lead to novel and non trivial dynamics on length scales much larger than the individual particle. For instance, simple orientation-based nearest neighbor interactions leads to flocking (interpreted as a phase transition) in 2D, seemingly in violation of the Mermin-Wagner-Hohenberg theorem that holds for equilibrium systems [Chaté, 2020; Vicsek and Zafeiris, 2012]. In another case, it has been shown that phase separation can occur in a system of dense active particles with purely repulsive interactions [Cates and Tailleur, 2015; Stenhammar et al., 2013; Wittkowski et al., 2014]. Such models for active matter do not involve hydrodynamic interactions, and can be termed as dry active matter.

In contrast, a wide variety of active matter does involve hydrodynamic interactions, termed as ‘wet active matter’ [Elgeti et al., 2015; Koch and Subramanian, 2011; Thampi and Yeomans, 2016; Zöttl and Stark, 2016]. Bacterial suspensions have been extensively studied, both experimentally [Dombrowski et al., 2004; Gachelin et al., 2014] and computationally and

theoretically [Marchetti et al., 2013; Wensink et al., 2012], over recent years, as a prototypical example of wet active-matter systems. Further, both dilute and concentrated bacterial suspensions have been thoroughly investigated, with novel phenomena observed in both regimes [Baskaran and Marchetti, 2009; Chen et al., 2017; Dombrowski et al., 2004; Koch and Subramanian, 2011]. For dilute bacterial suspensions, several instances of non-trivial dynamics find mention in the literature. These include examples where a passive tracer in the suspension exhibits an enhanced diffusivity due to swimmer-induced velocity fluctuations [Chen et al., 2007b; Jepson et al., 2013; Wu and Libchaber, 2000]. Such suspensions have also shown to possess novel rheological properties, including regimes of superfluidity, due to the active stress induced by swimming bacteria [López et al., 2015; Nambiar et al., 2017, 2019]. Further, long-ranged hydrodynamic interactions lead to ‘collective-motion’ in bacterial suspensions on length scales much larger than a single-bacterium [Koch and Subramanian, 2011; Saintillan and Shelley, 2007]. Collective motion onset is dependent on the bacterial volume fraction, occurring beyond a finite threshold that involves both the volume fraction and appropriately scaled tumble time [Subramanian and Koch, 2009]. Numerical simulations have also shown non-trivial long-ranged orientation and velocity correlations in dilute bacterial suspensions [Bárdfalvy et al., 2019; Krishnamurthy and Subramanian, 2015; Stenhammar et al., 2017]. Owing to the expense involved in simulating bacterial suspensions on large scales, the exact dynamics that contribute to the correlations, especially close to collective motion onset, are not well understood, and complementary theoretical approaches are needed.

As discussed in Chapter 2, individual bacteria are effectively modeled as run and tumble particles (RTPs), where the run phase denotes the bacterium swimming through the fluid along a straight line between successive (random) tumbles. Interactions in dilute bacterial suspensions are primarily hydrodynamic, being mediated through the fluid flows generated due to swimming [Koch and Subramanian, 2011]. Since the swimming motion is force-free, the bacteria appear as dipoles in the far-field, and are termed ‘pushers’ owing to the fluid flow pointing outwards along the axis of the bacterium. There is a second class of microswimmers, examples of which include algae, where the flow is directed inwards along the swimming axis - these are termed ‘pullers’. The long-ranged $O(1/r^2)$ fluid flow (r being the distance from the bacterium) induced by the swimming motion of the bacterial dipoles is thus crucial to the dynamics of dilute suspensions. Only dilute suspensions of pushers, like bacteria, are known to exhibit collective motion. Building on the results from the previous chapter, herein, we theoretically study the correlations in a dilute bacterial suspension that develops due to the long ranged hydrodynamic interactions.

First, in section 3.2, we study correlations away from the threshold of collective motion. In this regime, it is pairwise hydrodynamic interactions that are dominant. This regime was already analysed in Nambiar [2020] and we extend the analysis to determine the diffusivity of a passive non-Brownian tracer. We show that the tracer diffusivity diverges linearly with the swimmer run length at $O(nL^3)^2$, where nL^3 is the swimmer volume fraction, this divergence arising from a weaker logarithmic divergence of the fluid velocity variance. We also examine the differences between pushers and pullers, and discuss the relevance of these results to recent experimental observations.

In section 3.3, we study the correlations near the threshold of collective motion. For equilibrium systems, correlations near a phase transition are studied using stochastic field theories [Chaikin and Lubensky, 2000]. For example, Model B is used to study the dynamics of a conserved scalar order parameter near a phase transition, while Model H incorporates additional hydrodynamical effects. Existing studies have examined how such field theories behave with additional terms that are used to phenomenologically model the consequences of activity [Cates, 2019; Cates and Tjhung, 2018; Tiribocchi et al., 2015; Tjhung et al., 2018; Wittkowski et al., 2014]. However, such models are not applicable to dilute bacterial suspensions since they do not incorporate the effects of long-ranged hydrodynamic interactions which are crucial to the collective motion [Koch and Subramanian, 2011; Krishnamurthy and Subramanian, 2015; Saintillan and Shelley, 2007; Stenhammar et al., 2017]. To include the effects of such interactions, we develop a fluctuating kinetic theory, from first principles in section 3.3.1 and 3.3.2. Then, following the methodology outlined in Chapter 2, we develop an exact solution of the governing stochastic integro-differential equation in section 3.3.3 and use the same to derive the phase space density correlation function in section 3.3.4. We then use the phase space density correlation function to specifically examine the velocity fluctuations (variance and co-variance), the diffusivity of a passive tracer and the orientation (nematic) correlations as the threshold for collective motion is approached in section 3.3.5. We also examine the differences between suspensions of pushers and pullers. Finally, we conclude in section 3.4.

3.2 Correlations (Tracer diffusivity) away from the collective motion threshold

First, in this section, we examine correlations in a dilute bacterial suspension away from the threshold of collective motion. The latter ensures that the correlations induced by the long wavelength velocity fluctuations in the bacterial suspension are negligible and hence,

all correlations arise due to pairwise interactions between bacteria. The nature of the fluid velocity fluctuations away from the threshold have been studied earlier by Nambiar [2020] where it was observed that direct pair interactions due to the long-ranged disturbance flow fields of individual swimmers lead to a non-trivial variation of the velocity variance with the volume fraction (nL^3) and swimmer run length ($U_s\tau/L$); specifically at $O(nL^3)^2$, the velocity variance diverges logarithmically with the swimmer run length. In this section, we extend the analysis in Nambiar [2020] to examine the diffusivity of a passive tracer away from the threshold of collective motion. Based on the above results for the velocity variance, and in addition the known results for both the velocity variance and tracer diffusivity in a passive suspension of sedimenting non-Brownian particles [Koch and Shaqfeh, 1991], one expects a stronger divergence of the tracer diffusivity with the run length at the same order in nL^3 .

The velocity fluctuations in the bacterial suspension convect a passive non-Brownian tracer. The dynamics of such a tracer is then governed by,

$$\dot{\mathbf{x}} = \mathbf{u}(\mathbf{x}), \quad (3.1)$$

where $\mathbf{u}(\mathbf{x})$ is the suspension velocity field. During a tracer-slender swimmer interaction with a separation of order the swimmer length L (the separations that contribute dominantly to the tracer diffusivity), the velocity convecting the tracer is $O(U/\ln \kappa)$ while the relative tracer-swimmer velocity is $O(U)$; κ here is the swimmer aspect ratio. Thus, the tracer displacement during an interaction event is logarithmically small, and tracer statistics may be calculated, at leading order, within an Eulerian approximation [Kasyap et al., 2014; Krishnamurthy and Subramanian, 2015]. The expression for the mean-squared displacement (MSD) of the tracer, at time t , is then given in terms of the time-dependent fluid velocity correlation function as,

$$\langle x^2(t) \rangle = \int_0^t dt_1 \int_0^t dt_2 \langle \mathbf{u}(\mathbf{r}, t_1) \cdot \mathbf{u}(\mathbf{r}, t_2) \rangle, \quad (3.2)$$

where the angular-brackets again denote an ensemble average [Balakrishnan, 2008; Zwanzig, 2001]. In terms of the Fourier-transformed variables, the tracer MSD is given as,

$$\langle x^2(t) \rangle = \int d\mathbf{k} \int_0^t dt_1 \int_0^t dt_2 \langle \hat{\mathbf{u}}(\mathbf{k}, t_1) \cdot \hat{\mathbf{u}}(-\mathbf{k}, t_2) \rangle, \quad (3.3)$$

which, to $O((nL^3)^2)$, may be written as

$$\langle x^2(t) \rangle = \langle x^2(t) \rangle|_{uncorr} + \langle x^2(t) \rangle|_{corr}, \quad (3.4)$$

where $\langle x^2(t) \rangle|_{uncorr} \sim O(nL^3)$ is the tracer MSD in a non-interacting swimmer suspension, while $\langle x^2(t) \rangle|_{corr} \sim O(nL^3)^2$ denotes the correlated contribution, with the correlation being the consequence of swimmer interactions. We have thus,

$$\langle x^2(t) \rangle|_{uncorr} = \int d\mathbf{k} \int_0^t dt_1 \int_0^t dt_2 \langle \hat{\mathbf{u}}(\mathbf{k}, t_1) \cdot \hat{\mathbf{u}}(-\mathbf{k}, t_2) \rangle|_{uncorr}, \quad (3.5)$$

and

$$\langle x^2(t) \rangle|_{corr} = \int d\mathbf{k} \int_0^t dt_1 \int_0^t dt_2 \langle \hat{\mathbf{u}}(\mathbf{k}, t_1) \cdot \hat{\mathbf{u}}(-\mathbf{k}, t_2) \rangle|_{corr}. \quad (3.6)$$

3.2.1 Suspensions of non-interacting swimmers

For non-interacting swimmers, the Fourier-transformed velocity correlation function is given by

$$\langle \hat{\mathbf{u}}(\mathbf{k}, t_1) \cdot \hat{\mathbf{u}}(-\mathbf{k}, t_2) \rangle|_{uncorr} = \int \hat{\mathbf{u}}(\mathbf{k}) \cdot \hat{\mathbf{u}}(-\mathbf{k}) \hat{G}_1(\mathbf{p}_1, t_1 | \mathbf{p}'_1, t_2; \mathbf{k}) \Omega_1 d\mathbf{p}_1 d\mathbf{p}'_1, \quad (3.7)$$

where $\Omega_1 = n/4\pi$ is the steady-state singlet probability density in an isotropic swimmer suspension, and $\hat{G}_1(\mathbf{p}_1, t_1 | \mathbf{p}'_1, t_2; \mathbf{k})$ is the Fourier transformed transition probability density of finding a swimmer with orientation \mathbf{p}_1 at time t_1 given that it had an orientation \mathbf{p}'_1 at t_2 . The governing equation for \hat{G}_1 is then the same as the equation governing the relaxation of the singlet probability density and is given by,

$$\frac{d\hat{G}_1}{dt} + \left(\frac{U\tau}{L} \right) 2\pi i \mathbf{k} \cdot \mathbf{p}_1 \hat{G}_1 + \left(\hat{G}_1 - \frac{1}{4\pi} \int d\mathbf{p}_1 \hat{G}_1 \right) = \delta(\mathbf{p}_1 - \mathbf{p}'_1) \delta(t - t'). \quad (3.8)$$

The orientation-space eigenmodes of the operator governing the transition probability density, \hat{G}_1 in (3.8), that contribute to the velocity correlation function in (3.7) have no concentration fluctuations. Thus, for these modes, the inverse-tumbling term in (3.8) vanishes and the expression for \hat{G}_1 is then easily given as,

$$\hat{G}_1(\mathbf{p}_1, t | \mathbf{p}'_1, t'; \mathbf{k}) = \delta(\mathbf{p}_1 - \mathbf{p}'_1) \exp \left(\left(-2\pi i \mathbf{k} \cdot \mathbf{p}_1 \frac{U\tau}{L} - 1 \right) (t - t') \right). \quad (3.9)$$

We emphasize that the expression for \hat{G}_1 is not complete since it does not capture the relaxation of the concentration modes. The complete expression for \hat{G}_1 is needed to characterize the time-dependent evolution of a initially localized population of run-and-tumble swimmers, and was discussed in Chapter 2. Using (3.9) in (3.7), and then (3.7) in (3.5) and upon simplifying, we obtain the expression for the MSD of a passive tracer in an isotropic non-interacting

swimmer suspension as:

$$\begin{aligned}
\langle x^2(t) \rangle|_{uncorr} &= \frac{nL^3}{(\ln \kappa)^2 16\pi^7} \int d\mathbf{p}_1 \int \frac{d\mathbf{k}}{k^4} \left(\frac{-1 + \exp\left(-\left(2\pi i \mathbf{k} \cdot \mathbf{p}_1 \frac{U\tau}{L} + 1\right)t\right)}{\left(2\pi i \mathbf{k} \cdot \mathbf{p}_1 \frac{U\tau}{L} + 1\right)^2} \right) \\
&\quad \left(\mathbf{1} - \frac{\mathbf{k}\mathbf{k}}{k^2} \right) : \mathbf{p}_1 \mathbf{p}_1 \frac{\sin^4\left(\frac{\pi}{2} \mathbf{k} \cdot \mathbf{p}_1\right)}{(\mathbf{k} \cdot \mathbf{p}_1)^2} \\
&+ \frac{nL^3}{(\ln \kappa)^2 16\pi^7} t \int d\mathbf{p}_1 \int \frac{d\mathbf{k}}{k^4} \left(\frac{1}{2\pi i \mathbf{k} \cdot \mathbf{p}_1 \frac{U\tau}{L} + 1} \right) \left(\mathbf{1} - \frac{\mathbf{k}\mathbf{k}}{k^2} \right) : \mathbf{p}_1 \mathbf{p}_1 \\
&\quad \frac{\sin^4\left(\frac{\pi}{2} \mathbf{k} \cdot \mathbf{p}_1\right)}{(\mathbf{k} \cdot \mathbf{p}_1)^2}.
\end{aligned} \tag{3.10}$$

The behavior of the tracer falls into two distinct regimes depending on the fluid velocity correlation time, which is $O(\tau)$ for $U\tau/L \ll 1$ and $O(L/U)$ for $U\tau/L \gg 1$. For times much shorter than the velocity correlation time, the tracer shows ballistic motion and the MSD simplifies to,

$$\begin{aligned}
\langle x^2(t) \rangle|_{uncorr} &= \frac{t^2}{2} \langle \hat{\mathbf{u}}(\mathbf{k}, t) \cdot \hat{\mathbf{u}}(-\mathbf{k}, t) \rangle|_{uncorr} \\
&= \frac{nL^3}{(\ln \kappa)^2 32\pi^7} \left[\int d\mathbf{p}_1 \int \frac{d\mathbf{k}}{k^4} \left(\mathbf{1} - \frac{\mathbf{k}\mathbf{k}}{k^2} \right) : \mathbf{p}_1 \mathbf{p}_1 \frac{\sin^4\left(\frac{\pi}{2} \mathbf{k} \cdot \mathbf{p}_1\right)}{(\mathbf{k} \cdot \mathbf{p}_1)^2} \right] t^2.
\end{aligned} \tag{3.11}$$

The term within the brackets can be identified as the fluid velocity variance and hence the magnitude of the MSD in the ballistic regime is hence set by the fluid velocity variance. On the other hand for times much longer than the velocity correlation time, the tracer shows diffusive motion with $\langle x^2(t) \rangle|_{uncorr} = D_t|_{uncorr} t$, where the effective diffusivity is given by,

$$D_t|_{uncorr} = \frac{nL^3}{(\ln \kappa)^2 16\pi^7} \int d\mathbf{p}_1 \int \frac{d\mathbf{k}}{k^4} \left(\frac{1}{2\pi i \mathbf{k} \cdot \mathbf{p}_1 \frac{U\tau}{L} + 1} \right) \left(\mathbf{1} - \frac{\mathbf{k}\mathbf{k}}{k^2} \right) : \mathbf{p}_1 \mathbf{p}_1 \frac{\sin^4\left(\frac{\pi}{2} \mathbf{k} \cdot \mathbf{p}_1\right)}{(\mathbf{k} \cdot \mathbf{p}_1)^2}. \tag{3.12}$$

The diffusivity may also be derived directly using the Green-Kubo formula [Balakrishnan, 2008] and has also been obtained by Kasyap et al. [2014] using a different approach. On the other hand, to the best of our knowledge, the complete expression for the MSD in (3.10) has not been given in the literature even for non-interacting swimmers. The integrals in (3.10) may be numerically evaluated with the choice of a \mathbf{k} -aligned spherical coordinate system.

3.2.2 Suspensions of interacting swimmers

For interacting swimmers, the Fourier-transformed velocity correlation function at $O((nL^3)^2)$ is given by

$$\langle \hat{\mathbf{u}}(\mathbf{k}, t_1) \cdot \hat{\mathbf{u}}(-\mathbf{k}, t_2) \rangle|_{corr} = \int d\mathbf{p}_1 d\mathbf{p}'_1 d\mathbf{p}_2 d\mathbf{p}'_2, \quad \hat{\mathbf{u}}(\mathbf{k}) \cdot \hat{\mathbf{u}}(-\mathbf{k}) \hat{G}_2(\mathbf{p}_1, \mathbf{p}_2, t_1 | \mathbf{p}'_1, \mathbf{p}'_2, t_2; \mathbf{k}) \hat{\Omega}_2^{(1)}(\mathbf{k}, \mathbf{p}'_1, \mathbf{p}'_2) \quad (3.13)$$

where $\hat{\Omega}_2^{(1)}$ is the correlated component of the Fourier transformed pair probability density, $\hat{\Omega}_2^{(1)}$ is $O(nL^3)^2 / \log \kappa$. It was derived by Nambiar [2020] and is given as,

$$\hat{\Omega}_2^{(1)} = \frac{3(nL^3)^2}{32\pi^5 k^2} \left(\frac{U\tau}{L} \right) \left(\frac{1}{\pi i (U\tau/L) \mathbf{k} \cdot (\mathbf{p}_2 - \mathbf{p}_1) + 1} \right) (\mathbf{1} - \hat{\mathbf{k}}\hat{\mathbf{k}}) : \mathbf{p}_2 \mathbf{p}_1 \left[\frac{1}{(\mathbf{k} \cdot \mathbf{p}_1)} \sin^2 \left(\frac{\pi}{2} \mathbf{k} \cdot \mathbf{p}_1 \right) \sin(\pi \mathbf{k} \cdot \mathbf{p}_2) + \frac{1}{(\mathbf{k} \cdot \mathbf{p}_2)} \sin^2 \left(\frac{\pi}{2} \mathbf{k} \cdot \mathbf{p}_2 \right) \sin(\pi \mathbf{k} \cdot \mathbf{p}_1) \right]. \quad (3.14)$$

\hat{G}_2 gives the Fourier transformed transition probability of finding a pair of swimmers with orientations \mathbf{p}_1 and \mathbf{p}_2 at time t_1 , starting with the same pair of swimmers with orientations \mathbf{p}'_1 and \mathbf{p}'_2 at time t_2 . The governing equation for \hat{G}_2 is then same as the equation governing the relaxation of the pair probability density and is given by,

$$\frac{d\hat{G}_2}{dt} + 2\pi i \left(\frac{U\tau}{L} \right) \mathbf{k} \cdot (\mathbf{p}_2 - \mathbf{p}_1) \hat{G}_2 + \left(2\hat{G}_2 - \frac{1}{4\pi} \int d\mathbf{p}_1 \hat{G}_2 - \frac{1}{4\pi} \int d\mathbf{p}_2 \hat{G}_2 \right) = \boldsymbol{\delta}(\mathbf{p}_2 - \mathbf{p}'_2) \boldsymbol{\delta}(\mathbf{p}_1 - \mathbf{p}'_1) \delta(t - t'). \quad (3.15)$$

Similar to the case in section 3.2.1, the inverse tumbling terms in (3.15) again don't contribute, and the expression for \hat{G}_2 relevant to the evaluation of the velocity correlation function, is given by,

$$\hat{G}_2(\mathbf{p}_1, \mathbf{p}_2, t | \mathbf{p}'_1, \mathbf{p}'_2, 0; \mathbf{k}) = \delta(\mathbf{p}_1 - \mathbf{p}'_1) \delta(\mathbf{p}_2 - \mathbf{p}'_2) \exp \left(\left(-2\pi i \mathbf{k} \cdot (\mathbf{p}_2 - \mathbf{p}_1) \frac{U\tau}{L} - 2 \right) t \right). \quad (3.16)$$

Using this result and simplifying, we obtain the final expression for the MSD of a passive tracer at $O((nL^3)^2)$ as

$$\begin{aligned}
\langle x^2(t) \rangle|_{corr} &= \frac{1}{(\ln \kappa)^3 4\pi^6} \int d\mathbf{p}_1 \int d\mathbf{p}_2 \int \frac{d\mathbf{k}}{k^4} \left(\frac{-1 + \exp\left(\left(-2\pi i \mathbf{k} \cdot (\mathbf{p}_2 - \mathbf{p}_1) \frac{U\tau}{L} - 2\right)t\right)}{\left(2\pi i \mathbf{k} \cdot (\mathbf{p}_2 - \mathbf{p}_1) \frac{U\tau}{L} + 2\right)^2} \right) \\
&\quad \left(\mathbf{1} - \frac{\mathbf{k}\mathbf{k}}{k^2} \right) : \mathbf{p}_1 \mathbf{p}_2 \frac{\sin^2\left(\frac{\pi}{2} \mathbf{k} \cdot \mathbf{p}_1\right)}{(\mathbf{k} \cdot \mathbf{p}_1)} \frac{\sin^2\left(\frac{\pi}{2} \mathbf{k} \cdot \mathbf{p}_2\right)}{(\mathbf{k} \cdot \mathbf{p}_2)} \hat{\Omega}_2^{(1)}(\mathbf{p}_1, \mathbf{p}_2; \mathbf{k}) \\
&+ \frac{1}{(\ln \kappa)^3 4\pi^6} t \int d\mathbf{p}_1 \int d\mathbf{p}_2 \int \frac{d\mathbf{k}}{k^4} \left(\frac{1}{2\pi i \mathbf{k} \cdot (\mathbf{p}_2 - \mathbf{p}_1) \frac{U\tau}{L} + 2} \right) \\
&\quad \left(\mathbf{1} - \frac{\mathbf{k}\mathbf{k}}{k^2} \right) : \mathbf{p}_1 \mathbf{p}_2 \frac{\sin^2\left(\frac{\pi}{2} \mathbf{k} \cdot \mathbf{p}_1\right)}{(\mathbf{k} \cdot \mathbf{p}_1)} \frac{\sin^2\left(\frac{\pi}{2} \mathbf{k} \cdot \mathbf{p}_2\right)}{(\mathbf{k} \cdot \mathbf{p}_2)} \hat{\Omega}_2^{(1)}(\mathbf{p}_1, \mathbf{p}_2; \mathbf{k}).
\end{aligned} \tag{3.17}$$

At times much shorter than the velocity correlation time, the tracer shows ballistic motion and the MSD simplifies to,

$$\begin{aligned}
\langle x^2(t) \rangle|_{corr} &= \frac{t^2}{2} \langle \hat{\mathbf{u}}(\mathbf{k}, t) \cdot \hat{\mathbf{u}}(-\mathbf{k}, t) \rangle|_{corr} \\
&= \frac{t^2}{(\ln \kappa)^3 8\pi^6} \int d\mathbf{p}_1 \int d\mathbf{p}_2 \int \frac{d\mathbf{k}}{k^4} \left(\mathbf{1} - \frac{\mathbf{k}\mathbf{k}}{k^2} \right) : \mathbf{p}_1 \mathbf{p}_2 \\
&\quad \frac{\sin^2\left(\frac{\pi}{2} \mathbf{k} \cdot \mathbf{p}_1\right)}{(\mathbf{k} \cdot \mathbf{p}_1)} \frac{\sin^2\left(\frac{\pi}{2} \mathbf{k} \cdot \mathbf{p}_2\right)}{(\mathbf{k} \cdot \mathbf{p}_2)} \hat{\Omega}_2^{(1)}(\mathbf{k}, \mathbf{p}_1, \mathbf{p}_2).
\end{aligned} \tag{3.18}$$

The magnitude of the MSD in the ballistic regime is again set by the fluid velocity variance. On the other hand, for times much longer than the velocity correlation time, the tracer shows diffusive motion with $\langle x^2(t) \rangle|_{corr} = D_t|_{corr} t$ for any finite swimmer run-length ($U\tau/L$). The effective diffusivity is given by,

$$\begin{aligned}
D_t|_{corr} &= \frac{1}{(\ln \kappa)^3 4\pi^6} \int d\mathbf{p}_1 \int d\mathbf{p}_2 \int \frac{d\mathbf{k}}{k^4} \left(\frac{1}{2\pi i \mathbf{k} \cdot (\mathbf{p}_2 - \mathbf{p}_1) \frac{U\tau}{L} + 2} \right) \left(\mathbf{1} - \frac{\mathbf{k}\mathbf{k}}{k^2} \right) : \mathbf{p}_1 \mathbf{p}_2 \\
&\quad \frac{\sin^2\left(\frac{\pi}{2} \mathbf{k} \cdot \mathbf{p}_1\right)}{(\mathbf{k} \cdot \mathbf{p}_1)} \frac{\sin^2\left(\frac{\pi}{2} \mathbf{k} \cdot \mathbf{p}_2\right)}{(\mathbf{k} \cdot \mathbf{p}_2)} \hat{\Omega}_2^{(1)}(\mathbf{k}, \mathbf{p}_1, \mathbf{p}_2).
\end{aligned} \tag{3.19}$$

The integrals in (3.17) and (3.19) are again evaluated numerically. The total mean-squared displacement of the tracer, to $O(nL^3)^2$, is obtained by combining the expressions in (3.10) and (3.17), and is plotted in figure 3.1, as a function of nL^3 , for a suspension of pushers.

Surprisingly, figure 3.1 shows that the time taken to transition from the ballistic to the diffusive regime increases with increasing volume-fraction of the swimmers. This surprising behavior can be explained by noting the differing time scales for the decay of the velocity correlations at $O(nL^3)$ and $O(nL^3)^2$. At $O(nL^3)$, this time-scale (t_c) is set by the swimmer-tracer interaction time. For rapid tumblers ($U\tau/L \ll 1$), the interaction is cut off by the decorrelation of the swimmer orientation, implying $t_c \sim O(\tau)$. On the other hand for straight swimmers ($U\tau/L \gg 1$), the distance that the tracer is convected asymptotes to a finite value for tracer-swimmer separations greater than $O(L)$, and thus $t_c \sim O(L/U)$. At $O(nL^3)^2$, the decay of the velocity correlations, irrespective of $U\tau/L$, only occurs due to orientation decorrelation of the swimmers on the time scale τ . As a result for nL^3 of order unity, the transition time between the ballistic and diffusive regimes diverges as $U\tau/L$. The resulting broad cross-over gives the impression of an nL^3 -dependent anomalous exponent in the interval $L/U \ll t \ll \tau$ (see the curve for $nL^3 = 2.5$ in figure 3.1). For rapid tumblers ($U\tau/L \ll 1$), the transition time is $O(\tau)$ regardless of nL^3 , and there is no intermediate anomalous scaling.

The inset in figure 3.1 shows the $O(nL^3)^2$ correlated contribution to the tracer diffusivity ($D_t|_{corr}$). In the straight-swimmer limit, $D_t|_{corr}$ diverges linearly in $U\tau/L$. This scaling may be rationalized by starting from $D_t \sim U_t^2 t_c$ where U_t is the scale of the velocity convecting the tracer and t_c is the time scale of decay of the velocity correlations. U_t is $O(U/\ln \kappa)$ for (nL^3) of order unity, while the t_c scaling is discussed above. The resulting scaling for tracer diffusivity in an interacting suspension, to $O(nL^3)^2$, is therefore given by,

$$\frac{nL^3 U^2 \tau}{(\ln \kappa)^2} (\tilde{d}_1 + \frac{nL^3 U \tau}{\ln \kappa L} \tilde{d}_2) \quad \text{for } U\tau/L \ll 1, \quad (3.20)$$

and

$$\frac{nL^4 U}{(\ln \kappa)^2} (d_1 + \frac{nL^3 U \tau}{\ln \kappa L} d_2) \quad \text{for } U\tau/L \gg 1. \quad (3.21)$$

and confirms the scalings shown in figure 3.1 (inset) at $O(nL^3)^2$. The tracer diffusivity variation with volume fraction also shows a pusher-puller bifurcation similar to the velocity variance as shown in figure 3.2. Such behavior has been observed in numerical simulations before [Krishnamurthy and Subramanian, 2015].

Several experiments probing bacterial suspension dynamics with passive tracers have reported an intermediate super-diffusive regime and a volume fraction dependent cross-over time [Argun et al., 2016; Chen et al., 2007a; Kim and Breuer, 2004; Patteson et al., 2016; Peng et al., 2016; Valeriani et al., 2011; Wu and Libchaber, 2000]. Our analysis shows that in a bath of interacting persistent swimmers ($U\tau/L \gg 1$), the temporal and spatial

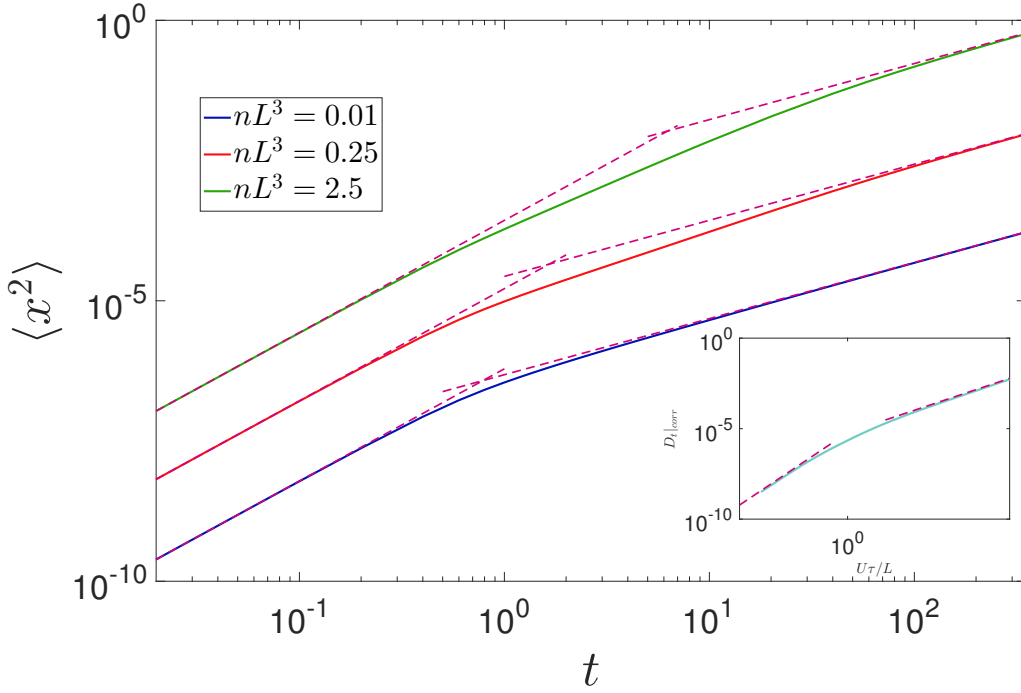


Fig. 3.1 The evolution of the mean-squared displacement of the passive tracer, in a suspension of pushers, with time for $U\tau/L = 50$ and $\kappa = 8$ for varying nL^3 . The inset shows the correlated tracer diffusivity ($D_t|_{corr}$) at $O(nL^3)^2$ as a function of the run-length, $U\tau/L$, for $\kappa = 8$; the dashed lines show the asymptotic scalings discussed in the text.

correlations of the (effective) noise experienced by the passive tracer increase to $O(\tau)$ and $O(U\tau)$ respectively. The simplistic approximation for the active noise often found in the literature is thus seen to be insufficient [Argun et al., 2016; Kanazawa et al., 2020; Maggi et al., 2014].

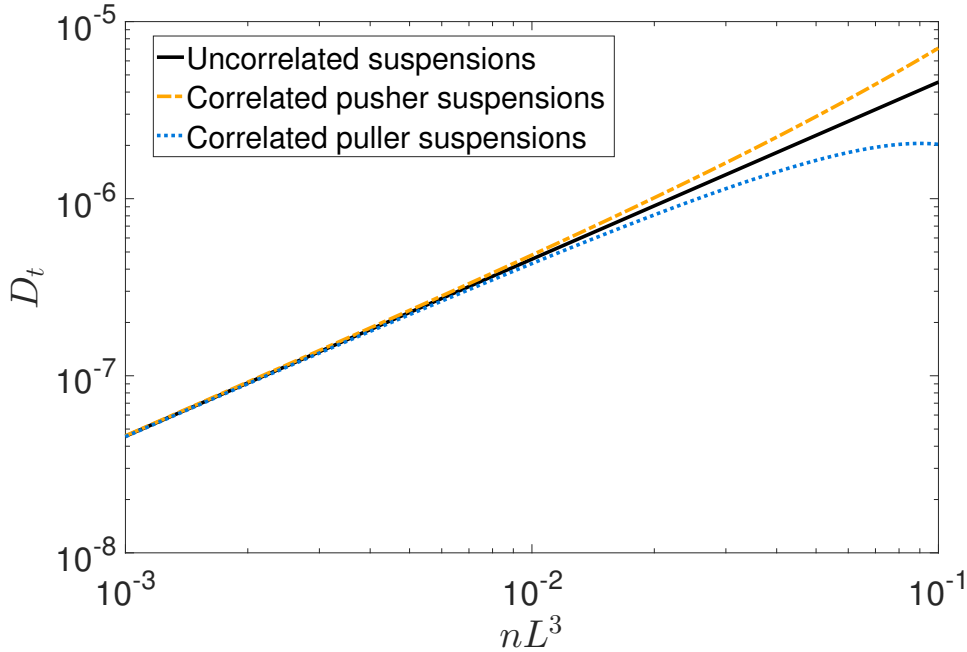


Fig. 3.2 The variation of the diffusivity of a passive tracer versus the volume fraction of swimmers (nL^3) for a fixed run-length $U\tau/L = 50$ and aspect-ratio $\kappa = 8$.

3.3 Correlations near the collective motion threshold

Closer to the collective motion threshold, the correlations induced by the fluctuating suspension velocity field are expected to become important. Thus, we need to use a stochastic equation to theoretically examine the same. Stochastic partial differential equations are used in analysing correlations near equilibrium phase transitions [Chaikin and Lubensky, 2000]; their active analogs have been used more recently in examining non-equilibrium transitions in active suspensions [Cates, 2019; Cates and Tjhung, 2018; Tiribocchi et al., 2015]. We develop a similar theory for a dilute bacterial suspension in this section by accounting for the fluctuating flow induced by long-ranged hydrodynamic interactions between the bacteria. Here, the mean-field interaction between all the bacteria is accounted for by introducing an active stress field, which drives the fluctuating flow. This is in contrast to the correlations examined in the previous section, which relied on pairwise interactions between the bacteria.

First, section 3.3.1 discusses the governing stochastic integro-differential equation and section 3.3.2 derives the correlations for the associated noise. Next, section 3.3.3 and section 3.3.4 discuss the solution to this stochastic equation and then derive a theoretical expression for the phase space density correlation function; the analysis in 3.3.3 closely follows the method outlined in Chapter 2. Finally, section 3.3.5 discusses the results for

various correlations as the threshold for collective motion is approached. Specifically, we examine the velocity variance and co-variance, the tracer diffusivity and the nematic orientation correlations.

3.3.1 Stochastic run-and-tumble Operator for interacting bacteria

Consider a bath of bacteria, with volume fraction nL^3 , where n is the number of bacteria per unit volume and L the length of a bacterium. Each bacterium swims with a speed U (the run event), until it randomly reorients by a finite amount (the tumble event). The tumbles are assumed to obey Poissonian statistics with an average rate (τ). The bacteria induces a long-ranged fluid flow as it swims, which in turn convects and rotates the other bacteria. The bath is characterized by the orientation-position density for the bacteria ($\Omega(\mathbf{x}, \mathbf{p}, t)$) and the associated velocity field (\mathbf{u}). The stochastic equation governing the phase space density Ω is given by,

$$\frac{\partial \Omega}{\partial t} + (U\mathbf{p} + \mathbf{u}) \cdot \nabla_{\mathbf{x}} \Omega + \nabla_{\mathbf{p}} \cdot (\dot{\mathbf{p}} \Omega) + \frac{1}{\tau} \left(\Omega - \frac{1}{4\pi} \int \Omega(\mathbf{p}', t) d\mathbf{p}' \right) = \eta(\mathbf{x}, \mathbf{p}, t), \quad (3.22)$$

where the left hand side represents the deterministic evolution and the right hand side is the noise term ($\eta(\mathbf{x}, \mathbf{p}, t)$), and we have assumed random tumbles. The deterministic evolution is governed by convection due to swimming ($U\mathbf{p}$) and the suspension velocity field (\mathbf{u}) interspersed with random decorrelating tumbles. The suspension velocity field (\mathbf{u}), which is governed by the Stokes equations with an additional active stress ($\boldsymbol{\Sigma}^a$) due to the swimming motion,

$$-\nabla P + \mu \nabla^2 \mathbf{u} = \nabla \cdot \boldsymbol{\Sigma}^a, \quad (3.23)$$

where P is the suspension pressure and μ the viscosity of the suspending fluid. A bacterium can be efficiently modeled as a slender fiber with a given distribution of forces ($\mathbf{f}(s)$). This gives a non-local expression for the stress,

$$\boldsymbol{\Sigma}^a = \frac{1}{2} \int d\mathbf{p} \int_{-L/2}^{L/2} ds \int_{-L/2}^s d\hat{s} \Omega(\mathbf{x} - s\mathbf{p}, \mathbf{p}) (\mathbf{f}(\hat{s})\mathbf{p} + \mathbf{p}\mathbf{f}(\hat{s})), \quad (3.24)$$

with $\mathbf{f}(s) = \mathcal{D} \mu U \text{sgn}(s) / (\log(\kappa)) \mathbf{p}$, where κ is the bacterium aspect ratio. Note that \mathcal{D} distinguishes whether the swimmer is a pusher or a puller; for a force-free pusher $\mathcal{D} = 1$, while for a puller $\mathcal{D} = -1$. Recall that bacteria are pushers so we will set $\mathcal{D} = 1$ for the analysis of bacterial suspensions in this chapter, but our formalism would also allow us to easily study pullers.

The governing equations (3.22)-(3.23) should be interpreted in the usual sense of stochastic field theories, such as the classical Model H that is used to study phase transitions in systems with conserved density and associated fluid flow [Chaikin and Lubensky, 2000]. The correlations of the noise term in (3.22) are examined in the next section.

3.3.2 Noise Correlations for the Run-And-Tumble Operator

The swimming of the bacteria implies that time-reversal symmetry is broken at the micro-scale in a bacterial bath. Thus, we cannot appeal to a fluctuation-dissipation theorem to derive the noise correlations as is usually done in stochastic field theories describing equilibrium critical phenomena [Cates, 2019; Chaikin and Lubensky, 2000; Täuber, 2014]. Instead, we start from the phase space density (Ω) which is defined as,

$$\Omega = \sum_{i=1}^N \delta(\mathbf{x} - \mathbf{x}_i(t)) \delta(\mathbf{p} - \mathbf{p}_i) \quad (3.25)$$

in a bacterial bath with N bacteria. The equation governing the evolution of the phase space density can be written in a difference form as,

$$\Delta\Omega + \Delta t((U\mathbf{p} + \mathbf{u}) \cdot \nabla_{\mathbf{x}}\Omega + \nabla_{\mathbf{p}} \cdot (\dot{\mathbf{p}}\Omega)) = \sum_{i=1}^N q_i(-\delta(\mathbf{p} - \mathbf{p}_i(t)) + \delta(\mathbf{p} - \hat{\mathbf{p}}_i)) \delta(\mathbf{x} - \mathbf{x}_i(t)), \quad (3.26)$$

where $\Delta\Omega = \Omega(\mathbf{x}, \mathbf{p}, t + \Delta t) - \Omega(\mathbf{x}, \mathbf{p}, t)$. The RHS of (3.26) denotes the terms associated with the spatially localized tumbling events for each of the N -bacterium. Here $\mathbf{p}_i(t)$ and $\hat{\mathbf{p}}_i$ are the pre- and post-tumble orientations, respectively, of the i -th bacterium, and q_i are identical, independent Poisson-distributed random variables with mean $\langle q_i \rangle = \Delta t / \tau$ and variance $(\langle q_i - \langle q_i \rangle \rangle)^2 = \Delta t / \tau$ [Van Kampen, 1992]. Taking the continuum ($\Delta t \rightarrow 0$) limit, and subtracting out the mean of the tumbling terms on both sides, we obtain,

$$\begin{aligned} \frac{\partial \Omega}{\partial t} + (U\mathbf{p} + \mathbf{u}) \cdot \nabla_{\mathbf{x}}\Omega + \nabla_{\mathbf{p}} \cdot (\dot{\mathbf{p}}\Omega) + \sum_{i=1}^N \frac{\langle q_i \rangle}{\Delta t} (\delta(\mathbf{x} - \mathbf{x}_i(t)) \delta(\mathbf{p} - \mathbf{p}_i(t)) \\ + \delta(\mathbf{x} - \mathbf{x}_i(t)) \langle \delta(\mathbf{p} - \hat{\mathbf{p}}_i) \rangle) = \eta(\mathbf{x}, \mathbf{p}, t), \end{aligned} \quad (3.27)$$

with the exact expression for the noise being given by,

$$\begin{aligned} \eta(\mathbf{x}, \mathbf{p}, t) = \lim_{\Delta t \rightarrow 0} & \left[\sum_{i=1}^N \frac{q_i - \langle q_i \rangle}{\Delta t} (-\delta(\mathbf{p} - \mathbf{p}_i(t)) + \delta(\mathbf{p} - \hat{\mathbf{p}}_i)) \right. \\ & \left. + \sum_{i=1}^N \frac{\langle q_i \rangle}{\Delta t} \left(\frac{1}{4\pi} - \delta(\mathbf{p} - \hat{\mathbf{p}}_i) \right) \delta(\mathbf{x} - \mathbf{x}_i(t)) \right]. \end{aligned} \quad (3.28)$$

Upon rearranging and using the definition of Ω , (3.27) reduces to the expected continuum form,

$$\frac{\partial \Omega}{\partial t} + (U\mathbf{p} + \mathbf{u}) \cdot \nabla_{\mathbf{x}} \Omega + \nabla_{\mathbf{p}} \cdot (\dot{\mathbf{p}} \Omega) + \frac{1}{\tau} \left(\Omega - \int \Omega(\mathbf{p}', t) d\mathbf{p}' \right) = \eta(\mathbf{x}, \mathbf{p}, t), \quad (3.29)$$

which was stated in the previous section. From (3.28) it is easy to see that $\langle \eta(\mathbf{x}, \mathbf{p}, t) \rangle = 0$ as expected. The pair correlations of the noise can be further calculated as,

$$\langle \eta(\mathbf{x}, \mathbf{p}, t), \eta(\mathbf{x}', \mathbf{p}', t') \rangle = \frac{1}{\tau} \delta(\mathbf{x} - \mathbf{x}') \delta(t - t') \left[\delta(\mathbf{p} - \mathbf{p}') - \frac{1}{4\pi} \right] \langle \Omega(\mathbf{x}, \mathbf{p}, t) + \Omega(\mathbf{x}, \mathbf{p}', t) \rangle. \quad (3.30)$$

where the presence of $\delta(\mathbf{x} - \mathbf{x}')$ indicates that tumbling conserves locally the number of bacterium. Thus, it does not induce any direct position-space correlations and is easily seen from (3.30) as,

$$\int \int \langle \eta(\mathbf{x}, \mathbf{p}, t), \eta(\mathbf{x}', \mathbf{p}', t') \rangle d\mathbf{p} d\mathbf{p}' = 0. \quad (3.31)$$

Since the run-and-tumble process is Poissonian and not Gaussian, we expect higher moments of the noise to not be dependent on just the second moment [Gardiner et al., 1985]. This has been shown earlier in the context of the the non-linear stochastic Boltzmann-equation [Ueyama, 1980]. Further note that (3.30) implies a multiplicative-noise interpretation, similar to the Langevin equation for interacting Brownian particles [Dean, 1996] as well as the stochastic Boltzmann-equation [Ueyama, 1980]. However, in this chapter we are only considered with correlations that develop in a homogeneous isotropic swimmer suspension with approach towards the collective motion threshold, and as we will see below, the noise correlations simplify in this limit.

3.3.3 Solving the interacting Run-And-Tumble Operator

We look for small amplitude fluctuations about the homogeneous, isotropic mean state ($n/4\pi$) such that $\Omega = \frac{n}{4\pi} + \Omega'$. To solve for the fluctuating phase space density Ω' , we transform to

Fourier space where

$$\tilde{\Omega}(\mathbf{k}, \mathbf{p}) = \int \Omega' e^{-2\pi i \mathbf{k} \cdot \mathbf{x}} d\mathbf{x}, \quad (3.32)$$

and similarly for the suspension velocity,

$$\tilde{\mathbf{u}}(\mathbf{k}) = \int \mathbf{u}' e^{-2\pi i \mathbf{k} \cdot \mathbf{x}} d\mathbf{x}. \quad (3.33)$$

Upon linearizing (3.22) we obtain the following governing equation, in Fourier space, for the fluctuating phase space density,

$$\frac{\partial \tilde{\Omega}}{\partial t} + 2\pi i \mathbf{k} \cdot \mathbf{p} U \tilde{\Omega} + \frac{1}{\tau} \left(\tilde{\Omega} - \frac{1}{4\pi} \int \tilde{\Omega} d\mathbf{p} \right) + \frac{n}{4\pi} \nabla_{\mathbf{p}} \cdot \tilde{\mathbf{p}} = \tilde{\eta}(\mathbf{k}, \mathbf{p}, t), \quad (3.34)$$

where $\tilde{\mathbf{p}}$ is the Fourier transformed $\dot{\mathbf{p}}$, which denotes the rotation of the bacteria by the fluctuating velocity gradient. For a slender-body it is given by [Subramanian and Koch, 2009],

$$\dot{\mathbf{p}} = \frac{3}{2L^3} \int_{-L/2}^{L/2} s ds (\boldsymbol{\delta} - \mathbf{p}\mathbf{p}) \cdot \mathbf{u}'(\mathbf{x} + s\mathbf{p}), \quad (3.35)$$

and

$$\tilde{\mathbf{p}} = \int \dot{\mathbf{p}} e^{-2\pi i \mathbf{k} \cdot \mathbf{x}} d\mathbf{x}. \quad (3.36)$$

Inverting the Stokes equation in Fourier space and simplifying the active stress finally yields, for the fluctuating velocity field,

$$\tilde{\mathbf{u}}(\mathbf{k}, t) = \mathcal{D} \frac{U}{\log(\kappa)} \frac{i}{2\pi^3 k^2} \int d\mathbf{p} \tilde{\Omega}(\mathbf{k}, \mathbf{p}, t) \frac{1}{\mathbf{k} \cdot \mathbf{p}} \sin^2\left(\pi \frac{(\mathbf{k} \cdot \mathbf{p})L}{2}\right) (\boldsymbol{\delta} - \hat{\mathbf{k}}\hat{\mathbf{k}}) \cdot \mathbf{p}. \quad (3.37)$$

Using the above two expressions in (3.34) and simplifying finally leads to a integro-differential equation for $\tilde{\Omega}$. Omitting the intermediate steps, we finally obtain,

$$\begin{aligned} \frac{\partial \tilde{\Omega}}{\partial t} + 2\pi i \mathbf{k} \cdot \mathbf{p} U \tilde{\Omega} + \frac{1}{\tau} \left(\tilde{\Omega} - \frac{1}{4\pi} \int \tilde{\Omega} d\mathbf{p} \right) + \\ \frac{3n\mathcal{D}U}{32\pi^4 k^2 L \log(\kappa)} \int \tilde{\Omega}(\mathbf{p}') d\mathbf{p}' (\boldsymbol{\delta} - \hat{\mathbf{k}}\hat{\mathbf{k}}) : \mathbf{p}\mathbf{p}' \frac{(\sin^2(\pi(L/2)(\mathbf{k} \cdot \mathbf{p}')))(\sin(\pi L \mathbf{k} \cdot \mathbf{p}))}{(\mathbf{k} \cdot \mathbf{p}')} = \tilde{\eta}(\mathbf{k}, \mathbf{p}, t). \end{aligned} \quad (3.38)$$

Using $\langle \Omega(\mathbf{k}, \mathbf{p}, t) \rangle = n/4\pi$, the noise correlations in Fourier space reduce to

$$\langle \tilde{\eta}(\mathbf{k}, \mathbf{p}, t), \tilde{\eta}(\mathbf{k}', \mathbf{p}', t') \rangle = \frac{2n}{4\pi\tau} \delta(\mathbf{k} + \mathbf{k}') \delta(t - t') \left(\delta(\mathbf{p} - \mathbf{p}') - \frac{1}{4\pi} \right). \quad (3.39)$$

Note that the noise becomes additive for the homogeneous isotropic state. Using the Green's function expression, the solution for (3.38) is given as,

$$\tilde{\Omega}(\mathbf{k}, \mathbf{p}, t) = \int_0^t ds \int d\bar{\mathbf{p}} G(\mathbf{k}, \mathbf{p}, t | \bar{\mathbf{p}}, s) \tilde{\eta}(\mathbf{k}, \bar{\mathbf{p}}, s), \quad (3.40)$$

where the Green's function ($G(\mathbf{k}, \mathbf{p}, t)$) must satisfy the homogeneous equation,

$$\begin{aligned} \frac{\partial G}{\partial t} + 2\pi i \mathbf{k} \cdot \mathbf{p} U G + \frac{1}{\tau} \left(G - \frac{1}{4\pi} \int G d\mathbf{p} \right) + \\ \frac{3n\mathcal{D}U}{32\pi^4 k^2 L \log(\kappa)} \int G(\mathbf{p}') d\mathbf{p}' (\boldsymbol{\delta} - \hat{\mathbf{k}}\hat{\mathbf{k}}) : \mathbf{p}\mathbf{p}' \frac{(\sin^2(\pi(L/2)(\mathbf{k} \cdot \mathbf{p}')))(\sin(\pi L \mathbf{k} \cdot \mathbf{p}))}{(\mathbf{k} \cdot \mathbf{p}')} = 0, \end{aligned} \quad (3.41)$$

with the initial condition $G(\mathbf{k}, \mathbf{p}, 0) = \delta(\mathbf{p} - \bar{\mathbf{p}})$. Note that in (3.41) the last term on the left hand side arises from coupling of the fluid flow with the equations of motion for the bacterium. We choose the following wavevector-aligned co-ordinate system to further simplify things,

$$\mathbf{p} = \cos \theta \hat{\mathbf{k}} + \sin \theta \sin \phi \hat{\mathbf{m}} + \sin \theta \cos \phi \frac{\hat{\mathbf{u}}}{|\hat{\mathbf{u}}|}, \quad (3.42)$$

along with using $\mu = \cos \theta$ in what follows. We can then expand

$$G = \mathcal{G}^0 + \sum_{m=1}^{\infty} \mathcal{G}^m \cos m\phi, \quad (3.43)$$

where we can neglect the $\sin m\phi$ terms without loss of generality due to the nature of the inhomogeneous terms in (3.41). For \mathcal{G}^0 , we obtain the equation,

$$\frac{\partial \mathcal{G}^0}{\partial t} + 2\pi i k \mu \mathcal{G}^0 + \frac{L}{U\tau} \left(\mathcal{G}^0 - \frac{1}{2} \int \mathcal{G}^0 d\mu \right) = 0, \quad (3.44)$$

with the initial condition $\partial \mathcal{G}^0(k, 0) = 1$. We see that for axisymmetric modes, the contribution of the mean flow field drops out and thus \mathcal{G}^0 describes the evolution of independent concentration modes as seen in Chapter 2.

For \mathcal{G}^1 , we obtain the equation,

$$\frac{\partial \mathcal{G}^1}{\partial t} + 2\pi i k \mu \mathcal{G}^1 + \frac{L}{U\tau} \mathcal{G}^1 = \frac{-3nL^3 \mathcal{D}}{\log \kappa 32\pi^3 k^3} \sin(\pi k \mu) (1 - \mu^2)^{1/2} \int \frac{d\mu'}{\mu'} \mathcal{G}^1 (1 - (\mu')^2)^{1/2} \sin^2\left(\frac{\pi k \mu'}{2}\right), \quad (3.45)$$

with the initial condition $\partial \mathcal{G}^1(k, 0) = \cos(\phi - \bar{\phi})$. We thus see that the relevance of the fluid velocity comes in only the non-axisymmetric mode $m = 1$. It is easily seen that the final term

in (3.41) does not contribute to any higher modes ($m \geq 2$). Thus, the expressions for \mathcal{G}^0 and \mathcal{G}^m ($m \geq 2$) remain identical to those already obtained in Chapter 2. One only has to solve (3.45) to obtain \mathcal{G}^1 . This may again be done along the lines of Chapter 2 by first solving for the corresponding eigenfunctions and writing \mathcal{G}^1 as a bilinear superposition of the direct and adjoint eigenfunctions.

$$\mathcal{G}^1(\lambda, t | \lambda', 0) = \int \Phi_{cs}^1(\lambda; \lambda_0) \tilde{\Phi}_{cs}^1(\lambda_0; \lambda') e^{\lambda_0 t} d\lambda_0 + \sum_n \Phi_d^1(\lambda; \lambda_n) \tilde{\Phi}_d^1(\lambda_n; \lambda') e^{\lambda_n t}, \quad (3.46)$$

Both the discrete and continuous spectrum eigenfunctions and the adjoints are obtained exactly in the same manner as that in Chapter 2. While it is possible to derive the analytical form of the eigenfunctions for (3.45) exactly, it is not possible to obtain the associated phase space density correlation function analytically. Thus, here we have to make a further simplification to make analytical progress which corresponds to assuming the bacterium length to be much smaller than the wavelength of the fluid velocity fluctuations, which in turn are constructed from a superposition of the aforementioned eigenfunctions. The bacteria appear as dipoles on the length scales relevant to the suspension velocity and is equivalent to using the approximation $\sin \pi k \mu \approx \pi k \mu$ in (3.45), which leads to the following simplified equation,

$$\frac{\partial \mathcal{G}^1}{\partial t} + 2\pi i k \mu \mathcal{G}^1 + \frac{L}{U \tau} \mathcal{G}^1 = \frac{-3nL^3 \mathcal{D}}{\log \kappa 128} \mu (1 - \mu^2)^{1/2} \int \frac{d\mu'}{\mu'} \mathcal{G}^1 (1 - (\mu')^2)^{1/2} \mu'. \quad (3.47)$$

The detailed derivation of the eigenfunction and eigenvalues associated with \mathcal{G}^1 in (3.47) is exactly the same as that in Chapter 2, and thus the details are omitted here. The method of obtaining the adjoints also follows the same steps as the previous chapter. The final forms of the various eigenfunctions are given below, and these are used to derive analytic expressions for the correlations. The dynamic discrete mode eigenfunction is,

$$\Phi_d^1 = \frac{\mu(1 - \mu^2)^{1/2}}{\mu - \mu_d}, \quad (3.48)$$

with the associated adjoint,

$$\tilde{\Phi}_d^1 = \frac{\mu'(1 - (\mu')^2)^{1/2}}{\mu' - \mu_d} \left(\int d\mu \frac{\mu^2(1 - \mu^2)}{\mu - \mu_d} \right)^{-1} \quad (3.49)$$

Upon solving the dispersion relation for μ_d , we find that there are two separate discrete modes, and one of the eigenvalues crosses zero upon increasing $nL^2 U \tau$, which marks the onset of collective motion. This result was originally derived by [Subramanian and Koch](#)

[2009] and further studied in Subramanian et al. [2011], and thus we omit the details of the eigenvalues here. The continuous spectrum eigenfunction is given by,

$$\Phi_{cs}^1 = \left[1 - C \int_{-1}^1 \frac{(\mu')^2(1 - (\mu')^2)}{\mu' - \mu_0} d\mu' \right] \delta(\mu - \mu_0) + C \frac{\mu \mu_0 (1 - \mu^2)^{1/2} (1 - \mu_0^2)^{1/2}}{\mu - \mu_0}, \quad (3.50)$$

where one sees the same overall structure as the CS eigenfunctions in Chapter 2 in terms of a Dirac delta function and a PV-singular non-local contribution. In (3.50),

$$C = \frac{3nL^3 i \mathcal{D}}{256\pi k \log(\kappa)}. \quad (3.51)$$

The continuous spectrum eigenvalue is given by $\sigma = -\frac{L}{U\tau} - 2\pi i k \mu_0$ with $\mu_0 \in [-1, 1]$. For the dipole approximation, the functional form of the adjoint is identical to that of the CS-eigenfunction, to within a normalisation constant ($D(\mu_0)$). This is of crucial importance in a simplification in the next section when deriving the analytical form of the phase space density correlation function. Note that the exact analytical form of the adjoint is not needed for deriving the phase space density correlation function in the next section, and this omitted here, but the same is analytically obtained by following the exact steps outlined in Chapter 2.

To summarise, we see that the eigenspectrum of the full operator consists of three classes of modes. First, the kinematic discrete mode which carries the concentration fluctuations in a non-interacting suspension and is associated with the axisymmetric mode. Second, the dynamic discrete modes only arise due to the bath velocity coupling for the mode $m = 1$. Finally, the continuous spectrum which arises due to swimming (see Chapter 2 for details) and exists for all m . Note that the CS-eigenfunctions for $m = 0$ and $m = 2$ are identical to those in Chapter 2, but that those for $m = 1$ are different as seen above.

3.3.4 Phase Space Density Correlation Function

Using the Green's function expression, the solution for (3.34) is given as,

$$\tilde{\Omega}(\mathbf{k}, \mathbf{p}, t) = \int_0^t ds \int d\bar{\mathbf{p}} G(\mathbf{k}, \mathbf{p}, t | \bar{\mathbf{p}}, s) \tilde{\eta}(\mathbf{k}, \bar{\mathbf{p}}, s). \quad (3.52)$$

The phase space density correlation function is then given by,

$$\begin{aligned} \langle \tilde{\Omega}(\mathbf{k}, \mathbf{p}, t) \tilde{\Omega}(\mathbf{k}', \mathbf{p}', t') \rangle &= \int_0^t \int_0^{t'} ds ds' \int \int d\bar{\mathbf{p}} d\bar{\mathbf{p}}' G(\mathbf{k}, \mathbf{p}, t | \bar{\mathbf{p}}, s) G(\mathbf{k}', \mathbf{p}', t' | \bar{\mathbf{p}}', s') \\ &\quad \langle \tilde{\eta}(\mathbf{k}, \bar{\mathbf{p}}, s) \tilde{\eta}(\mathbf{k}', \bar{\mathbf{p}}', s') \rangle. \end{aligned} \quad (3.53)$$

Using the noise-correlations given in (3.39), we get,

$$\begin{aligned} \langle \tilde{\Omega}(\mathbf{k}, \mathbf{p}, t) \tilde{\Omega}(\mathbf{k}', \mathbf{p}', t') \rangle &= \frac{2n}{4\pi\tau} \delta(\mathbf{k} + \mathbf{k}') \int_0^t \int_0^{t'} ds ds' \delta(s - s') \\ &\quad \int \int d\bar{\mathbf{p}} d\bar{\mathbf{p}}' G(\mathbf{k}, \mathbf{p}, t | \bar{\mathbf{p}}, s) G(\mathbf{k}', \mathbf{p}', t' | \bar{\mathbf{p}}', s') (\delta(\bar{\mathbf{p}} - \bar{\mathbf{p}}') - \frac{1}{4\pi}), \end{aligned} \quad (3.54)$$

where the $\delta(\mathbf{k} + \mathbf{k}')$ term is a signature of spatial homogeneity of the mean state. Substituting the Green's function expansion in terms of the modes from (3.43), we get,

$$\begin{aligned} \langle \tilde{\Omega}(\mathbf{k}, \mathbf{p}, t) \tilde{\Omega}(\mathbf{k}', \mathbf{p}', t') \rangle &= \frac{2n}{4\pi\tau} \delta(\mathbf{k} + \mathbf{k}') \int_0^t \int_0^{t'} ds ds' \delta(s - s') \\ &\quad \int \int d\bar{\mu} d\bar{\mu}' d\bar{\phi} d\bar{\phi}' \left[\frac{1}{2\pi} \mathcal{G}^0(k, \mu, t | \bar{\mu}, s) + \sum_{m=1}^{\infty} \frac{1}{\pi} \mathcal{G}^m(k, \mu, t | \bar{\mu}, s) \cos(m(\phi - \bar{\phi})) \right] \\ &\quad \left[\frac{1}{2\pi} \mathcal{G}^0(k', \mu', t' | \bar{\mu}', s') + \frac{1}{\pi} \sum_{n=1}^{\infty} \mathcal{G}^n(k', \mu', t' | \bar{\mu}', s') \cos(n(\phi' - \bar{\phi}')) \right] \\ &\quad \left(\delta(\bar{\mu} - \bar{\mu}') \delta(\bar{\phi} - \bar{\phi}') - \frac{1}{4\pi} \right). \end{aligned} \quad (3.55)$$

Upon simplifying, we finally arrive at the expression for the phase space density correlation function,

$$\begin{aligned} \langle \tilde{\Omega}(\mathbf{k}, \mathbf{p}, t) \tilde{\Omega}(\mathbf{k}', \mathbf{p}', t') \rangle &= \sum_{m=1}^{\infty} \Omega_2^m(k, \mu, \mu') \cos(m(\phi - \phi')) \\ &= \frac{2n}{4\pi\tau} \delta(\mathbf{k} + \mathbf{k}') \int_0^t \int_0^{t'} ds ds' \delta(s - s') \\ &\quad \left[\frac{1}{\pi} \sum_{m=1}^{\infty} \int d\bar{\mu} \mathcal{G}^m(k, \mu, t | \bar{\mu}, s) \mathcal{G}^m(k', \mu', t' | \bar{\mu}, s') \cos(m(\phi - \phi')) \right. \\ &\quad \left. + \frac{1}{4\pi} \int \int d\bar{\mu} d\bar{\mu}' \mathcal{G}^0(k, \mu, t | \bar{\mu}, s) \mathcal{G}^0(k', \mu', t' | \bar{\mu}', s') (2\delta(\bar{\mu} - \bar{\mu}') - 1) \right], \end{aligned} \quad (3.56)$$

where we have separated out the non-axisymmetric and axisymmetric contributions to the phase space density correlation function. It is clear that the non-axisymmetric modes contribute to orientation and velocity correlations, and the axisymmetric mode to concentration correlations. As we have seen in section 3.3.3, the bath velocity leads to non-trivial dynamics only for the $m = 1$ mode and thus all the non-trivial correlation functions calculated later only depend on the $m = 1$ component. In the rest of the chapter we focus on the same mode

of the phase space density correlation function. Substituting the expression for \mathcal{G}^1 from (3.46) we get,

$$\begin{aligned}
\Omega_2^1(k, \mu, \mu', t, t') &= \frac{2n}{4\pi^2\tau} \int_0^t \int_0^{t'} ds ds' \int d\bar{\mu} \mathcal{G}^1(k, \mu, t | \bar{\mu}, s) \mathcal{G}^1(-k, \mu', t' | \bar{\mu}, s') \\
&= \frac{2n}{4\pi^2\tau} \delta(\mathbf{k} + \mathbf{k}') \int_0^t \int_0^{t'} ds ds' \int d\bar{\mu} \left[d\mu_0 \Phi_{cs}^1(\mu; \mu_0) \tilde{\Phi}_{cs}^1(\mu_0; \bar{\mu}) e^{(-2\pi i k \mu_0 - \frac{1}{\tau})(t-s)} \right. \\
&\quad \left. \int d\mu'_0 \Phi_{cs}^1(\mu'; \mu'_0) \tilde{\Phi}_{cs}^1(\mu'_0; \bar{\mu}) e^{(2\pi i k \mu'_0 - \frac{1}{\tau})(t'-s')} \right. \\
&\quad \left. + \sum_d \Phi_d^1(\mu; \mu_d) \tilde{\Phi}_d^1(\mu_d; \bar{\mu}) \Phi_d^1(\mu'; \mu'_d) \tilde{\Phi}_d^1(\mu'_d; \bar{\mu}) e^{(-2\pi i k \mu_d - \frac{1}{\tau})(t-s)} \right. \\
&\quad \left. e^{(2\pi i k \mu'_d - \frac{1}{\tau})(t'-s')} \right], \tag{3.57}
\end{aligned}$$

where we have used the property that the discrete and CS-spectrum eigenfunctions are orthogonal to each other. Further, the following identity may be proven for the eigenfunctions,

$$\int \tilde{\Phi}_{cs}^1(\mu_0; \bar{\mu}) \tilde{\Phi}_{cs}^1(\mu'_0; \bar{\mu}) d\bar{\mu} = \frac{\delta(\mu_0 - \mu'_0)}{D(\mu_0)}. \tag{3.58}$$

Note that this identity relies on the functional form of the eigenfunction and the adjoint being identical to within a normalisation constant. This simplification only holds for the case of dipoles and not for general slender bodies. Thus, analytical progress past this point requires the additional approximation that we made in the previous section. Using this and carrying out the time integration, we finally arrive at the expression for the phase space density correlation function

$$\begin{aligned}
\Omega_2^1(k, \mu, \mu', t, t') &= \frac{n}{4\pi^2\tau} \delta(\mathbf{k} + \mathbf{k}') \left(e^{-\frac{1}{\tau}(t-t')} - e^{-\frac{1}{\tau}(t+t')} \right) \left[\int d\mu_0 e^{(-2\pi i k \mu_0)(t-t')} \right. \\
&\quad \left. \frac{\Phi_{cs}^1(\mu; \mu_0) \Phi_{cs}^1(\mu'; \mu_0)}{D(\mu_0)} \right. \\
&\quad \left. + \sum_d \left(e^{-(2\pi i k \tau \mu_d + 1)(t+t')(t-t')} - e^{-(2\pi i k \tau \mu_d + 1)(t+t')} \right) \frac{\Phi_d^1(\mu; \mu_d) \tilde{\Phi}_d^1(\mu_d; \bar{\mu})}{2\pi i k \tau \mu_d + 1} \right]. \tag{3.59}
\end{aligned}$$

The steady-state phase space density correlation function is given as,

$$\Omega_2^1(k, \mu, \mu') = \frac{n}{4\pi^2} \delta(\mathbf{k} + \mathbf{k}') \left[\int d\mu_0 \frac{\Phi_{cs}^1(\mu; \mu_0) \Phi_{cs}^1(\mu'; \mu_0)}{D(\mu_0)} + \sum_d \frac{\Phi_d^1(\mu; \mu_d) \tilde{\Phi}_d^1(\mu_d; \bar{\mu})}{2\pi i k \tau \mu_d + 1} \right]. \tag{3.60}$$

Note that the eigenfunctions satisfy the following completeness identity for $m = 1$,

$$\delta(\mu - \mu') = \int d\mu_0 \frac{\Phi_{cs}^1(\mu; \mu_0) \Phi_{cs}^1(\mu'; \mu_0)}{D(\mu_0)} + \sum_d \Phi_d^1(\mu; \mu_d) \tilde{\Phi}_d^1(\mu_d; \bar{\mu}), \quad (3.61)$$

using which we get,

$$\Omega_2^1(k, \mu, \mu') = \frac{n}{4\pi^2} \delta(\mathbf{k} + \mathbf{k}') \left[\delta(\mu - \mu') + \sum_d \Phi_d^1(\mu; \mu_d) \tilde{\Phi}_d^1(\mu_d; \bar{\mu}) \frac{-2\pi i k \tau \mu_d}{2\pi i k \tau \mu_d + 1} \right]. \quad (3.62)$$

The delta-function term in (3.62) represents a lack of orientation correlations for non-interacting swimmers. Thus, we see that the steady-state correlations all project onto the discrete mode. A similar observation was made in the context of Kuramoto-model of coupled oscillators [Hildebrand et al., 2007]. Note that this is only the component corresponding to $m = 1$ of the phase space density correlation function. For $nL^3 \rightarrow 0$, the second term in (3.62) disappears and the $m = 1$ contribution combines with the contributions for other m 's to give the required answer for non-interacting swimmers. We further partition the phase space density correlation function as,

$$\langle \tilde{\Omega}(\mathbf{k}, \mathbf{p}, t) \tilde{\Omega}(\mathbf{k}', \mathbf{p}', t') \rangle = \langle \tilde{\Omega}(\mathbf{k}, \mathbf{p}, t) \tilde{\Omega}(\mathbf{k}', \mathbf{p}', t') \rangle^{\mathcal{U}} + \langle \tilde{\Omega}(\mathbf{k}, \mathbf{p}, t) \tilde{\Omega}(\mathbf{k}', \mathbf{p}', t') \rangle^{\mathcal{C}}, \quad (3.63)$$

where

$$\langle \tilde{\Omega}(\mathbf{k}, \mathbf{p}, t) \tilde{\Omega}(\mathbf{k}', \mathbf{p}', t') \rangle^{\mathcal{C}} = \left[\Omega_2^1(k, \mu, t, \mu', t') - \delta(\mu - \mu') \delta(\mathbf{k} + \mathbf{k}') \right] \cos \phi \cos \phi', \quad (3.64)$$

and

$$\begin{aligned} \langle \tilde{\Omega}(\mathbf{k}, \mathbf{p}, t) \tilde{\Omega}(\mathbf{k}', \mathbf{p}', t') \rangle^{\mathcal{U}} &= \frac{2n}{4\pi\tau} \delta(\mathbf{k} + \mathbf{k}') \left[\frac{1}{\pi} \sum_{m=1}^{\infty} \delta(\mu - \mu') \cos(m(\phi - \phi')) \right. \\ &\quad \left. + \frac{1}{4\pi} \int \int d\bar{\mu} d\bar{\mu}' \mathcal{G}^0(k, \mu, t | \bar{\mu}, s) \mathcal{G}^0(k', \mu', t' | \bar{\mu}', s') (2\delta(\bar{\mu} - \bar{\mu}') - 1) \right]. \end{aligned} \quad (3.65)$$

These expressions are used in the next section to derive results for physically relevant correlations, i.e. the velocity variance and the diffusivity of a passive tracer.

3.3.5 Results

Using the formulation developed in the previous section, we now examine the fluctuations in an active suspension near the threshold of collective motion. We study three specific quantities - the fluid velocity variance and covariance, the diffusivity of a passive non-Brownian tracer and the orientation (nematic) correlations between the swimmers.

Velocity Fluctuations - Velocity Variance

The velocity fluctuations in the swimmer suspension can be studied by examining the fluid velocity variance and covariance. We can separate the total velocity variance (\mathcal{V}) into the uncorrelated $\mathcal{V}^{\mathcal{U}}$ and correlated $\mathcal{V}^{\mathcal{C}}$ contributions as follows,

$$\begin{aligned}\mathcal{V} &= \mathcal{V}^{\mathcal{U}} + \mathcal{V}^{\mathcal{C}} \\ &= \int d\mathbf{k} \int d\mathbf{k}' \langle \tilde{\mathbf{u}}(\mathbf{k}, 0) \cdot \tilde{\mathbf{u}}(\mathbf{k}', 0) \rangle^{\mathcal{U}} + \int d\mathbf{k} \int d\mathbf{k}' \langle \tilde{\mathbf{u}}(\mathbf{k}, 0) \cdot \tilde{\mathbf{u}}(\mathbf{k}', 0) \rangle^{\mathcal{C}},\end{aligned}\quad (3.66)$$

where $\tilde{\mathbf{u}}(\mathbf{k}, t)$ is the fluid velocity in Fourier space. From the Fourier transformed Stokes equation one obtains,

$$\tilde{\mathbf{u}}(\mathbf{k}, t) = \mathcal{D} \frac{i}{2\pi k} \int d\mu d\phi \cos \phi \tilde{\Omega}(k, \mu, \phi, t) (1 - \mu^2)^{1/2} \mu. \quad (3.67)$$

Under the point-dipole approximation the uncorrelated component is a divergent quantity, so we use the slender body approximation to estimate the same [Nambiar, 2020].

Here, we calculate the correlated component of the velocity variance using the steady state phase space density correlation from (3.62); the final expression for the fluid velocity variance is obtained as,

$$\begin{aligned}\mathcal{V}^{\mathcal{C}} &= \int d\mathbf{k} \int d\mathbf{k}' \langle \tilde{\mathbf{u}}(\mathbf{k}, t) \cdot \tilde{\mathbf{u}}(\mathbf{k}', t) \rangle^{\mathcal{C}} \\ &= \mathcal{D}^2 L^3 \int_0^\infty dk \frac{-1}{(2\pi k)^2} \int_{-1}^1 \int_{-1}^1 d\mu d\mu' d\phi d\phi' \cos \phi \cos \phi' \langle \tilde{\Omega}(k, \mu, \phi, t) \tilde{\Omega}(k', \mu', \phi', t) \rangle^{\mathcal{C}} \\ &\quad (1 - \mu^2)^{1/2} (1 - \mu'^2)^{1/2} \mu \mu' \\ &= \mathcal{D}^2 L^3 \int_0^\infty dk \frac{-\pi^2}{(2\pi k)^2} \int_{-1}^1 \int_{-1}^1 d\mu d\mu' (\Omega_2^1(k, \mu, \mu') - \delta(\mu - \mu')) (1 - \mu^2)^{1/2} (1 - \mu'^2)^{1/2} \mu \mu', \\ &= \mathcal{D}^2 n L^3 \int_0^\infty dk \frac{-1}{(4\pi k)^2} \int_{-1}^1 \int_{-1}^1 d\mu d\mu' \sum_d \Phi_d^1(\mu; \mu_d) \tilde{\Phi}_d^1(\mu_d; \bar{\mu}) \frac{-2\pi i k \tau \mu_d}{2\pi i k \tau \mu_d + 1} \\ &\quad (1 - \mu^2)^{1/2} (1 - \mu'^2)^{1/2} \mu \mu',\end{aligned}\quad (3.68)$$

We evaluate the integrals in the above expression numerically. Figure 3.3a shows the variation of the total velocity variance for both pushers and pullers. Recall that a suspension of pushers shows a transition to collective motion at a finite threshold; this threshold has been shown to be given by the non-dimensional number density $((nL^2U\tau)_{cr})$ [Koch and Subramanian, 2011]; in the current non-dimensional formulation the threshold is numerically 20.125. On the other hand, a suspension of pullers does not show such a transition. Figure 3.3a shows that away from the threshold, as expected, the total velocity variance is the same for both pushers and pullers. As the threshold is approached, a bifurcation is observed between the two, and the velocity variance seems to diverge for pushers and stays finite for pullers. Figure 3.3b shows just the correlated component of the velocity variance for pushers, which confirms that the divergence is indeed due to correlations; the correlated component of the variance is seen to diverge as $\frac{1}{((nL^2U\tau)_{cr}) - (nL^2U\tau)^{1/2}}$ as the threshold $(nL^2U\tau)_{cr}$ is approached. This scaling can also be analytically seen by taking the $nL^2k \rightarrow 0$ limit of (3.68). Near the threshold the discrete eigenvalue becomes $O(k^2)$ instead of $O(1)$, and hence the relaxation of the correlation function occurs on increasingly large length scales. This long-ranged relaxation is also seen in equilibrium phase transitions [Chaikin and Lubensky, 2000]. The long ranged decay consequently leads to a divergence of the velocity variance.

Velocity Fluctuations - Velocity Co-variance

To study the spatial extent of the velocity fluctuations, we examine the velocity co-variance which is defined as,

$$\mathcal{V}(\mathbf{r}) = \langle \mathbf{u}(\mathbf{r}) \cdot \mathbf{u}(0) \rangle.$$

It can again be divided into the uncorrelated and correlated contributions as before,

$$\mathcal{V}(\mathbf{r}) = \mathcal{V}^{\mathcal{U}}(\mathbf{r}) + \mathcal{V}^{\mathcal{C}}(\mathbf{r}).$$

The exact expression for the correlated component can be derived following the exact same steps as the correlated component velocity variance earlier, and is as follows,

$$\mathcal{V}^{\mathcal{C}}(r) = \mathcal{D}^2 n L^3 \int_0^\infty dk \frac{-\sin(2k\pi r)}{(2k\pi r)(4\pi k)^2} \int_{-1}^1 \int_{-1}^1 d\mu d\mu' \sum_d \Phi_d^1(\mu; \mu_d) \tilde{\Phi}_d^1(\mu_d; \bar{\mu}) \frac{-2\pi i k \tau \mu_d}{2\pi i k \tau \mu_d + 1} (1 - \mu^2)^{1/2} (1 - \mu'^2)^{1/2} \mu \mu'. \quad (3.69)$$

Since we are considering correlations in an isotropic swimmer suspension, the covariance is only a function of the scalar separation, r . The integral is again evaluated numerically; to plot the results we normalize the velocity co-variance with the corresponding velocity

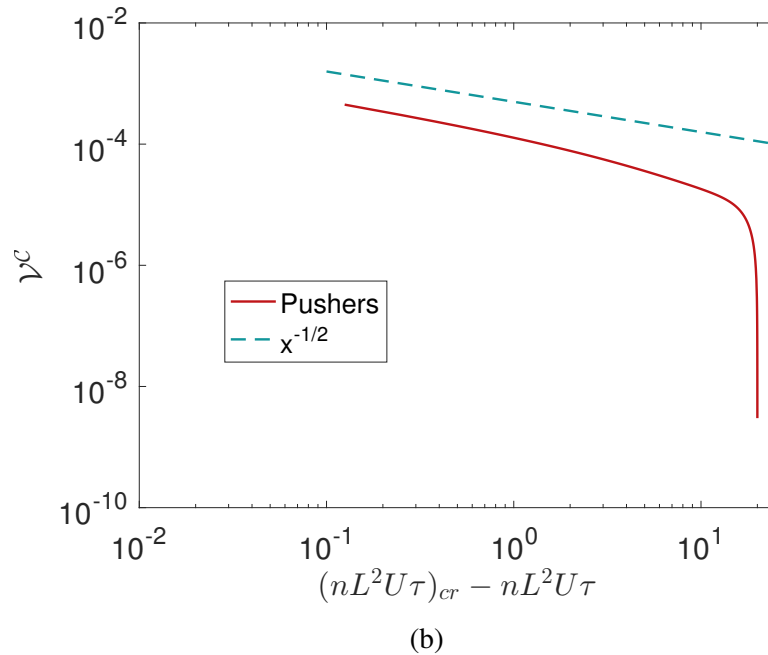
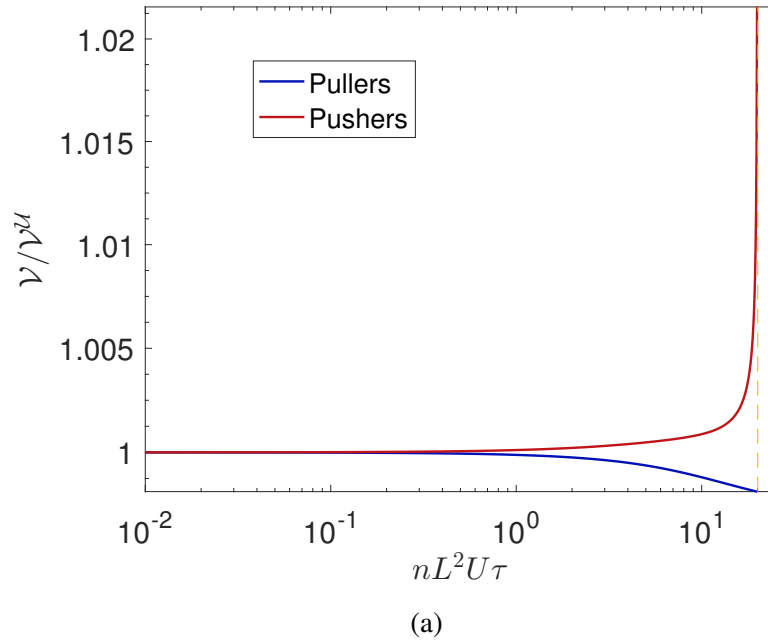


Fig. 3.3 (a) The variation of the total fluid velocity variance, including the correlated ($\mathcal{V}^{\mathcal{C}}$) and uncorrelated contributions ($\mathcal{V}^{\mathcal{U}}$), for varying $nL^2U\tau$ for pushers and pullers; the velocity variance is normalized by the uncorrelated component ($\mathcal{V}^{\mathcal{U}}$). (b) The variation of the correlated contribution ($\mathcal{V}^{\mathcal{C}}$) to the velocity variance versus $((nL^2U\tau)_{cr} - (nL^2U\tau))$ on a log-log plot, which shows that the power law of the divergence is $-1/2$ on approaching the threshold of collective motion for pushers; $(nL^2U\tau)_{cr} \sim 20.125$.

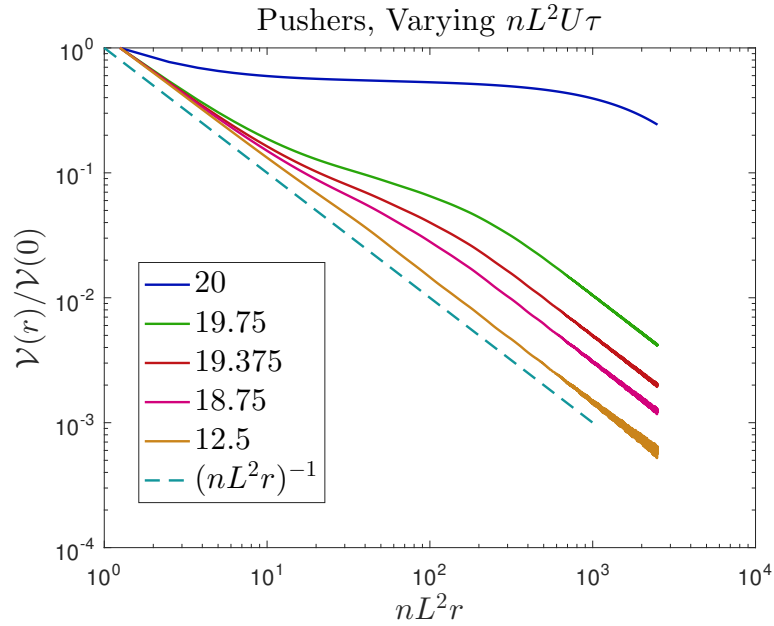


Fig. 3.4 The spatial decay of the net fluid velocity co-variance, including the correlated and uncorrelated contributions, for varying $nL^2U\tau$ for pushers; where the velocity co-variance is normalized with corresponding velocity ($\mathcal{V}(0)$) variance and the radial distance r is non-dimensionalised by the length scale $(nL^2)^{-1}$. On approaching the threshold of collective motion $((nL^2U\tau)_{cr} \sim 20.125)$, the co-variance becomes long ranged.

variance and non-dimensionalise the radial distance r is by the length scale $(nL^2)^{-1}$. Figure 3.4 shows the spatial variation of the total fluid velocity co-variance, including the correlated and uncorrelated components, for pushers. We see that the covariance decays over longer distances and thus the spatial correlations for the fluid velocity thus become long-ranged as the threshold is approached. This can be explained by noting that orientation relaxation occurs at long length scales ($r \sim (nL^2)^{-1}$) near the threshold; away from the threshold it occurs at the length scale of a single bacterium. Thus, the fluid flow induced by bacteria separated by long distances is increasingly correlated as the threshold for collective motion is approached. Away from the threshold, the uncorrelated component dominates and the velocity co-variance decays away as $1/r$ in the far-field as expected from earlier results [Krishnamurthy and Subramanian, 2015; Underhill and Graham, 2011].

Tracer Diffusivity

Using the Green-Kubo formula [Balakrishnan, 2008; Zwanzig, 2001], the diffusivity of a non-Brownian passive-tracer convected by the bacterial bath may be given as,

$$D = \int_0^\infty \int d\mathbf{k} \int d\mathbf{k}' \langle \tilde{\mathbf{u}}(\mathbf{k}, t) \cdot \tilde{\mathbf{u}}(\mathbf{k}', t) \rangle. \quad (3.70)$$

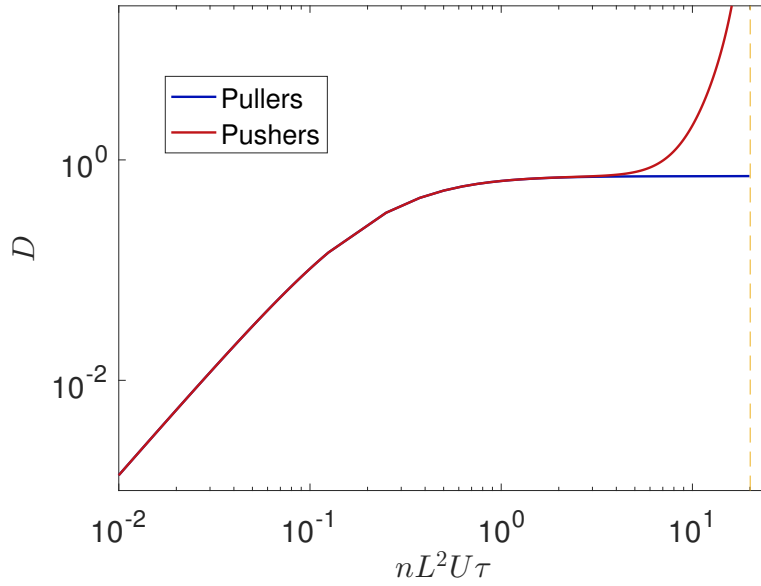
We again separate the uncorrelated and correlated contributions as,

$$\begin{aligned} D &= D^{\mathcal{U}} + D^{\mathcal{C}} \\ &= \int_0^\infty dt \int d\mathbf{k} \int d\mathbf{k}' \langle \tilde{\mathbf{u}}(\mathbf{k}, t) \cdot \tilde{\mathbf{u}}(\mathbf{k}', 0) \rangle^{\mathcal{U}} + \int_0^\infty dt \int d\mathbf{k} \int d\mathbf{k}' \langle \tilde{\mathbf{u}}(\mathbf{k}, t) \cdot \tilde{\mathbf{u}}(\mathbf{k}', 0) \rangle^{\mathcal{C}}. \end{aligned} \quad (3.71)$$

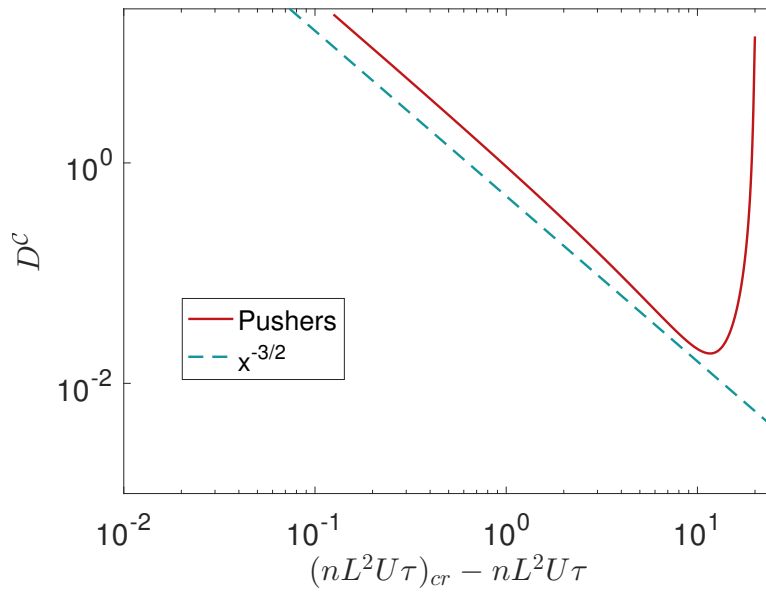
The uncorrelated contribution is the diffusivity of a passive tracer in a suspension at $O(nL^3)$. This was already derived in section 3.2 and is given in (3.12). Upon simplifying, following similar steps as for the velocity variance, we obtain the final expression for the correlated contribution to the tracer diffusivity as,

$$\begin{aligned} D^{\mathcal{C}} &= \mathcal{D}^2 nL^3 \int_0^\infty dk \frac{-1}{(4\pi k)^2} \int_{-1}^1 \int_{-1}^1 d\mu d\mu' \sum_d \Phi_d^1(\mu; \mu_d) \tilde{\Phi}_d^1(\mu_d; \bar{\mu}) \frac{1}{(2\pi i k \tau \mu_d + 1)^2} \\ &\quad (1 - \mu^2)^{1/2} (1 - \mu'^2)^{1/2} \mu \mu'. \end{aligned} \quad (3.72)$$

The final expression is again evaluated numerically. Figure 3.5a shows the total tracer diffusivity, including the correlated and uncorrelated contributions, for suspensions of pushers and pullers. Away from the threshold, where the uncorrelated contribution dominates we see that the tracer diffusivity is the same for both pushers and pullers. As the threshold of collective motion is approached, we see a divergence between the two. The diffusivity in a pusher suspension starts to increase due to the correlated contribution and diverges as the threshold is approached. Figure 3.5b shows just the correlated contribution and we see that the divergence of correlated contribution to the diffusivity is stronger than that for the velocity variance and is proportional to $\frac{1}{((nL^2 U \tau)_{cr} - (nL^2 U \tau))^{3/2}}$. This scaling can also be analytically recovered by taking the limit $nL^2 k \rightarrow 0$ of (3.72). The stronger divergence in this case is understood by noting that the divergence of the tracer diffusivity depends on the product of the velocity variance scale, $O(k^2)$, and the scale for the correlation time, $O(k^2)$, as one approaches the threshold which leads to the decay of the correlations being $O(k^2)^2$ near the threshold. Note that in contrast, the diffusivity stays finite for pullers.



(a)



(b)

Fig. 3.5 (a) The variation of the total tracer diffusivity, including the correlated and uncorrelated contributions, of a passive tracer for varying $nL^2U\tau$ for pushers and pullers. (b) The variation of the correlated contribution (D^c) to the tracer diffusivity versus $((nL^2U\tau)_{cr} - (nL^2U\tau))$ on a log-log plot, which shows that the power law of the divergence is $-3/2$ on approaching the threshold of collective motion for pushers; $(nL^2U\tau)_{cr} \sim 20.125$.

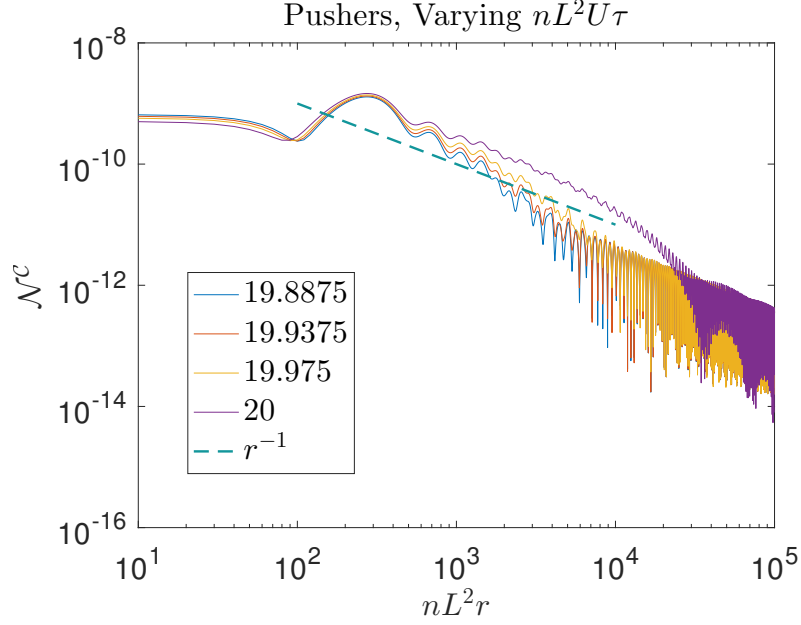


Fig. 3.6 The variation of the nematic correlations of the swimmers orientations for varying $nL^2U\tau$ for pushers; $(nL^2U\tau)_{cr} \sim 20.125$.

Orientation Correlations

To examine the orientation correlations, we consider the nematic parameter defined as $\mathbf{N} = \mathbf{p}\mathbf{p}$. The nematic correlations (\mathcal{N}^c) in the suspension are given as,

$$\begin{aligned} \mathcal{N}^c &= \langle \mathbf{N}(\mathbf{r}) : \mathbf{N}(0) \rangle = \int d\mathbf{k} \int d\mathbf{k}' e^{2\pi i \mathbf{k} \cdot \mathbf{r}} \langle \mathbf{p}\mathbf{p} : \mathbf{p}'\mathbf{p}' \rangle^c \\ &= \mathcal{D}^2 nL^3 \int_0^\infty dk \frac{-\sin(2\pi kr)}{(2\pi kr)(4\pi k)^2} \int_{-1}^1 \int_{-1}^1 d\mu d\mu' \sum_d \Phi_d^1(\mu; \mu_d) \tilde{\Phi}_d^1(\mu_d; \bar{\mu}) \frac{-2\pi i k \tau \mu_d}{2\pi i k \tau \mu_d + 1} \mu^2 (\mu')^2. \end{aligned} \quad (3.73)$$

Since the swimmer suspension is isotropic, the nematic correlations again only depend on the radial distance (r) and we again evaluate the integral numerically. Figure 3.6 shows the nematic correlations for suspensions of pushers. Unlike the velocity correlations, we see that the nematic correlations neither diverge nor become long ranged as the threshold for collective motion is approached. This can also be seen by taking the $nL^2k \rightarrow 0$ limit of the integral and we see an $O(1/r)$ decay of the correlations in the far-field. The orientation correlations by themselves thus do not become long-ranged near the threshold. This points to the crucial role of studying the velocity fluctuations when trying to get theoretical insight into the transition to collective motion in dilute bacterial suspensions.

3.4 Conclusion

In this chapter, we have theoretically studied the correlations in a bacterial suspension. First, we examined the correlations away from the collective motion threshold where pairwise hydrodynamic interactions dominate. The tracer diffusivity was found to diverge linearly with the swimmer run length at $O(nL^3)^2$, where nL^3 is the volume fraction. The correlations also provide a distinction between pushers and pullers, where they enhance the diffusivity only for the former. Next, we examine the correlations as the threshold of collective motion is approached. This is done by formulating a fluctuating kinetic theory for the bacterial suspension, following the stochastic field theories used to study phase transitions in equilibrium systems. We derive an exact solution for the governing equation by deriving the eigenfunctions and the adjoints, and then using them to derive the Green's function. This is used to derive the correlations when accounting for the long-ranged interactions near the threshold of collective motion. Finally, we use our analytical expressions to examine the fluid velocity variance, tracer diffusivity and orientation correlations. We show the fluid velocity variance and tracer diffusivity diverge as the threshold is approached, but the orientation correlations stay finite. The velocity variance (tracer diffusivity) diverges with the power law $-1/2$ ($-3/2$) as the threshold is approached.

An approximation that is sometimes used to theoretically examine bacterial suspensions in the literature is to assume swimmers that do not swim (i.e. have no run phase), but whose orientation still decorrelates due to tumbling (see for instance [Stenhammar et al. \[2017\]](#)). Here, the eigenvalue becomes independent of the wavenumber k since all relaxation occurs on a uniform scale. For this case, the scaling analysis in turn suggests that the power law associated with the divergence of the velocity variance (tracer diffusivity) is -1 (-2). This is an important difference from the complete case that we have analysed. The no-swimming approximation drops the spatial dependence of the relaxation of the correlation function completely, and in turn leads to slightly misleading power-laws for the divergence. We thus see that it is crucial to retain the swimming term when analysing the correlations in a bacterial suspension.

We discuss a few possible generalisations of our results here. To make analytical progress, we had simplified the suspension velocity, such that it was coming from a super-position of dipoles in the far-field. While an exact solution for the case of slender bodies is not possible, scaling analysis can be used to verify that the power-law of the divergence does not change in this case. Another generalisation would be to incorporate the effect of the mean fluctuating flow field on the pairwise hydrodynamic interactions studied in section 3.2 or to incorporate external fields such as chemotaxis [[Kasyap and Koch, 2012](#)] or shear flow [[López et al., 2015](#)], and examine if either of those change the divergence of the correlations near the

threshold. A final possible generalisation would be two dimensions to, following the analysis in Chapter 2.

References

- Ablowitz, M. J., Fokas, A. S., and Fokas, A. (2003). *Complex variables: introduction and applications*. Cambridge University Press.
- Agarwal, A., Brandt, L., and Zaki, T. A. (2014). Linear and nonlinear evolution of a localized disturbance in polymeric channel flow. *J. Fluid Mech.*, 760:278–303.
- Angelani, L. (2013). Averaged run-and-tumble walks. *EPL (Europhysics Letters)*, 102(2):20004.
- Argun, A., Moradi, A.-R., Pinçe, E., Bağcı, G. B., Imparato, A., and Volpe, G. (2016). Non-boltzmann stationary distributions and nonequilibrium relations in active baths. *Physical Review E*, 94(6):062150.
- Avila, K., Moxey, D., de Lozar, A., Avila, M., Barkley, D., and Hof, B. (2011). The onset of turbulence in pipe flow. *Science*, 333(6039):192–196.
- Balakrishnan, V. (2008). *Elements of nonequilibrium statistical mechanics*. Ane Books.
- Balmforth, N. and Morrison, P. (1995a). Normal modes and continuous spectra. *Annals of the New York Academy of Science*, 773(1):80–94.
- Balmforth, N. and Morrison, P. (1995b). Singular eigenfunctions for shearing fluids i. Technical report, Texas Univ.
- Balmforth, N., Morrison, P., and Thiffeault, J.-L. (2013). Pattern formation in hamiltonian systems with continuous spectra; a normal-form single-wave model. *arXiv preprint arXiv:1303.0065*.
- Bárdfalvy, D., Nordanger, H., Nardini, C., Morozov, A., and Stenhammar, J. (2019). Particle-resolved lattice boltzmann simulations of 3-dimensional active turbulence. *Soft Matter*, 15(39):7747–7756.
- Barkley, D. (1990). Theory and predictions for finite-amplitude waves in two-dimensional plane poiseuille flow. *Physics of Fluids A: Fluid Dynamics*, 2(6):955–970.
- Barkley, D. (2016). Theoretical perspective on the route to turbulence in a pipe. *J. Fluid Mech.*, 803.
- Baskaran, A. and Marchetti, M. C. (2009). Statistical mechanics and hydrodynamics of bacterial suspensions. *Proceedings of the National Academy of Sciences*, 106(37):15567–15572.

- Baumert, B. M. and Muller, S. J. (1999). Axisymmetric and non-axisymmetric elastic and inertio-elastic instabilities in taylor–couette flow. *Journal of non-newtonian fluid mechanics*, 83(1-2):33–69.
- Bechinger, C., Di Leonardo, R., Löwen, H., Reichhardt, C., Volpe, G., and Volpe, G. (2016). Active particles in complex and crowded environments. *Reviews of Modern Physics*, 88(4):045006.
- Belan, S. and Kardar, M. (2019). Pair dispersion in dilute suspension of active swimmers. *The Journal of chemical physics*, 150(6):064907.
- Ben Dor, Y., Kafri, Y., and Tailleur, J. (2018). Forces in dry active matter. *arXiv preprint arXiv:1811.08829*.
- Ben-Dov, G. and Cohen, J. (2007). Critical reynolds number for a natural transition to turbulence in pipe flows. *Phys. Rev. Lett.*, 98(6):064503.
- Bennett, R. R. and Golestanian, R. (2013). Emergent run-and-tumble behavior in a simple model of chlamydomonas with intrinsic noise. *Physical review letters*, 110(14):148102.
- Berg, H. C. (1993). *Random walks in biology*. Princeton University Press.
- Berg, H. C. (2008). *E. coli in Motion*. Springer Science & Business Media.
- Berg, H. C. and Brown, D. A. (1972). Chemotaxis in escherichia coli analysed by three-dimensional tracking. *Nature*, 239(5374):500.
- Beris, A. N. and Dimitropoulos, C. D. (1999). Pseudospectral simulation of turbulent viscoelastic channel flow. *Computer methods in applied mechanics and engineering*, 180(3-4):365–392.
- Berman, N. S. (1978). Drag reduction by polymers. *Annu. Rev. Fluid Mech.*, 10:47.
- Bertola, V., Meulenbroek, B., Wagner, C., Storm, C., Morozov, A., van Saarloos, W., and Bonn, D. (2003). Nonlinear elastic instability in channel flows at low reynolds numbers. *Phys. Rev. Lett.*, 90(11):114502.
- Bistagnino, A., Boffetta, G., Celani, A., Mazzino, A., Puliafito, A., and Vergassola, M. (2007). Nonlinear dynamics of the viscoelastic kolmogorov flow. *Journal of fluid mechanics*, 590:61–80.
- Boyd, J. P. (1999). *Chebyshev and Fourier Spectral Methods*. Springer-Verlag, second edition.
- Burger, E., Munk, W., and Wahl, H. (1982). Flow increase in the trans alaska pipeline through use of a polymeric drag-reducing additive. *J. Petroleum Technol.*, 34:377.
- Case, K. (1978). Plasma oscillations. *The Physics of Fluids*, 21(2):249–257.
- Case, K. M. (1959). Plasma oscillations. *Annals of Physics*, 7(3):349–364.
- Case, K. M. (1960). Elementary solutions of the transport equation and their applications. *Annals of Physics*, 9(1):1–23.

- Cates, M. E. (2012). Diffusive transport without detailed balance in motile bacteria: does microbiology need statistical physics? *Reports on Progress in Physics*, 75(4):042601.
- Cates, M. E. (2019). Active field theories. *arXiv preprint arXiv:1904.01330*.
- Cates, M. E. and Tailleur, J. (2015). Motility-induced phase separation. *Annu. Rev. Condens. Matter Phys.*, 6(1):219–244.
- Cates, M. E. and Tjhung, E. (2018). Theories of binary fluid mixtures: from phase-separation kinetics to active emulsions. *Journal of Fluid Mechanics*, 836.
- Chaikin, P. M. and Lubensky, T. C. (2000). *Principles of condensed matter physics*, volume 1. Cambridge university press Cambridge.
- Chandra, B., Shankar, V., and Das, D. (2018). Onset of transition in the flow of polymer solutions through microtubes. *Journal of Fluid Mechanics*, 844:1052–1083.
- Chandra, B., Shankar, V., and Das, D. (2020). Early transition, relaminarization and drag reduction in the flow of polymer solutions through microtubes. *Journal of Fluid Mechanics*, 885:A47.
- Chaté, H. (2020). Dry aligning dilute active matter. *Annual Review of Condensed Matter Physics*, 11:189–212.
- Chen, C., Liu, S., Shi, X.-q., Chaté, H., and Wu, Y. (2017). Weak synchronization and large-scale collective oscillation in dense bacterial suspensions. *Nature*, 542(7640):210–214.
- Chen, D. T., Lau, A., Hough, L. A., Islam, M. F., Goulian, M., Lubensky, T. C., and Yodh, A. G. (2007a). Fluctuations and rheology in active bacterial suspensions. *Physical Review Letters*, 99(14):148302.
- Chen, D. T. N., Lau, A. W. C., Hough, L. A., Islam, M. F., Goulian, M., Lubensky, T. C., and Yodh, A. G. (2007b). Fluctuations and rheology in active bacterial suspensions. *Physical Review Letters*, 99:148302.
- Choueiri, G. H., Lopez, J. M., and Hof, B. (2018). Exceeding the asymptotic limit of polymer drag reduction. *Physical review letters*, 120(12):124501.
- Choueiri, G. H., Lopez, J. M., Varshney, A., Sankar, S., and Hof, B. (2021). Experimental observation of the origin and structure of elastoinertial turbulence. *Proceedings of the National Academy of Sciences*, 118(45).
- Clasen, C., Plog, J., Kulicke, W.-M., Owens, M., Macosko, C., Scriven, L., Verani, M., and McKinley, G. H. (2006). How dilute are dilute solutions in extensional flows? *Journal of Rheology*, 50(6):849–881.
- Dean, D. S. (1996). Langevin equation for the density of a system of interacting langevin processes. *Journal of Physics A: Mathematical and General*, 29(24):L613.
- Detcheverry, F. (2015). Non-poissonian run-and-turn motions. *EPL (Europhysics Letters)*, 111(6):60002.

- Detcheverry, F. (2017). Generalized run-and-turn motions: From bacteria to lévy walks. *Physical Review E*, 96(1):012415.
- Dhar, A., Kundu, A., Majumdar, S. N., Sabhapandit, S., and Schehr, G. (2019). Run-and-tumble particle in one-dimensional confining potentials: Steady-state, relaxation, and first-passage properties. *Physical Review E*, 99(3):032132.
- Dombrowski, C., Cisneros, L., Chatkaew, S., Goldstein, R. E., and Kessler, J. O. (2004). Self-concentration and large-scale coherence in bacterial dynamics. *Physical review letters*, 93(9):098103.
- Doostmohammadi, A., Ignés-Mullol, J., Yeomans, J. M., and Sagués, F. (2018). Active nematics. *Nature communications*, 9(1):3246.
- Draad, A., Kuiken, G. D. C., and Nieuwstadt, F. T. M. (1998). Laminar–turbulent transition in pipe flow for newtonian and non-newtonian fluids. *J. Fluid Mech.*, 377:267–312.
- Drazin, P. G. and Reid, W. H. (1981). *Hydrodynamic stability*. Cambridge University Press, Cambridge.
- Dubief, Y., Terrapon, V., and Soria, J. (2013). On the mechanism of elasto-inertial turbulence. *Phys. Fluids*, 25(11):110817.
- Dufresne, E. R. (2019). Active materials: Biological benchmarks and transport limitations. *arXiv preprint arXiv:1903.09584*.
- Ebbens, S., Jones, R. A., Ryan, A. J., Golestanian, R., and Howse, J. R. (2010). Self-assembled autonomous runners and tumblers. *Physical Review E*, 82(1):015304.
- Eckhardt, B., Schneider, T. M., Hof, B., and Westerweel, J. (2007). Turbulence transition in pipe flow. *Annu. Rev. Fluid Mech.*, 39:447–468.
- El-Kareh, A. W. and Leal, L. G. (1989). Existence of solutions for all Deborah numbers for a non-newtonian model modified to include diffusion. *Journal of Non-Newtonian Fluid Mechanics*, 33(3):257–287.
- Elgeti, J., Winkler, R. G., and Gompper, G. (2015). Physics of microswimmers—single particle motion and collective behavior: a review. *Reports on progress in physics*, 78(5):056601.
- Ezhilan, B., Alonso-Matilla, R., and Saintillan, D. (2015). On the distribution and swim pressure of run-and-tumble particles in confinement. *Journal of Fluid Mechanics*, 781.
- Forame, P. C., Hansen, R. J., and Little, R. C. (1972). Observations of early turbulence in the pipe flow of drag reducing polymer solutions. *AIChE Journal*, 18(1):213–217.
- Friedman, B. (1990). *Principles and techniques of applied mathematics*. Courier Dover Publications.
- Gachelin, J., Rousselet, A., Lindner, A., and Clement, E. (2014). Collective motion in an active suspension of escherichia coli bacteria. *New Journal of Physics*, 16(2):025003.
- Gakhov, F. D. (2014). *Boundary value problems*. Elsevier.

- Gardiner, C. W. et al. (1985). *Handbook of stochastic methods*, volume 3. Springer Berlin.
- Garg, P., Chaudhary, I., Khalid, M., Shankar, V., and Subramanian, G. (2018). Viscoelastic pipe flow is linearly unstable. *Physical review letters*, 121(2):024502.
- Gill, A. E. (1965). On the behaviour of small disturbances to poiseuille flow in a circular pipe. *J. Fluid Mech.*, 21:145–172.
- Goldstein, R., Adrian, R., and Kreid, D. (1969). Turbulent and transition pipe flow of dilute aqueous polymer solutions. *Industrial and Engineering Chemistry Fundamentals*, 8(3):498–502.
- Goldstein, R. E. (2015). Green algae as model organisms for biological fluid dynamics. *Annual review of fluid mechanics*, 47:343–375.
- Gorodtsov, V. and Leonov, A. (1967). On a linear instability of a plane parallel couette flow of viscoelastic fluid. *Journal of applied mathematics and mechanics.*, 31(2):310–319.
- Graham, M. D. (1998). Effect of axial flow on viscoelastic Taylor-Couette instability. *J. Fluid Mech.*, 360:341–374.
- Graham, M. D. (2014). Drag reduction and the dynamics of turbulence in simple and complex fluids. *Phys. Fluids*, 26(10):101301.
- Grillet, A. M., Bogaerds, A. C., Peters, G. W., and Baaijens, F. P. (2002). Stability analysis of constitutive equations for polymer melts in viscometric flows. *J. Non-Newton. Fluid Mech.*, 103(2):221–250.
- Gupta, A. and Vincenzi, D. (2019). Effect of polymer-stress diffusion in the numerical simulation of elastic turbulence. *Journal of Fluid Mechanics*, 870:405–418.
- Hansen, R. J. (1973). Stability of laminar pipe flows of drag reducing polymer solutions in the presence of high-phase-velocity disturbances. *AIChE Journal*, 19(2):293–304.
- Hansen, R. J., Little, R., and Forame, P. (1973). Experimental and theoretical studies of early turbulence. *Journal of Chemical Engineering of Japan*, 6(4):310–314.
- Hansen, R. J. and Little, R. C. (1974). Early turbulence and drag reduction phenomena in larger pipes. *Nature*, 252(5485):690–690.
- Hildebrand, E. J., Buice, M. A., and Chow, C. C. (2007). Kinetic theory of coupled oscillators. *Physical review letters*, 98(5):054101.
- Hoda, N., Jovanovic, M., and Kumar, S. (2008). Energy amplification in channel flows of viscoelastic fluids. *J. Fluid Mech.*, 601:407–424.
- Hof, B., Juel, A., and Mullin, T. (2003). Scaling of the turbulence transition threshold in a pipe. *Phys. Rev. Lett.*, 91(24):244502.
- Hong, S. O., Cooper-White, J. J., and Kim, J. M. (2016). Inertio-elastic mixing in a straight microchannel with side wells. *Applied Physics Letters*, 108(1):014103.

- Hoyt, J. W. (1977). Laminar-turbulent transition in polymer solutions. *Nature*, 270(5637):508–509.
- Jepson, A., Martinez, V. A., Schwarz-Linek, J., Morozov, A., and Poon, W. C. (2013). Enhanced diffusion of nonswimmers in a three-dimensional bath of motile bacteria. *Physical Review E*, 88(4):041002.
- Jones, W. and Maddock., J. L. (1966). Onset of instabilities and reduction of drag in the flow of relaxing liquids through tubes and porous beds. *Nature*, 212(5060):388–390.
- Jones, W., Marshall, D., and Walker, P. (1976). The flow of dilute aqueous solutions of macromolecules in various geometries. ii. straight pipes of circular cross-section. *Journal of Physics D: Applied Physics*, 9(5):735.
- Kanazawa, K., Sano, T. G., Cairoli, A., and Baule, A. (2020). Loopy lévy flights enhance tracer diffusion in active suspensions. *Nature*, 579(7799):364–367.
- Karani, H., Pradillo, G. E., and Vlahovska, P. M. (2019). Tuning the random walk of active colloids: From individual run-and-tumble to dynamic clustering. *Physical Review Letters*, 123(20):208002.
- Kasyap, T. and Koch, D. L. (2012). Chemotaxis driven instability of a confined bacterial suspension. *Physical review letters*, 108(3):038101.
- Kasyap, T., Koch, D. L., and Wu, M. (2014). Hydrodynamic tracer diffusion in suspensions of swimming bacteria. *Physics of Fluids (1994-present)*, 26(8):081901.
- Kerswell, R. (2005). Recent progress in understanding the transition to turbulence in a pipe. *Nonlinearity.*, 18(6):R17.
- Kim, M. J. and Breuer, K. S. (2004). Enhanced diffusion due to motile bacteria. *Physics of fluids*, 16(9):L78–L81.
- Koch, D. L. and Shaqfeh, E. (1991). Screening in sedimenting suspensions. *Journal of fluid mechanics*, 224:275–303.
- Koch, D. L. and Subramanian, G. (2011). Collective hydrodynamics of swimming microorganisms: Living fluids. *Annual Review of Fluid Mechanics*, 43:637–659.
- Krishnamurthy, D. and Subramanian, G. (2015). Collective motion in a suspension of micro-swimmers that run-and-tumble and rotary diffuse. *Journal of Fluid Mechanics*, 781:422–466.
- Kumaran, V. (2015). Experimental studies on the flow through soft tubes and channels. *Sadhana*, 40(3):911–923.
- Kupferman, R. (2005). On the linear stability of plane couette flow for an oldroyd-b fluid and its numerical approximation. *J. Non-Newton. Fluid Mech.*, 127:169–190.
- Kurchan, J. (2009). Six out of equilibrium lectures. *arXiv preprint arXiv:0901.1271*.

- Kurzthaler, C., Devailly, C., Arlt, J., Franosch, T., Poon, W. C., Martinez, V. A., and Brown, A. T. (2018). Probing the spatiotemporal dynamics of catalytic janus particles with single-particle tracking and differential dynamic microscopy. *Physical review letters*, 121(7):078001.
- Kurzthaler, C. and Franosch, T. (2017). Intermediate scattering function of an anisotropic brownian circle swimmer. *Soft matter*, 13(37):6396–6406.
- Kurzthaler, C., Leitmann, S., and Franosch, T. (2016). Intermediate scattering function of an anisotropic active brownian particle. *Scientific reports*, 6:36702.
- Larson, R. G. (1988). *Constitutive Equations for Polymer Melts and Solutions*. Butterworths, Boston.
- Larson, R. G. (1992). Instabilities in viscoelastic flows. *Rheologica Acta*, 31(3):213–263.
- Larson, R. G., Shaqfeh, E. S. G., and Muller, S. J. (1990). A purely elastic instability in taylor-couette flow. *J. Fluid Mech.*, 218:573–600.
- Lauga, E. (2016). Bacterial hydrodynamics. *Annual Review of Fluid Mechanics*, 48:105–130.
- Lauga, E. and Powers, T. R. (2009). The hydrodynamics of swimming microorganisms. *Reports on Progress in Physics*, 72(9):096601.
- Li, W., Xi, L., and Graham, M. D. (2006). Nonlinear travelling waves as a framework for understanding turbulent drag reduction. *J. Fluid Mech.*, 565:353–362.
- Li, X.-B., Li, F.-C., Cai, W.-H., Zhang, H.-N., and Yang, J.-C. (2012). Very-low-re chaotic motions of viscoelastic fluid and its unique applications in microfluidic devices: a review. *Experimental thermal and fluid science*, 39:1–16.
- Lieu, B., Jovanovic, M., and Kumar, S. (2013). Worst-case amplification of disturbances in inertialess couette flow of viscoelastic fluids. *J. Fluid Mech.*, 601:232–263.
- Lighthill, M. J. (1958). *An introduction to Fourier analysis and generalised functions*. Cambridge University Press.
- Lim, E. J., Ober, T. J., Edd, J. F., Desai, S. P., Neal, D., Bong, K. W., Doyle, P. S., McKinley, G. H., and Toner, M. (2014). Inertio-elastic focusing of bioparticles in microchannels at high throughput. *Nature communications*, 5.
- Little, R. C. and Wiegard, M. (1970). Drag reduction and structural turbulence in flowing polyox solutions. *Journal of Applied Polymer Science*, 14(2):409–419.
- López, H. M., Gachelin, J., Douarche, C., Auradou, H., and Clément, E. (2015). Turning bacteria suspensions into superfluids. *Physical review letters*, 115(2):028301.
- Lopez, J. M., Choueiri, G. H., and Hof, B. (2019). Dynamics of viscoelastic pipe flow at low reynolds numbers in the maximum drag reduction limit. *Journal of Fluid Mechanics*, 874:699–719.
- Lozano, C., Gomez-Solano, J. R., and Bechinger, C. (2018). Run-and-tumble-like motion of active colloids in viscoelastic media. *New Journal of Physics*, 20(1):015008.

- Lumley, J. L. (1969). Drag reduction by additives. *Annu. Rev. Fluid Mech.*, 1:367.
- Maggi, C., Paoluzzi, M., Pellicciotta, N., Lepore, A., Angelani, L., and Di Leonardo, R. (2014). Generalized energy equipartition in harmonic oscillators driven by active baths. *Physical review letters*, 113(23):238303.
- Malakar, K., Jemseena, V., Kundu, A., Kumar, K. V., Sabhapandit, S., Majumdar, S. N., Redner, S., and Dhar, A. (2018). Steady state, relaxation and first-passage properties of a run-and-tumble particle in one-dimension. *Journal of Statistical Mechanics: Theory and Experiment*, 2018(4):043215.
- Marchetti, M. C., Joanny, J.-F., Ramaswamy, S., Liverpool, T. B., Prost, J., Rao, M., and Simha, R. A. (2013). Hydrodynamics of soft active matter. *Reviews of Modern Physics*, 85(3):1143.
- Martens, K., Angelani, L., Di Leonardo, R., and Bocquet, L. (2012). Probability distributions for the run-and-tumble bacterial dynamics: An analogy to the lorentz model. *The European Physical Journal E*, 35(9):84.
- Meseguer, A. and Trefethen, L. (2003). Linearized pipe flow to reynolds number 10⁷. *Journal of Computational Physics*, 186(1):178–197.
- Morozov, A. and van Saarloos, W. (2007). An introductory essay on subcritical instabilities and the transition to turbulence in visco-elastic parallel shear flows. *Phys. Rep.*, 447:112–143.
- Morozov, A. and Van Saarloos, W. (2019). Subcritical instabilities in plane poiseuille flow of an oldroyd-b fluid. *Journal of Statistical Physics*, 175(3):554–577.
- Morozov, A. N. and van Saarloos, W. (2005). Subcritical finite-amplitude solutions for plane couette flow of viscoelastic fluids. *Phys. Rev. Lett.*, 95(2):024501.
- Mullin, T. (2011). Experimental studies of transition to turbulence in a pipe. *Annu. Rev. Fluid Mech.*, 43:1–24.
- Nambiar, S. (2020). *Swimmer suspensions: fluctuations, microstructure and rheology*. PhD thesis, Jawaharlal Nehru Centre for Advanced Scientific Research.
- Nambiar, S., Garg, P., and Subramanian, G. (2021). Enhanced velocity fluctuations in interacting swimmer suspensions. *Journal of Fluid Mechanics*, 907.
- Nambiar, S., Nott, P., and Subramanian, G. (2017). Stress relaxation in a dilute bacterial suspension. *Journal of Fluid Mechanics*, 812:41–64.
- Nambiar, S., Phanikanth, S., Nott, P., and Subramanian, G. (2019). Stress relaxation in a dilute bacterial suspension: the active–passive transition. *Journal of Fluid Mechanics*, 870:1072–1104.
- Nash, R., Adhikari, R., Tailleur, J., and Cates, M. (2010). Run-and-tumble particles with hydrodynamics: sedimentation, trapping, and upstream swimming. *Physical review letters*, 104(25):258101.

- Neelamegam, R., Shankar, V., and Das, D. (2013). Suppression of purely elastic instabilities in the torsional flow of viscoelastic fluid past a soft solid. *Phys. Fluids*, 25(12):124102.
- Nicholson, D. R. (1983). *Introduction to plasma theory*. Wiley New York.
- Othmer, H. G., Dunbar, S. R., and Alt, W. (1988). Models of dispersal in biological systems. *Journal of mathematical biology*, 26(3):263–298.
- Pan, L., Morozov, A., Wagner, C., and Arratia, P. E. (2013). Nonlinear elastic instability in channel flows at low reynolds numbers. *Phys. Rev. Lett.*, 110(17):174502.
- Paterson, R. W. and Abernathy, F. H. (1972). Transition to turbulence in pipe flow for water and dilute solutions of polyethylene oxide. *J. Fluid Mech.*, 51(1):177–185.
- Patteson, A. E., Gopinath, A., Purohit, P. K., and Arratia, P. E. (2016). Particle diffusion in active fluids is non-monotonic in size. *Soft matter*, 12(8):2365–2372.
- Peng, Y., Lai, L., Tai, Y.-S., Zhang, K., Xu, X., and Cheng, X. (2016). Diffusion of ellipsoids in bacterial suspensions. *Physical review letters*, 116(6):068303.
- Pfenniger, W. (1961). Transition in the inlet length of tubes at high reynolds numbers. *Boundary layer and flow control (ed. GV Lachman)*, pages 970–980.
- Polin, M., Tuval, I., Drescher, K., Gollub, J. P., and Goldstein, R. E. (2009). Chlamydomonas swims with two “gears” in a eukaryotic version of run-and-tumble locomotion. *Science*, 325(5939):487–490.
- Poole, R. J., Alves, M. A., and Oliveira, P. J. (2007). Purely elastic flow asymmetries. *Phys. Rev. Lett.*, 99(16):164503.
- Ram, A. and Tamir, A. (1964). Structural turbulence in polymer solutions. *Journal of Applied Polymer Science*, 8(6):2751–2762.
- Ramkrishna, D. and Amundson, N. R. (1985). *Linear operator methods in chemical engineering with applications to transport and chemical reaction systems*. Prentice Hall.
- Renardy, M. and Renardy, Y. (1986). Linear stability of plane couette flow of an upper convected maxwell fluid. *J. Non-Newton. Fluid Mech.*, 22(1):23–33.
- Romanczuk, P., Bär, M., Ebeling, W., Lindner, B., and Schimansky-Geier, L. (2012). Active brownian particles. *The European Physical Journal Special Topics*, 202(1):1–162.
- Roy, A., Garg, P., Reddy, J. S., and Subramanian, G. (2022). Inertio–elastic instability of a vortex column. *Journal of Fluid Mechanics*, 937.
- Roy, A., Morozov, A., van Saarloos, W., and Larson, R. G. (2006). Mechanism of polymer drag reduction using a low-dimensional model. *Phys. Rev. Lett.*, 97(23):234501.
- Roy, A. and Subramanian, G. (2014a). An inviscid modal interpretation of the ‘lift-up’ effect. *Journal of Fluid Mechanics*, 757:82–113.
- Roy, A. and Subramanian, G. (2014b). Linearized oscillations of a vortex column: the singular eigenfunctions. *Journal of Fluid Mechanics*, 741:404–460.

- Saintillan, D. (2018). Rheology of active fluids. *Annual Review of Fluid Mechanics*, 50:563–92.
- Saintillan, D. and Shelley, M. J. (2007). Orientational order and instabilities in suspensions of self-locomoting rods. *Phys. Rev. Lett.*, 99(5):058102.
- Samanta, D. (2013). Transition to turbulence in newtonian and non newtonian fluids. *Phd Thesis, Saarbrucken University*.
- Samanta, D., Dubief, Y., Holzner, M., Schafer, C., Morozov, A., Wagner, C., and Hof, B. (2013). Elasto-inertial turbulence. *Proc. Nat. Acad. Sci.*, 110:10557–10562.
- Sandoval, M., Marath, N. K., Subramanian, G., and Lauga, E. (2014). Stochastic dynamics of active swimmers in linear flows. *Journal of Fluid Mechanics*, 742:50–70.
- Schmid, P. J. and Henningson, D. S. (2001). *Stability and Transition in Shear flows*. Springer: Newyork.
- Schnitzer, M. J. (1993). Theory of continuum random walks and application to chemotaxis. *Physical Review E*, 48(4):2553.
- Schwarz-Linek, J., Arlt, J., Jepson, A., Dawson, A., Vissers, T., Miroli, D., Pilizota, T., Martinez, V. A., and Poon, W. C. (2016). Escherichia coli as a model active colloid: A practical introduction. *Colloids and Surfaces B: Biointerfaces*, 137:2–16.
- Sedlacek, Z. (1971). Electrostatic oscillations in cold inhomogeneous plasma i. differential equation approach. *J. Plasma Phys.*, 5:239.
- Sevilla, F. J., Arzola, A. V., and Cital, E. P. (2019). Stationary superstatistics distributions of trapped run-and-tumble particles. *Physical Review E*, 99(1):012145.
- Shaqfeh, E. S. G. (1996). Purely elastic instabilities in viscometric flows. *Annu. Rev. Fluid Mech.*, 28:129–185.
- Sid, S., Terrapon, V., and Dubief, Y. (2018a). Two-dimensional dynamics of elasto-inertial turbulence and its role in polymer drag reduction. *Physical Review Fluids*, 3(1):011301.
- Sid, S., Terrapon, V. E., and Dubief, Y. (2018b). Two-dimensional dynamics of elasto-inertial turbulence and its role in polymer drag reduction. *Physical Review Fluids*, 3(1):011301.
- Singh, S., Subramanian, G., and Ansumali, S. (2011). A lattice boltzmann method for dilute polymer solutions. *Philosophical Transactions of the Royal Society A: Mathematical, Physical and Engineering Sciences*, 369(1944):2301–2310.
- Singh, S., Subramanian, G., and Ansumali, S. (2022). Two-fluid kinetic theory for dilute polymer solutions. *Physical Review E*, 106(4):044501.
- Soibelman, I. and Meiron, D. I. (1991). Finite-amplitude bifurcations in plane poiseuille flow: two-dimensional hopf bifurcation. *J. Fluid Mech.*, 229:389–416.
- Solon, A. P., Cates, M., and Tailleur, J. (2015). Active brownian particles and run-and-tumble particles: A comparative study. *The European Physical Journal Special Topics*, 224(7):1231–1262.

- Squires, T. M. and Quake, S. R. (2005). Microfluidics: Fluid physics at the nanoliter scale. *Reviews of modern physics*, 77(3):977.
- Srinivas, S. S. and Kumaran, V. (2017). Effect of viscoelasticity on the soft-wall transition and turbulence in a microchannel. *J. Fluid Mech.*, 812:1076–1118.
- Stenhammar, J., Nardini, C., Nash, R. W., Marenduzzo, D., and Morozov, A. (2017). Role of correlations in the collective behavior of microswimmer suspensions. *Physical review letters*, 119(2):028005.
- Stenhammar, J., Tiribocchi, A., Allen, R. J., Marenduzzo, D., and Cates, M. E. (2013). Continuum theory of phase separation kinetics for active brownian particles. *Physical review letters*, 111(14):145702.
- Stocker, R. (2011). Reverse and flick: Hybrid locomotion in bacteria. *Proceedings of the National Academy of Sciences*, 108(7):2635–2636.
- Stone, P., Roy, A., Larson, R. G., Waleffe, F., and Graham, M. D. (2004). Polymer drag reduction in exact coherent structures of plane shear flow. *Phys. Fluids*, 16:3470–3482.
- Stone, P. A., Waleffe, F., and Graham, M. D. (2002). Towards a structural understanding of turbulent drag reduction: nonlinear coherent states in viscoelastic shear flows. *Phys. Rev. Lett.*, 89:208301.
- Strogatz, S. H. and Mirollo, R. E. (1991). Stability of incoherence in a population of coupled oscillators. *Journal of Statistical Physics*, 63(3-4):613–635.
- Strogatz, S. H., Mirollo, R. E., and Matthews, P. C. (1992). Coupled nonlinear oscillators below the synchronization threshold: relaxation by generalized landau damping. *Physical review letters*, 68(18):2730.
- Subramanian, G. and Koch, D. (2009). Critical bacterial concentration for the onset of collective swimming. *J. Fluid Mech.*, 632:359–400.
- Subramanian, G., Koch, D. L., and Fitzgibbon, S. R. (2011). The stability of a homogeneous suspension of chemotactic bacteria. *Physics of Fluids*, 23(4).
- Subramanian, G. and Nott, P. (2011). The fluid dynamics of swimming microorganisms and cells. *IISc J.*, 91:283–313.
- Sureshkumar, R. and Beris, A. N. (1995a). Effect of artificial stress diffusivity on the stability of numerical calculations and the flow dynamics of time-dependent viscoelastic flows. *Journal of Non-Newtonian Fluid Mechanics*, 60(1):53–80.
- Sureshkumar, R. and Beris, A. N. (1995b). Linear stability analysis of viscoelastic poiseuille flow using an arnoldi based orthogonalization algorithm. *J. Non-Newtonian Fluid Mech.*, 56:151–182.
- Sureshkumar, R., Beris, A. N., and Handler, R. A. (1997). Direct numerical simulation of the turbulent channel flow of a polymer solution. *Physics of Fluids*, 9(3):743–755.
- Tailleur, J. and Cates, M. (2008). Statistical mechanics of interacting run-and-tumble bacteria. *Physical review letters*, 100(21):218103.

- Tailleur, J. and Cates, M. (2009). Sedimentation, trapping, and rectification of dilute bacteria. *EPL (Europhysics Letters)*, 86(6):60002.
- Taktikos, J., Stark, H., and Zaburdaev, V. (2013). How the motility pattern of bacteria affects their dispersal and chemotaxis. *PloS one*, 8(12):e81936.
- Tauber, U. C. (2014). *Critical dynamics: a field theory approach to equilibrium and non-equilibrium scaling behavior*. Cambridge University Press.
- Thampi, S. and Yeomans, J. (2016). Active turbulence in active nematics. *The European Physical Journal Special Topics*, 225:651–662.
- Thompson, A. G., Tailleur, J., Cates, M. E., and Blythe, R. A. (2011). Lattice models of nonequilibrium bacterial dynamics. *Journal of Statistical Mechanics: Theory and Experiment*, 2011(02):P02029.
- Tiribocchi, A., Wittkowski, R., Marenduzzo, D., and Cates, M. E. (2015). Active model h: scalar active matter in a momentum-conserving fluid. *Physical review letters*, 115(18):188302.
- Tjhung, E., Nardini, C., and Cates, M. E. (2018). Cluster phases and bubbly phase separation in active fluids: reversal of the ostwald process. *Physical Review X*, 8(3):031080.
- Toms, B. A. (1977). On the early experiments on drag reduction by polymers. *Phys. Fluids*, 20:S3.
- Ueyama, H. (1980). The stochastic boltzmann equation and hydrodynamic fluctuations. *Journal of Statistical Physics*, 22(1):1–26.
- Underhill, P. T. and Graham, M. D. (2011). Correlations and fluctuations of stress and velocity in suspensions of swimming microorganisms. *Physics of Fluids*, 23(12).
- Valeriani, C., Li, M., Novosel, J., Arlt, J., and Marenduzzo, D. (2011). Colloids in a bacterial bath: simulations and experiments. *Soft Matter*, 7(11):5228–5238.
- Van Kampen, N. G. (1955). On the theory of stationary waves in plasmas. *Physica*, 21(6-10):949–963.
- Van Kampen, N. G. (1992). *Stochastic processes in physics and chemistry*, volume 1. Elsevier.
- Vennamneni, L., Nambiar, S., and Subramanian, G. (2020). Shear-induced migration of microswimmers in pressure-driven channel flow. *Journal of Fluid Mechanics*, 890.
- Vicsek, T. and Zafeiris, A. (2012). Collective motion. *Physics reports*, 517(3-4):71–140.
- Virk, P. (1975). Drag reduction fundamentals. *AIChE J.*, 21:625–656.
- Waleffe, F. (1998). Three-dimensional coherent states in plane shear flows. *Phys. Rev. Lett.*, 81:4140–4143.
- Wan, K. Y. and Goldstein, R. E. (2018). Time irreversibility and criticality in the motility of a flagellate microorganism. *Physical review letters*, 121(5):058103.

- Wang, Z., Chen, H.-Y., Sheng, Y.-J., and Tsao, H.-K. (2014). Diffusion, sedimentation equilibrium, and harmonic trapping of run-and-tumble nanoswimmers. *Soft Matter*, 10(18):3209–3217.
- Wensink, H. H., Dunkel, J., Heidenreich, S., Drescher, K., Goldstein, R. E., Löwen, H., and Yeomans, J. M. (2012). Meso-scale turbulence in living fluids. *Proceedings of the National Academy of Sciences*, 109(36):14308–14313.
- White, C. and Mungal, M. (2008). Mechanics and prediction of turbulent drag reduction with polymer additives. *Annu. Rev. Fluid Mech.*, 40:235–256.
- Wilson, H. J., Renardy, M., and Renardy, Y. (1999). Structure of the spectrum in zero reynolds number shear flow of the ucm and oldroyd-b liquids. *J. Non-Newton. Fluid Mech.*, 80(2):251–268.
- Wilson, L. G., Martinez, V. A., Schwarz-Linek, J., Tailleur, J., Bryant, G., Pusey, P., and Poon, W. C. (2011). Differential dynamic microscopy of bacterial motility. *Physical review letters*, 106(1):018101.
- Wittkowski, R., Tiribocchi, A., Stenhammar, J., Allen, R. J., Marenduzzo, D., and Cates, M. E. (2014). Scalar ϕ^4 field theory for active-particle phase separation. *Nature communications*, 5(1):4351.
- Woillez, E., Zhao, Y., Kafri, Y., Lecomte, V., and Tailleur, J. (2019). Activated escape of a self-propelled particle from a metastable state. *Phys. Rev. Lett.*, 122:258001.
- Wu, X.-L. and Libchaber, A. (2000). Particle diffusion in a quasi-two-dimensional bacterial bath. *Physical review letters*, 84(13):3017.
- Wynanski, I. and Champagne, F. (1973). On transition in a pipe. part 1. the origin of puffs and slugs and the flow in a turbulent slug. *J. Fluid Mech.*, 59(2):281–335.
- Wynanski, I., Sokolov, M., and Friedman, D. (1975). On transition in a pipe. part 2. the equilibrium puff. *J. Fluid Mech.*, 69(2):283–304.
- Xi, L. and Graham, M. D. (2012). Dynamics on the laminar-turbulent boundary and the origin of the maximum drag reduction asymptote. *Phys. Rev. Lett.*, 108(2):028301.
- Yan, W. and Brady, J. F. (2015). The force on a boundary in active matter. *Journal of Fluid Mechanics*, 785.
- Zakin, J., Ni, C., Hansen, R., and Reischman, M. (1977). Laser doppler velocimetry studies of early turbulence. *Phys. Fluids*, 10:S85–S88.
- Zakin, J. L., Lu, B., and Bewersdorff, H. W. (1998). Surfactant drag reduction. *Reviews in Chemical Engineering*, 14(4-5):253–320.
- Zell, A., Gier, S., Rafai, S., and Wagner, C. (2010). Is there a relation between the relaxation time measured in caber experiments and the first normal stress coefficient?. *J. Non-Newton. Fluid Mech.*, 165(19):1265–1274.
- Zhang, M., Lashgari, I., Zaki, T. A., and Brandt, L. (2013). Linear stability analysis of channel flow of viscoelastic Oldroyd-B and FENE-P fluids. *J. Fluid Mech.*, 737:249–279.

Zöttl, A. and Stark, H. (2016). Emergent behavior in active colloids. *Journal of Physics: Condensed Matter*, 28(25):253001.

Zwanzig, R. (2001). *Nonequilibrium statistical mechanics*. Oxford University Press.